JAIST Repository
https://dspace.jaist.ac.jp/

Title	グラフェンナノ構造における単キャリア輸送現象と局所ドーピング効果
Author(s)	岩﨑，拓哉
Citation	
Issue Date	2017-03
Type	Thesis or Dissertation
Text version	ETD
URL	http://hdl.handle.net/10119/14252
Rights	
Description	Supervisor:水田　博，マテリアルサイエンス研究科，博士

JAIST
JAPAN
ADVANCED INSTITUTE OF
SCIENCE AND TECHNOLOGY

Japan Advanced Institute of Science and Technology

Doctoral Dissertation

Single carrier transport and local doping effects on graphene nanostructures

Takuya Iwasaki

Supervisor : Prof. Hiroshi Mizuta

School of Materials Science
Japan Advanced Institute of Science and Technology

March 2017

Abstract

Since electrons in graphene-based quantum dots (QDs) are promising for quantum information processing (*i.e.*, quantum bit), graphene nanodevices have therefore been studied to realize single electron/hole transport property. However, the clear characteristic of single QD (SQD) has not been established yet in graphene devices because of the formation of unintentional multiple dots in graphene caused by uncontrollable potential inhomogeneity and edge irregularity. In particular, single carrier transport at the intrinsic Dirac point (at zero gate voltage) has not been observed so far. This study aims to fabricate and measure the graphene SQD based on the following two approaches: (1) optimizing the design of the device structure, and (2) reducing the influence of charged impurity (*e.g.*, carrier localization, namely the local doping effect).

As a result of (1), it is revealed that the devices with the geometrically-defined quantum dot shows multiple dots characteristics rather than that of the single dot. This indicates that unintentional dots are formed in the graphene channel comprising constrictions and a dot structure. Moreover, simple nanoribbon devices with a longer length ($\geq$100nm) and a narrower width also exhibited the multiple dots behavior. Even though the ultra-narrow nanoribbon (width $\sim$5 nm) fabricated by the novel patterning process using hydrogen silsesquioxane, the SQD behavior was not observed in the nanoribbon with a longer length. From these results, it is understood that the formation of unintentional dots can not be avoided even in a narrow constriction if it has a longer length. In order to overcome this issue, the constriction with a short length and a narrow width can be considered as a more suitable structure to form the SQD in graphene.

For (2), firstly, the distribution of doping concentration in graphene is spatially resolved by using tip-enhanced Raman spectroscopy. It is clarified that the hole doping concentration is modulated by the order of magnitude of 10^{13} cm^{-2} within a distance of 1 μm by the variation in the device fabrication process. Secondary, the mechanism of irreversible change in carrier transport property of graphene devices by the post annealing process is elucidated by the systematic experiments and the first principle calculations. As a result, it is found that the shift of the charge neutrality point (*i.e.*, averaged doping effects in overall graphene) can be controlled by annealing in the vacuum or hydrogen gas environment.

Based on the above results, graphene constriction devices with a short length and a narrow width are studied to realize the SQD behavior in graphene. The regular Coulomb diamond and periodic Coulomb oscillation characteristics are observed at the temperature of 5 K in the certain gate voltage range, which indicates the transport property through the SQD. Comparing the extracted parameters from the transport measurements and from the geometric structure in the scanning electron microscope images, it can be considered that the single dot is formed in the constriction region. By shifting CNP near

to zero voltage by annealing, transport through randomly formed multiple dots is not yet eliminated. Though the potential inhomogeneity presents in the SQD formed in the constriction region, the possibility of single dot formation is increased due to the overall reduction in the edge irregularities.

Keywords: Graphene nanostructure, Single carrier transport, Doping effect, Coulomb blockade, Quantum dot, Single electron transistor

Contents

This dissertation was prepared according to the curriculum for the Collaborative Education Program organized by Japan Advanced Institute of Science and Technology and University of Southampton.

Acronyms

AFM	**A**tomic **F**orce **M**icroscopy/**M**icroscope
BLG	**Bi****L**ayer **G**raphene
CNP	**C**harge **N**eutrality **P**oint
CVD	**C**hemical **V**apor **D**eposition
DFT	**D**ensity **F**unctional **T**heory
DIW	**D**e**I**onized **W**ater
DOS	**D**ensity **O**f **S**tate
DQD	**D**ouble **Q**uantum **D**ot
EB	**E**lectron **B**eam
EBL	**E**lectron **B**eam **L**ithography
FET	**F**ield-**E**ffect **T**ransistor
FWHM	**F**ull **W**idth at **H**alf **M**aximum
GNR	**G**raphene **N**ano**R**ibbon
h-BN	**h**exagonal **B**oron **N**itride
HOPG	**H**ighly **O**riented **P**yrolytic **G**raphite
HSQ	**H**ydrogen **S**ilses**Q**uioxane
ICP-RIE	**I**nductive **C**oupled **P**lasma-**R**eactive **I**on **E**tching
IPA	**I**so**P**ropyl **A**lcohol
MIBK	**M**ethyl **I**so**B**utyl **K**etone
MMA	**M**ethyl **M**eth**A**crylate
NA	**N**umerical **A**perture
NMP	**N**-**M**ethyl-2-**P**yrrolidone
PMMA	**P**oly(**M**ethyl **M**eth**A**crylate)
PSB	**P**auli **S**pin **B**lockade
QD	**Q**uantum **D**ot
RIE	**R**eactive **I**on **E**tching
SCT	**S**ingle **C**arrier **T**ransistor
SEM	**S**canning **E**lectron **M**icroscopy/**M**icroscope
SET	**S**ingle **E**lectron **T**ransistor
SLG	**S**ingle **L**ayer **G**raphene
SQD	**S**ingle **Q**uantum **D**ot
TERS	**T**ip-**E**nhanced **R**aman **S**pectroscopy

Symbols

C_Σ	Total capacitance
C_g	Gate capacitance
e	Elementary charge
E_C	Charging energy
G	Conductance
G_diff	Differential conductance
h	Planck constant
$\hbar$	Dirac constant $= h/2\pi$
k_B	Boltzmann constant
L	Channel length
n	Carrier density
T	Temperature
v_F	Fermi velocity
V_d	Source-drain bias voltage
V_g	Gate voltage
V_CNP	Voltage at charge neutrality point
W	Channel width
ϵ_0	Vacuum permittivity
$\epsilon_{\mathrm{SiO_2}}$	Dielectric constant of SiO_2
μ_FE	Field effect mobility
σ	Conductivity
σ_min	Minimum conductivity
ρ	Resistivity

Chapter 1

Introduction

1.1 Overview of graphene quantum devices

Graphene, a one-atom-thick two-dimensional material composed of sp^2 bonded carbon atoms arranged in a honeycomb lattice structure, has attracted great interest in recent years. In 2004, the research team at the University of Manchester succeeded in separating graphene from graphite by a mechanical exfoliation method using an adhesive tape.[1] Since they also demonstrated that graphene has a remarkable electric field effect, many researchers were fascinated due to the simple acquisition method of graphene and the possibility of many kinds of device applications. Hence, the researches of graphene ignited all over the world. In 2010, as the achievements that the discovery and characterization of graphene were highly acclaimed, Novoselov and Geim in the University of Manchester were awarded the Nobel Prize in Physics. The number of research articles on graphene is still increasing annually in extensive research fields, such as physics, chemistry, biology, medical science, engineering, etc.[2–5]

The major feature of graphene is the special structure of energy band stemming from the nature of the two-dimensional system.[6,7] In the low energy region, the valence band and the conduction band are in a cone shape and are contacted to each other at zero energy (the structure is called the Dirac cone, and the contacted point is called the Dirac point). This indicates that the dispersion relation of graphene is linear at low energy, and that there is no band gap unlike semiconductor materials. Since the linear energy dispersion, effective mass approximation can not be applied, and the electrons in graphene are regarded as relativistic particles, *i.e.*, massless Dirac fermions. The Fermi velocity in graphene is extremely fast $\sim 10^6$ m/s, 1/300 of the speed of light. In addition, the conductive carrier

type in graphene can be switched between electrons and holes by simply gating across the Dirac point, called ambipolar characteristic. These electronic properties of graphene result in causing Klein tunneling phenomenon that allows electrons to have perfectly transparency for potential barriers without energy dissipation (elastic tunneling).[6–8]

Unlike two-dimensional electron gas (2DEG) in heterostructured compound semiconductors, graphene is a completely two-dimensional system, and thereby various quantum phenomena are expected to be observed at high temperatures. In 2005, it has reported that graphene exhibited the anomalous quantum Hall effect even at room temperature.[9]

Graphene quantum devices would make a great contribution to the research field of quantum phenomenon in condensed matters and quantum information processing. In particular, the spin coherence of electrons in graphene is predicted to be preserved for long time due to that a relatively light carbon atom leads to small spin-orbit interaction, and that nuclear magnetic moment (hyperfine interaction) in graphene composed of ^{12}C isotope is almost negligible.[10] Hence, the spin of electrons in graphene is expected as a key factor for the implementation of spin quantum bits in solid states. The essential to realize graphene-based quantum devices is the three-dimensionally confinement of an electron in potential barriers. In case of graphene, because graphene has no band gap and there is Klein tunneling, electron confinement by potential control using top gate, which used for the 2DEG systems, is difficult.

So far, a geometrically-defined quantum dot (QD) structure has been widely used like silicon-based QD devices in order to confine an electron. In 2008, the graphene QD device using lateral side gates was firstly reported,[11] and Coulomb blockade, the fundamental characteristic of single electron transport was observed at 1.7 K. Several research teams have then succeeded in fabricating and characterizing the graphene QD devices and observing typical quantum transport properties. For example, the graphene nanoribbon (GNR)[12] or the single electron transistor (SET),[13] whose diameter is sufficient large $\sim$100 nm to neglect quantum confinement energy,[14] in the vicinity of the QD was used as a charge detector, allowing to detect the signal of excited state. In the controllable graphene SQD with the lateral side-gate, electron-hole crossover in which the transported carrier is switched to other type polarity was observed by the transport measurements applying a perpendicular magnetic field at 90 mK.[15] Furthermore, the determination of the spin state was demonstrated in the same device.[16]

Graphene double quantum dot (DQD) devices were also studied in both geometrical definition[17–19] and gating for GNR,[20] the stability diagram where the resonant current peaks present a honeycomb structure was observed indicating that the device acts as the DQD system. Even though the some properties, such as the excited state and the interdot capacitive/tunnel coupling, were characterized in graphene DQD devices,[18,19] some phenomena expected in the DQD system have not been observed so far. For instance, the spin-dependent current rectification, called Pauli spin blockade (PSB), allow to control the spin state in QDs, and thereby the observation of this phenomena is one of the milestone for spin qubit implementation.[21] The failure to observe PSB is attributed to the localized carriers in the constriction region acting as pseudo QDs,[22] because the observation of PSB requires the system with certain double weakly coupled quantum QDs.[23] The carrier localization is caused by potential inhomogeneities in graphene, due to, for example, edge disorder, roughness of a substrate, and charged impurity on the surface of graphene and the interface between graphene and substrate.[24]

For bilayer graphene (BLG), geometrically-defined SQD[25,26] and DQD[27,28] devices have been studied as well, which also have not shown the PSB phenomena yet owing to the same reason in the case of using SLG. In the case of BLG, since its electronic band structure largely differs from that of SLG, an electron in BLG has an effective mass of $0.03m_e$ (m_e is the mass of free electron) at low energy, and the band gap can be opened by applying a perpendicular electric field.[6,7] Hence, the QD can be defined by gating in a large BLG flake, which allows to avoid the influence of edge disorder. This method has been applied to form the SQD structure in BLG,[29,30] and however, not been applied for the DQD structure until now. As the technology of hexagonal boron nitride (h-BN) dielectric material has been recently developed leading to the better quality of graphene, the gate-defined BLG DQD device can be expected for observing the PSB phenomenon in BLG.[29,31] For trilayer graphene, SQD and DQD have been studied only little.[32–34] As similar to the SLG DQD devices,[19] the trilayer graphene DQD showed the non-monotonically variable interdot tunnel coupling, which is ascribed to edge disorder.

1.2 Motivations and aim

In almost cases, well-controlled QD transport characteristics have been achieved by the side and top gate control. However, all of them have the problems that the influence of potential inhomogeneities due to edge disorder, and charge impurities strongly appeared disturbing the observation of some physical phenomena. In 2013, it has been reported that the transport properties of the geometrically-defined BLG SQD device fabricated with the very sophisticated constrictions (the length and width are ∼10 nm), which did not show the SQD behavior.[22] The observed transport behavior was explained by the model of serial triple QDs instead of SQD. As mentioned above, the QDs are unintentionally formed in the constriction regions which are ideally expected to act as only the tunnel barriers. This behavior has been observed in the GNR devices with the length of ≥100 nm, where multiple serial QDs were formed due to the edge disorder and the charge localization. In particular, the localized charge means local doping on graphene, whose spatial scale is ∼30 nm,[35] behaving as the QDs. From these reports, it can be suspected that the QD formation needs the certain area to manifest itself.

For high resolution patterning in top-down fabrication of graphene, there are attempts to ultra-fine microfabrication, such as direct milling using a helium ion beam.[36] However, the control of the perfectly aligned edge structure has not been achieved at present. On the other hand, it is known that charged impurities basically originate from remaining of resists or chemicals used in device fabrication processes, and from the physical adsorption of gas molecules at the surface of graphene.[37,38] In 2007, it was reported that contaminations at the surface of graphene was observed and can be removed by the annealing treatment.[39] Additionally, it also was reported that the doping effect which stem from physically adsorbed gas molecules at the surface of graphene can be reduced by the annealing treatment.[38] The annealing treatment is, therefore, conceivable as means for suppressing the doping effect that is the influence of charge impurities caused by physically adsorbed molecules from graphene surface or substrate. Currently, the annealing treatment has been widely used in various graphene researches, but its mechanism has not been investigated in detail.

As aimed to form the graphene SQD, this study approached from two points of view as follows: (1) optimizing the device structure where the

SQD is naturally formed without the lateral control from the side-gates, (2) investigating the doping effect that caused by the charged impurities for the transport properties in graphene, and the developing the method to reduce the doping effects.

Firstly, graphene devices with the geometrically-defined SQD were studied varying the dimension of QD and constrictions to explore the optimum structure for the SQD formation. From this experiment, it is found that the formation of unintentional QDs in constrictions can not be avoid in the intentionally-patterned QD structures without control by the side gates. Next, the GNR devices with the long length and the extremely narrow width were fabricated and characterized. As results, the multiple QDs behavior was observed even width was narrowed to $\sim$5 nm. According to the literatures and these results, the nano-constriction, *i.e.*, the GNR with short length and narrow width, seems to be the proper structure for the SQD formation in graphene. In order to examine how the doping due to the charge impurities is localized on graphene, tip-enhanced Raman spectroscopy (TERS) technology was utilize to ascertain the spatial scale of doping concentration induced by the device fabrication process. Then, the doping effects for the transport properties in grpahene affects were studied in graphene field-effect transistors (FETs), and moreover, the effects and mechanisms of annealing treatment for them were clarified by the systematic annealing experiments. Consequently, the annealing treatment in vacuum condition can control the doping property by changing the annealing duration time. Finally, using the finding in the former experiments and analysis, the SQD behavior was observed in the SLG-based nano-constriction device without control from the side gates at 5 K. In this measurement, it is revealed that the SQD is formed in the nano-constriction region, and extracted the energy scale and the effective dimension of SQD. Since this nano-constriction structure is a fundamental building block for QD devices, its investigation and understanding in detail were imperative, clarified in this thesis. Hence, this work would make great contributions for the research field in quantum transport in graphene (academic) and graphene-based device applications (industrial).

1.3 Structure of this thesis

In Chapter 1, the overall concept and motivation, purpose, main results of this thesis are described. Chapter 2 describes the theoretical back-

ground of research and the recent reports on the related research with examples are reviewed. In Chapter 3, the device fabrication process and the measurement method of transport characteristics are explained, those are common through this thesis. For investigating the suitable device design and dimension, the geometrically defined graphene QDs and GNRs with the high aspect ratio are studied and shown in Chapter 4. The simple method to fabricate the ultra narrow GNR structure developed during this experiment is proposed. Chapter 5 discusses the local doping effects on graphene. In order to probe local doping, the tip-enhanced Raman spectroscopy technique is used for the spectra scanning with high spatial resolution over than laser diffraction limit. Furthermore the mechanism of the change in tranport properties before and after annealing is analyzed to utilize the annealing method for controlling the doping state of graphene. Chapter 6 shows the study on the transport properties of graphene nanoconstrictions based on the consideration of the design optimization, doping, and annealing effect discussed in the previous chapters for the final aim of the this thesis, that is, the SQD formation. Finally, all works in this thesis are summarized and concluded in Chapter 7, and the prospects for future development of this theme are presented.

References

1) K. S. Novoselov, A. K. Geim, S. V. Morozov, D. Jiang, Y. Zhang, S. V. Dubonos, I. V. Grigorieva, A. A. Firsov, Electric field effect in atomically thin carbon films. *Science* **306**, 666 (2004).

2) A. K. Geim, K. S. Novoselov, The rise of graphene. *Nat. Mater.* **6**, 183 (2007).

3) A. K. Geim, Graphene: Status and prospects. *Science* **324**, 1530 (2009).

4) K. S. Novoselov, V. I. Fal′ko, L. Colombo, P. R. Gellert, M. G. Schwab, K. Kim, A roadmap for graphene. *Nature* **490**, 192 (2012).

5) A. C. Ferrari, *et al.*, Science and technology roadmap for graphene, related two-dimensional crystals, and hybrid systems. *Nanoscale* **7**, 4587 (2015).

6) A. H. Castro Neto, F. Guinea, N. M. R. Peres, K. S. Novoselov, A. K. Geim, The electronic properties of graphene. *Rev. Mod. Phys.* **81**, 109 (2009).

7) S. Das Sarma, S. Adam, E. H. Hwang, E. Rossi, Electronic transport in two-dimensional graphene. *Rev. Mod. Phys.* **83**, 407 (2011).

8) A. F. Young, P. Kim, Quantum interference and Klein tunnelling in graphene heterojunctions. *Nat. Phys.* **5**, 222 (2009).

9) K. S. Novoselov, A. K. Geim, S. V. Morozov, D. Jiang, M. I. Katsnelson, I. V. Grigorieva, S. V. Dubonos, A. A. Firsov, Two-dimensional gas of massless Dirac fermions in graphene. *Nature* **438**, 197 (2005).

10) B. Trauzettel, D. V. Bulaev, D. Loss, G. Burkard, Spin qubits in graphene quantum dots, *Nat. Phys.* **3**, 192 (2007).

11) C. Stampfer, J. Güttinger, F. Molitor, D. Graf, T. Ihn, K. Ensslin, Tunable Coulomb blockade in nanostructured graphene. *Appl. Phys. Lett.* **92**, 012102 (2008).

12) J. Güttinger, C. Stampfer, S. Hellm*ddoto*, F. Molitor, T. Ihn, K. Ensslin, Charge detection in graphene quantum dots. Appl. Phts. Lett. **93**, 212102 (2008).

13) L. J. Wang, G. Cao, T. Tu, H. O. Li, C. Zhou, X. J. Hao, Z. Su, G. C. Guo, H. W. Jiang, G. P. Guo, A graphene quantum dot with a single electron transistor as an integrated charge sensor. *Appl. Phys. Lett.* **97**, 262113 (2010).

14) L. A. Ponomarenko, F. Schedin, M. I. Katsnelson, R. Yang, E. W. Hill, K. S. Novoselov, A. K. Geim, Chaotic Dirac billiard in graphene quantum dots. *Science* **320**, 356 (2008).

15) J. Güttinger, C. Stampfer, F. Libisch, T. Frey, J. Burgdörfer, T. Ihn, K. Ensslin, Electron-hole crossover in graphene quantum dots. *Phys. Rev. Lett.* **103**, 046810 (2009).

16) J. Güttinger, T. Frey, C. Stampfer, T. Ihn, K. Ensslin, Spin states in graphene quantum dots. *Phys. Rev. Lett.* **105**, 116801 (2010).

17) F. Molitor, S. Dröscher, J. Güttinger, A. Jacobsen, C. Stampfer, T. Ihn, K. Ensslin, Transport through graphene double dots. *Appl. Phys. Lett.* **94**, 222107 (2009).

18) F. Molitor, H. Knowles, S. Dröscher, U.Gasser, T. Choi, P. Roulleau, J. Güttinger, A. Jacobsen, C. Stampfer, K. Ensslin, T. Ihn, Observation of excited states in a graphene double quantum dot. *Europhys. Lett.* **89**, 67005 (2010).

19) D. Wei, H. O. Li, G. Cao, G. Luo, Z. X. Zheng, T. Tu, M. Xiao, G. C. Guo, H. W. Jiang, G. P. Guo, Tuning inter-dot tunnel coupling of an etched graphene double quantum dot by adjacent metal gates. *Sci. Rep.* **3**, 3175 (2013).

20) X. L. Liu, D. Hug, L. M. K. Vandersypen, Gate-defined graphene double quantum dot and excited state spectroscopy. *Nano Lett.* **10**, 1623 (2010).

21) K. Ono, D. G. Austing, Y. Tokura, S. Tarucha, Current rectification by Pauli exclusion in a weakly coupled double quantum dot system. *Science* **297**, 1313 (2002).

22) D. Bischoff, A. Varlet, P. Simonet, T. Ihn, K. Ensslin, Electronic triple-dot transport through a bilayer graphene island with ultrasmall constrictions. *New J. Phys.* **15**, 083029 (2013).

23) A. C. Johnson, J. R. Petta, C. M. Marcus, M. P. Hanson, A. C. Gossard Singlet-triplet spin blockade and charge sensing in a few-electron double quantum dot. *Phys. Rev. B* **72**, 165308 (2005).

24) D. Bischoff, A. Varlet, P. Simonet, M. Eich, H. C. Overweg, T. Ihn, K. Ensslin,Localized charge carriers in graphene nanodevices. *Appl. Phys. Rev.* **2**, 031301 (2015).

25) S. Dröscher, J. Güttinger, T. Mathis, B. Batlogg, T. Ihn, K. Ensslin, High-frequency gate manipulation of a bilayer graphene quantum dot. *Appl. Phys. Lett.* **101**, 043107 (2012).

26) S. Fringes, C. Volk, C. Norda, B. Terrés, J. Dauber, S. Engels, S. Trellenkamp, C. Stampfer, Charge detection in a bilayer graphene quantum dot. *Phys. Status Solidi B* **248**, 2684 (2011).

27) C.Volk, S. Fringes, B. Terrrés, J. Dauber, S. Engels, S. Trellenkamp, C. Stampfer, Electronic excited states in bilayer graphene double quantum dots. *Nano Lett.* **11**, 3581 (2011).

28) L. J. Wang, H. O. Li, T. Tu, G. Cao, C. Zhou, X. J. Hao, Z. Su, M. Xiao, G. C. Guo, A. M. Chang, G. P. Guo, Controllable tunnel coupling and molecular states in a graphene double quantum dot. *Appl. Phys. Lett.* **100**, 022106 (2012).

29) A. M. Goossens, S. C. M. Driessen, T. A. Baart, K. Watanabe, T. Taniguchi, L. M. K. Vandersypen, Gate-defined confinement in bilayer graphene-hexagonal boron nitride hybrid devices. *Nano Lett.* **12**, 4656 (2012).

30) M. T. Allen, J. Martin, A. Yacoby, Gate-defined quantum confinement in suspended bilayer graphene. *Nat. Commun.* **3**, 934 (2012).

31) C. R. Dean, A. F. Young, I. Meric, C. Lee, L. Wang, S. Sorgenfrei, K. Watanabe, T. Taniguchi, P. Kim, K. L. Shepard, J. Hone, Boron

nitride substrates for high-quality graphene electronics. *Nat. Nanotech.* **5**, 722 (2010).

32) J. Güttinger, C. Stampfer, D. Graf, T. Ihn, K. Ensslin, Coulomb oscillations in three-layer graphene nanostructures. *New J. Phys.* **10**, 125029 (2008).

33) S. Moriyama, D. Tsuya, E. Watanabe, S. Uji, M. Shimizu, T. Mori, T. Yamaguchi, K. Ishibashi, Coupled quantum dots in a graphene-based two-dimensional semimetal. *Nano Lett.* **9**, 2891 (2009).

34) S. Moriyama, Y. Morita, E. Watanabe, D. Tsuya, S. Uji, M. Shimizu, K. Ishibashi, Fabrication of quantum-dot devices in graphene. *Sci. Technol. Adv. Mater.* **11**, 054601 (2010).

35) J. Martin, N. Akerman, G. Ulbricht, T. Lohmann, J. H. Smet, K. Von Klitzing, A. Yacoby, Observation of electronhole puddles in graphene using a scanning single-electron transistor. *Nat. Phys.* **4**, 144 (2008).

36) M. C. Lemme, D. C. Bell, J. R. Williams, L. A. Stern, B. W. H. Baugher, P. Jarillo-Herrero, C. M. Marcus, Etching of graphene devices with a helium ion beam. *ACS Nano* **3**, 2674 (2009).

37) A. Pirkle, J. Chan, A. Venugopal, D. Hinojos, C. W. Magnuson, S. McDonnell, L. Colombo, E. M. Vogel, R. S. Ruoff, R. M. Wallace, The effect of chemical residues on the physical and electrical properties of chemical vapor deposited graphene transferred to SiO_2. *Appl. Phys. Lett.* **99**, 122108 (2011).

38) F. Schedin, A. K. Geim, S. V. Morozov, E. W. Hill, P. Blake, M. I. Katsnelson, K. S. Novoselov, Detection of individual gas molecules adsorbed on graphene. *Nat. Mater.* **6**, 652 (2007).

39) M. Ishigami, J. H. Chen, W. G. Cullen, M. S. Fuhrer, E. D. Williams, Atomic structure of graphene on SiO_2. *Nano Lett.* **7**, 1643 (2007).

Chapter 2

Research background

In this chapter, the theoretical background behind the related research field is presented. In particular, the researches on graphene involved with annealing, carrier localization, doping effects, and Coulomb blockade on GNR and QD devices are reviewed.

2.1 Theoretical background

2.1.1 Electronic structure of graphene

In this section, the basic of the electronic band structure of graphene is briefly described. Graphene comprises of sp^2 bonded carbon atoms with a honeycomb lattice structure. Among four valence electrons for carbon, three electrons constitute the sp^2 orbital hybridization, and make the σ-bonds with three neighbor carbon atoms, while one electron in the $2p_z$ orbital (π electron) freely moves in graphene, that is responsible for the electronic state near the Fermi energy of graphene.

Figure 2.1 shows the lattice structure and the unit cell of graphene. As a honeycomb structure is a typical non-Bravais lattice, two geometrically-asymmetric atoms (*i.e.*, two atoms are not translational symmetry) exist in the unit cell. In fact, the special electronic structure of graphene originates from this sub-lattice structure. Here each atom is named as A and B as shown in Fig. Figure exhibits the first Brillouin zone of graphene, forming a hexagon shape. The center of hexagon, each apex of hexagon, and the middle point of sides are called the Γ point, the K and K' points, and the M point, respectively.

The tight-binding approximation is conventionally used for the calculation of the electronic state of graphene,[1] which is the concept considering that the electron transfer happens between only neighbor atoms. Regard-

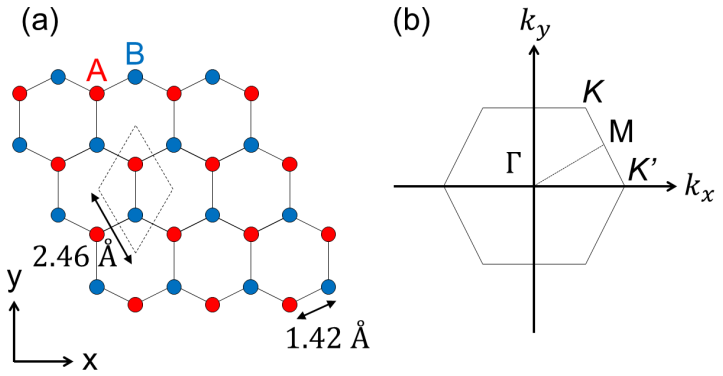

Figure 2.1: (a) Graphene lattice in the real space. Dashed line is the boundary of the unit cell. (b) First Brillouin zone of graphene. The center of hexagon (Γ), each apex of hexagon (K or K'), and the middle point of sides (M) are marked.

ing the wave function for A and B as ψ_A and ψ_B, the Hamiltonian $\mathcal{H}$ for describing the electronic state of graphene is followings:

$$\mathcal{H} = \begin{pmatrix} \langle\psi_A|\mathcal{H}|\psi_A\rangle & \langle\psi_A|\mathcal{H}|\psi_B\rangle \\ \langle\psi_B|\mathcal{H}|\psi_A\rangle & \langle\psi_B|\mathcal{H}|\psi_B\rangle \end{pmatrix}.$$

As the energies of π electrons for A and B are same, diagonal components are responsible for electron transfer from A (B) to B (A) meaning just the change in the overall energy of graphene, can be considered as 0 for simplifying the calculation. Taking the weight necessary for jumping to the orbit of the adjacent atom (hopping energy) written as γ_0 and Bloch's phase into account, non-diagonal components those are responsible for electron transfer from A (B) to B (A) are described as follows:

$$\langle\psi_A|\mathcal{H}|\psi_B\rangle = -\gamma_0 \sum_{n=1}^{3} \exp(i\vec{k}\cdot\vec{r_n})$$
$$\langle\psi_B|\mathcal{H}|\psi_A\rangle =^* \langle\psi_A|\mathcal{H}|\psi_B\rangle$$

where, $\vec{k} = (k_x, k_y)$ is the wave vector, and $\vec{r_n}$ is the vector for the transfer from A (B) to B (A). In the case that the $\vec{r_n}$ from A (B) to B (A) are considered as shown in Fig, $\vec{r_n}$ from A to B can be written as follows:

$$\vec{r_1} = (0, \frac{a}{\sqrt{3}}) \quad \vec{r_2} = (-\frac{a}{2}, -\frac{a}{2\sqrt{3}}) \quad \vec{r_3} = (\frac{a}{2}, -\frac{a}{2\sqrt{3}})$$

where, $a = 0.246$ nm is the lattice constant.

As the phase component written by $f(\vec{k})$, the Schrödinger equation of graphene is followings:

$$\begin{pmatrix} 0 & -\gamma_0 f(\vec{k}) \\ -\gamma_0 f^*(\vec{k}) & 0 \end{pmatrix} \begin{pmatrix} |\Psi_A\rangle(\vec{k}) \\ |\Psi_B\rangle(\vec{k}) \end{pmatrix} = E \begin{pmatrix} |\Psi_A\rangle(\vec{k}) \\ |\Psi_B\rangle(\vec{k}) \end{pmatrix}.$$

Assuming that the both wave function do not become 0 simultaneously, the energy eigenvalue can be derived by the determinant

$$det \begin{pmatrix} E & \gamma_0 f(\vec{k}) \\ \gamma_0 f^*(\vec{k}) & E \end{pmatrix} = 0.$$

This can be changed to

$$E(\vec{k}) = \pm\gamma_0 |f(\vec{k})|. \tag{2.1}$$

where $|f(\vec{k})|$ is

$$\begin{aligned} |f(\vec{k})| &= \sqrt{f(\vec{k}) f^*(\vec{k})} \\ &= \sqrt{\{\exp(i\frac{k_y a}{\sqrt{3}}) + 2\exp(-i\frac{k_y a}{2\sqrt{3}})\cos(\frac{k_x a}{2})\} f^*(\vec{k})} \\ &= \sqrt{1 + 4\cos^2(\frac{k_x a}{2}) + 4\cos(\frac{k_x a}{2})\cos(\frac{\sqrt{3}k_y a}{2})}. \end{aligned} \tag{2.2}$$

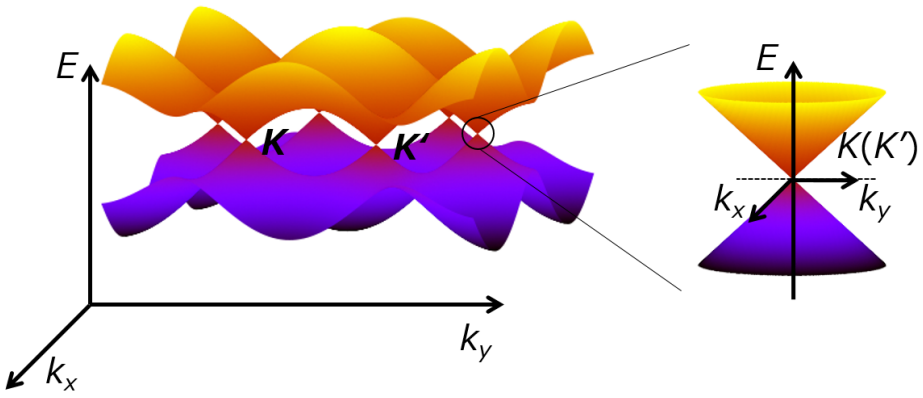

Figure 2.2: Energy band structure of graphene: Dirac cone.

The energy dispersion described by Eq. (2.2) is shown in Fig. 2.2. Assuming that there is one π electron on each carbon atom in average, in

the ground state the lower (π) band is completely filled with electrons and the upper (π^*) band is empty, *i.e.*, Fermi energy is $E = 0$, the lower band and the upper band are a valence band and a conduction band, respectively.

The dispersion relation near the K and K' points in the Brillouin zone are written as $\vec{K} = (2\pi/3a, 2\pi/\sqrt{3}a)$ and $\vec{K'} = (4\pi/3a, 0)$, then these can be expanded into the 1-order Taylor series near the K and K' points as follows:

$$\begin{aligned} f(\vec{k} + \vec{K'}) \cong & f(\vec{K'}) + \left[\frac{\partial}{\partial k_x} f(\vec{k})\right]_{\vec{k}=\vec{K'}} k_x + \left[\frac{\partial}{\partial k_y} f(\vec{k})\right]_{\vec{k}=\vec{K'}} k_y \\ = & 0 - \frac{\sqrt{3}a}{2} k_x + i\frac{\sqrt{3}a}{2} k_y \\ = & \frac{\sqrt{3}a}{2}(-k_x + ik_y). \end{aligned} \tag{2.3}$$

Therefore, the valence band and the conduction band are linear and touched at the the K and K' points, indicating no band gap. This band structure and the touched point are called Dirac cone and the Dirac point, respectively. For the linear dispersion, the effective mass approximation does not make sense. Hence, the electrons in graphene are often regarded as relativistic particles with zero mass, *i.e.*, massless Dirac fermions.

The equation (2.3) means the slope of energy band since it is obtained by differentiating the energy by k, that equals to the Fermi velocity. By combining the coefficient of γ_0 and the equation (2.3), the Fermi velocity v_F of graphene is derived to be

$$\hbar v_F = \frac{\sqrt{3}\gamma_0 a}{2} \tag{2.4}$$

where, $\hbar = h/2\pi$, h is the Planck constant ($\hbar$ is called the Dirac constant). Using γ_0 ~2.7 eV, the Fermi velocity $v_F \cong 10^6$ m/s, which is ~1/300 of the speed of light. This parameter v_F, even only one of parameter characterizing the energy band, dominantly determines the almost features of the electronic states of graphene.

2.1.2 Carrier transport property in graphene

In this section the electrical characteristics and carrier transport properties of graphene are introduced. Theoretically, the density of state (DOS) in graphene at the Dirac point is predicted to be zero. Under this condition, it is non-obvious whether the conductivity of graphene is zero or not. As considering the Fermi energy is not at the Dirac point by doping, the conductivity of graphene is calculated by the Boltzmann theory,

$$\sigma = g\frac{e^2\epsilon_F\tau}{4\pi\hbar^2} \tag{2.5}$$

where, g is the spin and valley degeneracy factor ($g = 4$), e is the elementary charge, ϵ_F is the Fermi energy, τ is the relaxation time for impurity scattering. This formula is analogous to the Drude conductivity for free electrons in the two dimensional system, indicating that the conductivity of graphene does not largely differ from the feature of free electrons. However, this can not be applied when the Fermi energy is at the Dirac point. From the uncertainty in the quantum mechanics theory, the energy can be considered as the scale of $\sim \hbar/\tau$, and then, the formula (2.5) becomes

$$\sigma = g\frac{e^2}{2h}. \tag{2.6}$$

Hence, graphene has the finite conductivity at the Dirac point. The conductivity σ does not contain the relaxation time τ, suggesting that the conductivity of graphene at the Dirac point is in the order of e^2/h independently from the disorder of system. In experiment, the finite conductivity of graphene at the Dirac point also has been observed, regarded as the presence of localized carriers due to the ripple structure of graphene or charged impurities in the substrate.

For doping in graphene, conductive carriers are easily activated by tuning the Fermi energy by applying the gate voltage. Moreover, the type of carrier can be switched between electrons and holes when the Fermi energy crosses the Dirac point, this feature is called the ambipolar characteristic.

Figure 2.3 shows the drain current-gate voltage characteristic of the graphene-based FET. In this U-shape curve, the minimum point corresponds to the Dirac point, which is called the charge neutrality point (CNP). The conductive carriers are electrons (holes) in the gate voltage range of the positive or right (negative or left) hand side from the CNP. The amount of carriers n induced by the applying gate voltage is described

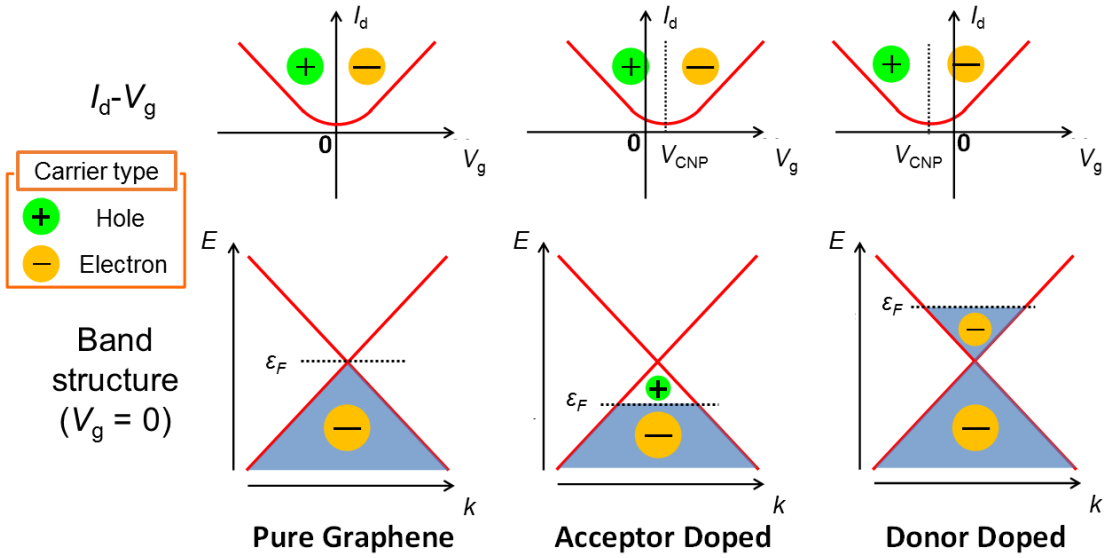

Figure 2.3: Gate modulation characteristic of graphene: Ambipolar characteristic.

by

$$n = \frac{C_g}{e}(V_g - V_{CNP}) \tag{2.7}$$

where, C_g is the gate capacitance, V_g is the gate voltage, and V_{CNP} is the voltage of the CNP.[2] In ideal case, the pure graphene exhibits the CNP at the zero gate voltage. However, the CNP is usually not found at zero in real experiments. Since graphene is not perfectly clean in experimental environments, the CNP is shifted to either side depending on the polarity of impurities, *i.e.*, doping to graphene. Hence, the doping state of graphene and the polarity of charged impurities can be characterized by observing the position of the CNP. The amount of carriers n_{imp} induced by charged impurities is extracted by

$$n_{imp} = \frac{C_g V_{CNP}}{e}. \tag{2.8}$$

The positive (negative) n_{imp} means that graphene is p-doped (n-doped).

As well-known, the electrons in graphene have very high mobility. In addition, the holes also have almost same mobility due to the symmetric band structure. The field effect mobility μ_{FE} of graphene device can be estimated by using the direct transconductance method,

$$\mu_{FE} = \frac{dI_d}{dV_g}\frac{L}{WC_g V_d} \tag{2.9}$$

where, I_{d} is the drain current, L and W are the length and width of the channel, respectively, and V_{d} is the source-drain bias voltage. Throughout this thesis, the mobility is extracted by this equation. Note that, this method,however, underestimates the mobility due to the influence of the contact resistance between graphene and metal contacts.

2.1.3 Single carrier tunneling through quantum dot systems

In this section, as the remarkable transport property in nanoscale structures, the single electron tunneling phenomena is described. Single electron tunneling is the effect reflecting the tunnel effect of single electron (one by one) to the electrical transport characteristics.[3,4] This effect is typically observed in the nanostructures such as the QD where one electron is three-dimensionally confined. These effect and QD structure are expected for the observation of physical phenomenon and nanoscale device applications.

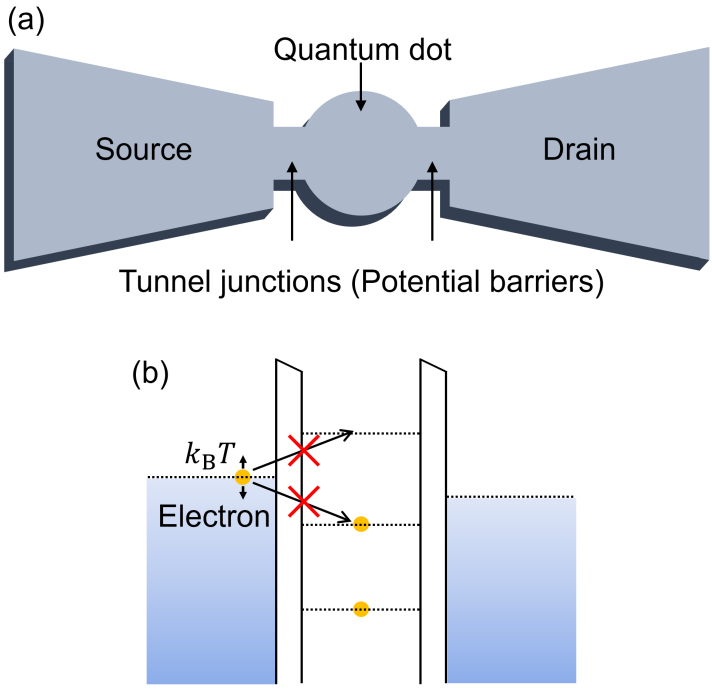

Figure 2.4: (a) Schematic structure of quantum device. The geometrically-defined quantum dot is connected to the source and the drain through the narrow constrictions, called tunnel junctions that are responsible for potential barriers. (b) Potential diagram of the quantum dot device under the finite source-drain bias voltage. Dotted lines represent the energy levels in the qunatum dot and Fermi energy at the source and the drain. The condition to occur Coulomb blockade is satisfied in this diagram.

Figure 2.4 shows the schematic structure and potential diagram of the QD device. In the dot, the energy level becomes discrete when the size of dot is comparable to the wavelength (de Broglie wave) of electron, and Coulomb interaction between electrons strongly works. For this reason, the charging energy that required to add one electron in the dot increases. If the charging energy is greater than the thermal energy k_BT (k_B is the Boltzmann constant, T is the temperature), the energy levels in the dot

below the Fermi energy of the source (under finite bias) are fully occupied, resulting that a new electron can not enter from the source into the dot (Fig. 2.4 (b)). This is called the Coulomb blockade effect. Between the source and dot, the drain and dot correspond to tunnel junctions, *i.e.*, potential barriers to confine the electron. Even though electrons can not pass through these barriers in the classical manner, they can be tunneling the barriers with a finite probability when the wave function of electrons seep into the opposite side of the barrier in the quantum manner. Assuming that the electrostatic capacitance of the junction system is C and the elementary charge is e, the change in the energy of the junction system before and after tunneling, which corresponds to the charging energy E_{C} is written as follows:

$$E_{\mathrm{C}} = \frac{e^2}{C}\,(J) = \frac{e}{C}\,(eV). \tag{2.10}$$

This energy means the difference in energy of the state of N electrons and that of $N+1$ electrons in the dot. Since the capacitance C decreases as the junction area decreases, a small tunnel junction and dot are required to increase the charging energy E_{C}. When the thermal energy of the system is sufficiently lower than the charging energy, E_{C} is the main energy scale that determines the tunnel probability.

Assuming that the charge Q is accumulated in the junctions, the electrostatic energy is given by $Q^2/2C$. When one electron tunnels, since Q is changed to $Q \pm e$, the change in electrostatic energy before and after tunneling ΔE is

$$\begin{aligned} \Delta E &= \frac{(Q \pm e)^2}{2C} - \frac{Q^2}{2C} \\ &= \frac{e}{C}(\frac{e}{2} \mp Q). \end{aligned} \tag{2.11}$$

Assuming $\Delta E > 0$, the electron tunneling is prohibited due to the electrostatic energy increases after tunneling,

$$-\frac{e}{2} < Q < \frac{e}{2}. \tag{2.12}$$

Here, considering $Q = CV$, the Eq. (2.12) becomes

$$-\frac{e}{2C} < V < \frac{e}{2C}. \tag{2.13}$$

Coulomb blockade occurred in this voltage range.

The conditions to cause the Coulomb blockade effect are mainly two as follows:

$$(1) \quad E_{\mathrm{C}} \gg k_{\mathrm{B}}T$$
$$(2) \quad R_{\mathrm{T}} \gg \frac{h}{e^2} \equiv R_{\mathrm{Q}}$$

where, R_{T} is the resistance of tunnel barrier, R_{Q} is the constant called quantum resistance. If R_{T} is sufficiently large, it means that the tunnel probability of electrons is sufficiently small. In such a case, the presence of electron can be distinguished which side against the barrier. This corresponds to the condition that tunneling electrons can be treated as particles having the quantized elementary charge.

Here the principle of the single electron transistor (SET) is described. The simplified equivalent circuit is shown in Fig. 2.5. The node sandwiched between the tunnel junctions corresponds to the QD.

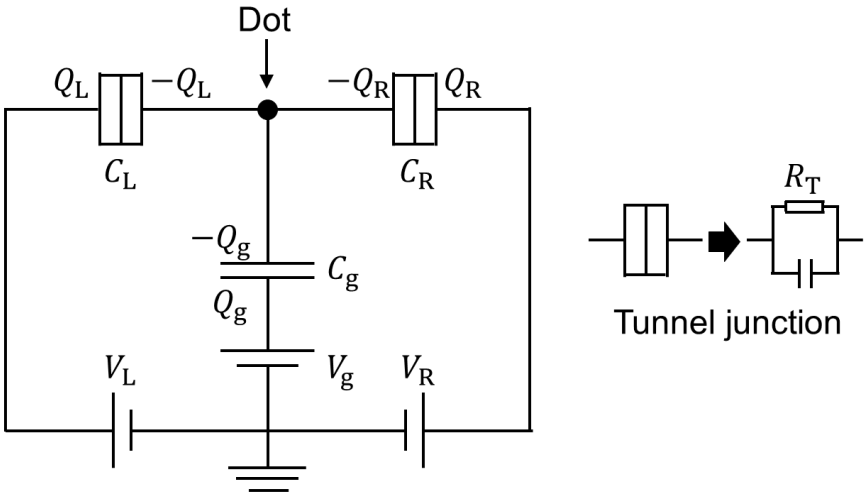

Figure 2.5: Equivalent circuit of the single electron transistor.

As considering the operation of single electron transport, the average current through the tunnel junctions is controlled by injecting charge into the dot by applying the gate voltage V_{g}. Assuming the capacitances of two tunnel junctions as C_{L}, C_{R} and the gate capacitance as C_{g}, and the charge accumulated outside the dot as Q_{L}, Q_{R} and Q_{g} as shown in Fig. 2.5, their relationships are followings:

$$Q_{\mathrm{L}} = C_{\mathrm{L}}V_{\mathrm{L}} \tag{2.14}$$
$$Q_{\mathrm{R}} = C_{\mathrm{R}}V_{\mathrm{R}} \tag{2.15}$$
$$Q_{\mathrm{g}} = C_{\mathrm{g}}V_{\mathrm{g}} \tag{2.16}$$

Assuming the number of electrons N, the charge in the dot $Q_{\rm D}$ is

$$Q_{\rm D} = -Ne = -Q_{\rm R} - Q_{\rm L} - Q_{\rm g}. \tag{2.17}$$

The amount of charge outside the dot is $-Q_{\rm D}$. Here, the total electrostatic capacitance C_Σ of the dot is

$$C_\Sigma \equiv C_{\rm R} + C_{\rm L} + C_{\rm g}. \tag{2.18}$$

Then, the charging energy $E_{\rm C}(N)$ can be written as follows:

$$E_{\rm C}(N) = \frac{Q_{\rm L}^2}{2C_{\rm L}} + \frac{Q_{\rm R}^2}{2C_{\rm R}} + \frac{Q_{\rm R}^2}{2C_{\rm R}} - (Q_{\rm L}V_{\rm L} + Q_{\rm R}V_{\rm R} + Q_{\rm g}V_{\rm g}) \tag{2.19}$$

$$= \frac{(Ne - Q_{\rm D})^2}{2C_\Sigma^2} - \frac{(C_{\rm L}V_{\rm L}^2 + C_{\rm R}V_{\rm R}^2 + C_{\rm g}V_{\rm g}^2}{2} \tag{2.20}$$

The difference of charging energy when the number of electrons in the dot changes N-1$\rightarrow N$ is the energy required for entering one electron into the dot.

$$\mu_N = E_{\rm C} - E_{\rm C}(N-1) = (N - \frac{1}{2} - \frac{Q_{\rm D}}{e})\frac{e^2}{C_\Sigma} \tag{2.21}$$

This energy μ_N is called the electrochemical potential, including the electrostatic potential.

The condition for the number of electron to be N in the QD is

$$\begin{aligned} \mu_N &< -eV_{\rm L} < \mu_{N+1} \\ \mu_N &< -eV_{\rm R} < \mu_{N+1}. \end{aligned} \tag{2.22}$$

Set $V_{\rm L} = -V_{\rm R} \equiv V/2$, and change Eq. (2.22) using (2.21),

$$e(N - \tfrac{1}{2}) < Q_{\rm D} - \tfrac{CV}{2} < e(N + \tfrac{1}{2}) \tag{2.23}$$

$$e(N - \tfrac{1}{2}) < Q_{\rm D} + \tfrac{CV}{2} < e(N + \tfrac{1}{2}) \tag{2.24}$$

Until here, only electrostatic energy is considered, ignoring the quantum confinement effect. To include this effect, the energy $E_{\rm add}(N)$ required to add one electron to the dot occupied N electrons is considered as follows:

$$E_{\rm add}(N) = \mu_{N+1} - \mu_N = E_{\rm C} + \Delta E \tag{2.25}$$

where, ΔE is the excitation energy, which represents the difference in energy between the two quantum discrete states, and μ_N is the electrochemical potential when the N-electrons occupy the dot. $\Delta E = 0$ means that energy states are degenerated.

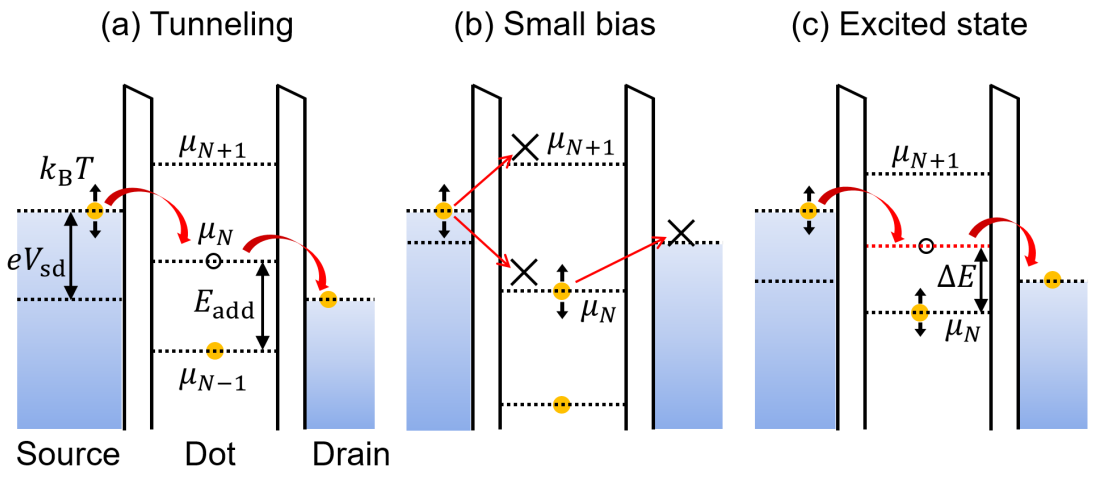

Figure 2.6: Diagram of energy levels and single electron tunneling.

(a) The electron can tunnel through the energy level of electrochemical potential μ_N.
(b) Tunneling of the electrons is prohibited since that the possible energy level in the QD does not exist in the bias window eV_d.
(c) The electron can tunnel through the excited state ΔE above the ground state.

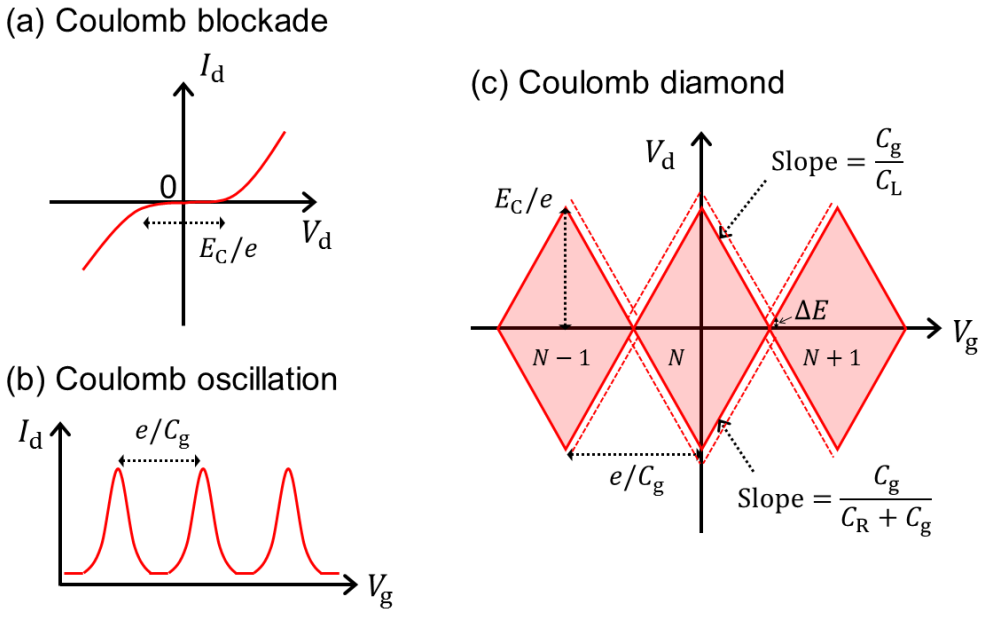

Figure 2.7: Coulomb blockade effects in transport measurements. (a) Coulomb blockade in the I_d-V_d characteristic with V_g in the constant. (b) Coulomb oscillation in the I_d-V_g characteristic with V_d in the constant. (c) Coulomb diamond in the V_d-V_g charge stability diagram. No current flow in the region inside the diamond shape. Dotted lines point to the signal of tunneling through the excited states.

In transport measurements, Coulomb blockade occurs in the range described in Eq. (2.13). This can be observed in the drain current-source-drain bias voltage (I_{d}-V_{d}) characteristic as shown in Fig. 2.7(a). The charging energy and capacitance of the system can be extracted from this characteristic.

As bias voltage V_{d} is fixed to a constant, the drain current I_{d} as a function of the gate voltage V_{g} exhibits the periodic peaks as shown in Fig. 2.7(b), this is called Coulomb oscillation. Since the spacing of the periodic current peaks is e/C_{g}, the gate capacitance can be extracted.

Fig. 2.7(c) shows Eq. 2.24 including Eqs. (2.14)$\sim$(2.17). This plot is called the charge stability diagram. The inside of the diamond structures indicated by the solid lines is the region where no current flows (Fig. 2.6(b)), *i.e.*, Coulomb blockade occurs, called Coulomb diamond. The dotted line corresponds to tunneling through the excited state, described in Fig. 2.6(c). From this stability diagram, ΔE, E_{add}, E_{C} are obtained.

In summary, it is possible to derive important parameters such as the charging energy, the gate capacitance, the excited states, etc. from the Coulomb diamond, oscillation characteristics. The observation of these characteristics is the strong evidence of that the system is being governed by single electron transport.

References

1) T. Enoki *et al.*, グラフェンが拓く材料の新領域, NTS (2012).

2) F. Schedin, A. K. Geim, S. V. Morozov, E. W. Hill, P. Blake, M. I. Katsnelson, K. S. Novoselov, Detection of individual gas molecules adsorbed on graphene. *Nat. Mater.* **6**, 652 (2007).

3) J. Haruyama, 単一電子トンネリング概論. コロナ社 (2003).

4) Y. Aoyagi, K. Ishibashi, H. Takayanagi, H. Nakano, Y. Hirayama, 基礎からわかるナノデバイス. コロナ社 (2011)

2.2 Literature review for related researches

2.2.1 Carrier localization and doping effects in graphene

Since graphene is truly a monolayer material, it is very sensitive for the surrounding environment.[1] In particular, it has recently been reported that the electrical characteristics of graphene change by the adsorption of only one gas molecule on the surface of graphene.[2] Therefore, graphene is expected for the application required for high sensitivity, such as sensors for volatile organic compounds gases. To put it the other way around, the electrical property of graphene for the external environment is, however, difficult to be stabilized. The mechanism of the change in the electrical property of graphene is due to the charge transfer from the surroundings, *i.e.*, doping effects.

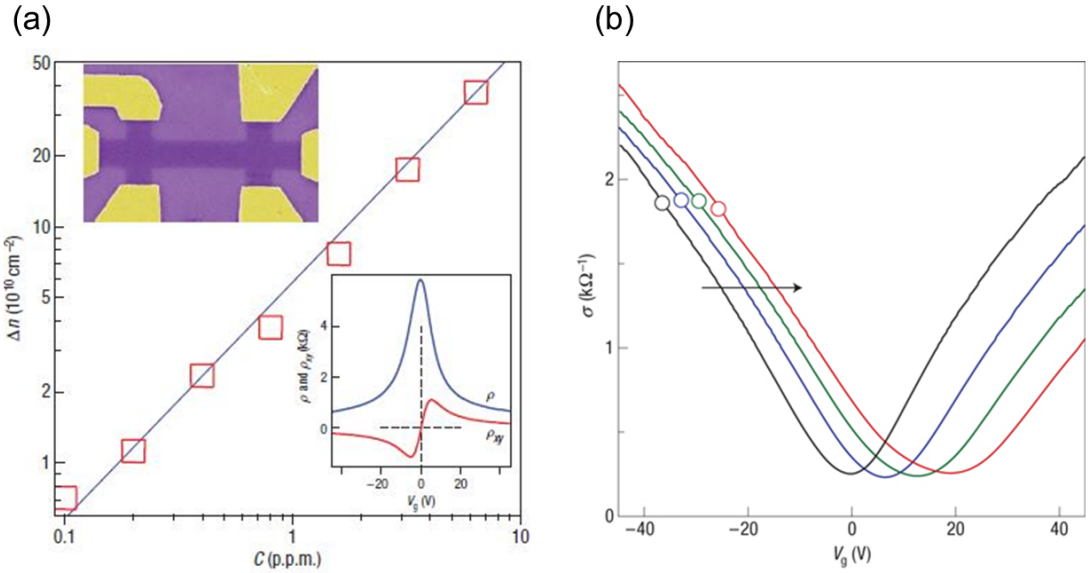

Figure 2.8: Gas sensing experiments on graphene.[1] (a) Doping-induced carrier density (Δn) of graphene as a function of the concentrations (C) of NO_2 gas. Upper inset shows SEM image of SLG-based Hall bar device with the width of 1 μm used in this measurement. Lower inset shows the longitudinal and Hall resistivity of graphene as a function of the gate voltage (V_g). (b) Conductivity (σ)-V_g characteristic of graphene in the NO_2 gas environments. The curves from black to red color show the increase in the concentration of NO_2 from zero to 1.5×10^{12} cm^{-1}.

In 2007, Schedin *et al.* reported that the gas sensing experiments in which the electrical characteristics of graphene were measured under the specific gas environments (Fig. 2.8).[1] In this experiments, the longitudinal

and Hall resistivity of graphene Hall bar device were changed when the device was exposed to the gas environment, and its quantity depended on the gas species. Furthermore, it was revealed that the shift of the CNP in the conductivity-gate voltage characteristic is enable to estimate the amount of adsorbed gas molecules and doping polarity, for example, NH_3 and CO acted as donors, while NO_2, O_2 and H_2O acted as accepters.[1,3]

The doping effects are caused not only by the adsorption of gas molecules, but also by the chemical residues on the surface of graphene and/or the interface of graphene and the substrate. Such as Poly(methyl methacrylate) (PMMA), an electron beam (EB) resist used for the device fabrication process, is known to induce p-doping in graphene.[4] The presence of water between graphene and SiO_2 substrate also causes p-doping in graphene.[5]

For reducing this doping effect, the annealing treatment method has been widely used for a lot of experiments. The annealing method can be distinguished to two as follows: (1) flowing large current to graphene,[6] and (2) annealing the sample using a furnace.[7] The former method (1) utilizes the Joule heating at the graphene channel, and is possible owing to the large current capability of graphene of 10^8 A/m.[8] This method has often been used for suspended graphene, effectively improving the carrier mobility.[9] However, in case for the graphene device on the SiO_2 substrate, the current-induced annealing method leads to the generation of dangling bonds on the SiO_2 surface, causing n-doping to graphene.[10]

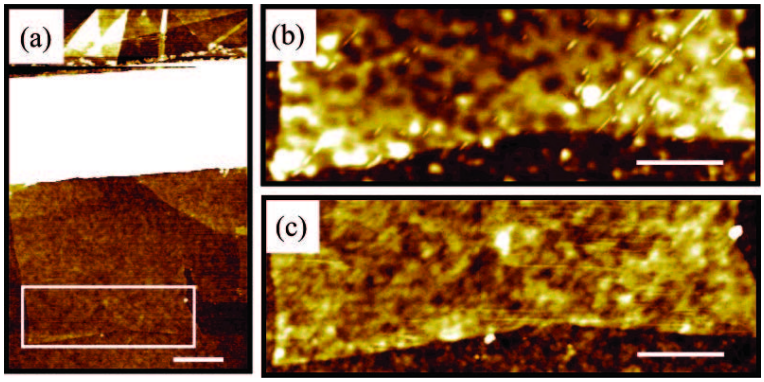

Figure 2.9: Cleaning graphene by annealing treatments.[7] (a) Atomic force microscopy image of the mechanically exfoliated graphene sheet on SiO_2. The scale bar represents 500 nm. (b) Graphene sheet before the annealing treatment. (c) Graphene sheet after the annealing treatment in Ar/H_2 atmosphere at 400°C. The graphene sheet becomes smoother corrugations. Both scale bars in (b) and (c) are 300 nm.

Regarding the latter annealing process (2), this method has been ex-

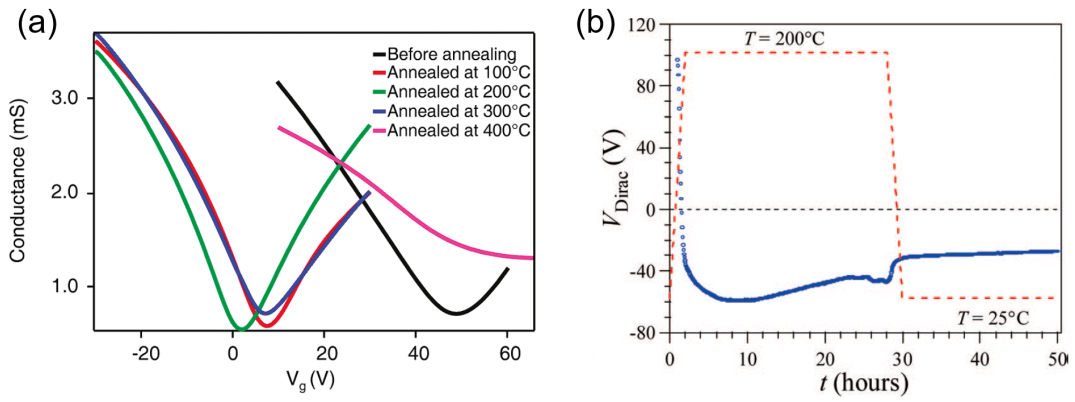

Figure 2.10: Doping effects after annealing. (a) Conductance of graphene as a function of V_g, measured under ambient conditions after annealing for various temperatures. The shift of the CNP to left hand side (relatively negative side) after annealing at 100, 200, 300°C indicates that annealing induces n-doping or reduce p-doping in graphene, while the positive shift of the CNP was shown after annealing at 400°C.[15] (b) Shift of the Dirac voltage (V_{Dirac} equals the CNP) of graphene FET on SiO_2 as a function of the annealing duration at 200°C, measured in the vacuum condition of $\sim 5 \times 10^{-5}$ Torr. The negative shift crossing $V_g = 0$ V of the CNP suggests that graphene is n-doped.[17]

tensively used in a lot of studies on graphene because it shows various improvement effects for graphene in spite of a simple method. For instance, annealing in a vacuum removes adsorbed molecules and polymeric residues from the graphene surface.[11] PMMA was shown to be effectively removed by annealing in hydrogen gas diluted by an inert gas (Ar or N_2).[7,12] Moreover, thermal annealing with argon gas cures defects in graphene owing to recombination of carbon adatoms with vacancies by thermal energy.[13] In addition, rapid thermal annealing improves the contact resistance of graphene-metal junctions.[14]

Even though many morphological effects of thermal annealing in graphene have been reported, the effects on the electronic transport properties of GFETs are still not fully understood, although some progress regarding the latter has been made in the past few years. It has been argued that vacuum annealing induces p-doping into graphene,[15,16] however, n-doping in graphene after vacuum annealing has been reported (Fig. 2.10)[17] This inconsistency has not yet been solved.

The doping effect also affects the carrier scattering properties in graphene. In 2008, Chen *et al.* reported that the characterization of charged-impurity scattering on transport properties of graphene by depositing potassium atoms onto the graphene surface.[18] As a result shown in Fig. 2.11, it turned

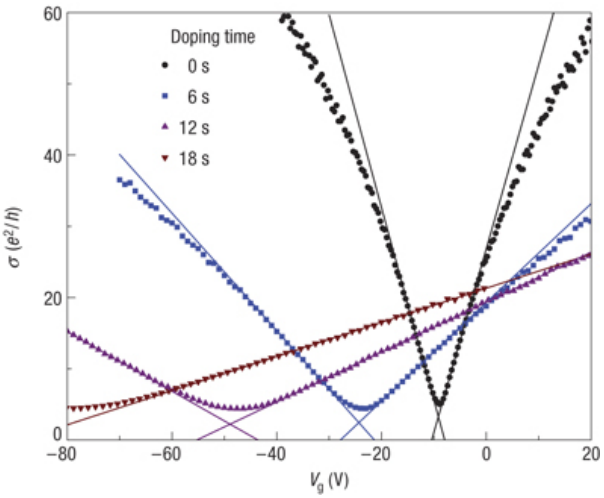

Figure 2.11: Impacts of charged-impurity scattering.[18] The σ-V_g characteristics of graphene in potassium with various concentrations, at 20 K in the ultrahigh vacuum condition. Lines are drawn using Eq. (2.26).

out that the higher the potassium doping concentration, the more the following tendency appears in the transport properties of graphene:

- The field-effect mobility decreases according to the following equation

$$\sigma = \begin{cases} \mu_e C_g (V_g - V_{CNP}) + \sigma_{res} & V_g > V_{CNP} \\ -\mu_h C_g (V_g - V_{CNP}) + \sigma_{res} & V_g < V_{CNP} \end{cases} \tag{2.26}$$

  where μ_e (μ_h) is the field-effect mobility of electron (hole), C_g is the gate capacitance per unit area, and σ_{res} is the residual conductivity.

- The dependence of conductivity on the carrier density (gate voltage) becomes linear at the high carrier density (gate voltage range far from the CNP).

- The mobility of electrons and holes get asymmetric.

- The CNP shifts to the negative gate voltage side.

- The conductivity-gate voltage curve around the CNP broadens.

- The minimum conductivity relatively decreases.

Although SiO_2 substrates which is widely used as a substrate for graphene devices, it is predicted that the condition of SiO_2 surface also induces doping in graphene.[17,19,20] For example, from the difference between the work

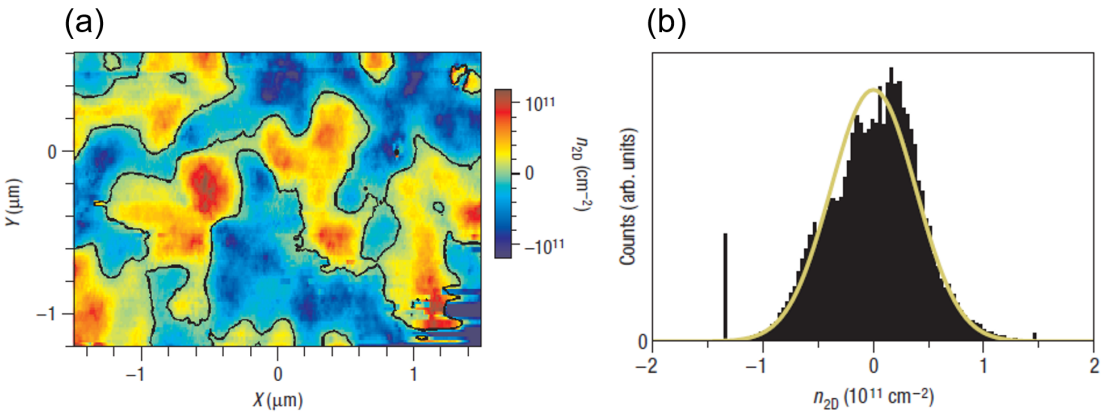

Figure 2.12: Observation of localized carrier puddles in graphene on SiO_2 by surface potential measurements.[21] (a) Mapping of carrier density distribution on graphene. The blue (red) area correspond to the electrons (holes) puddle. The black contour lines point to the zero carrier density. (b) Histogram of the carrier density distribution (n_{2D}) extracted from (a).

function of SiO_2 and graphene, charge is transferred from SiO_2 to graphene, resulting in n-doping to graphene.[17]

In 2008, Martin *et al.* reported that carriers in graphene are spatially-localized with the size of the order of 30 nm due to the potential inhomogeneity (Fig. 2.12).[21] These "carrier puddles" behave as pseudo QDs resulting in the irregular Coulomb blockade diamond characteristics observed in graphene nanodevices (introduced later). To minimize the influence of carrier doping and localization in graphene, the detailed investigation that how to reduce or avoid these effect is required.

Raman spectroscopy has also been used to evaluate doping properties.[22–25] Raman spectrum of graphene shows peaks originated from carbon materials such as G, D, and 2D peaks, whose intensity and shift allow to identify the type and amount of doping. The G peak shifts to the high energy side when graphene is either n-doped or p-doped as shown in Fig. 2.13, because the adiabatic Born-Oppenheimer approximation, which is fundamental to describe the interaction between electrons and nuclei, does not make sense for the doped graphene. It has also been observed that 2D peak shifts to high energy side for hole doping and low energy side for electron doping. However, the localized doping effect has been difficult to probed by Raman spectroscopy on the resolution smaller than the range of visible light wavelength owing to the diffraction limit of laser. Recently, the tip-enhanced Raman spectroscopy, which is the combination of atomic force microscopy

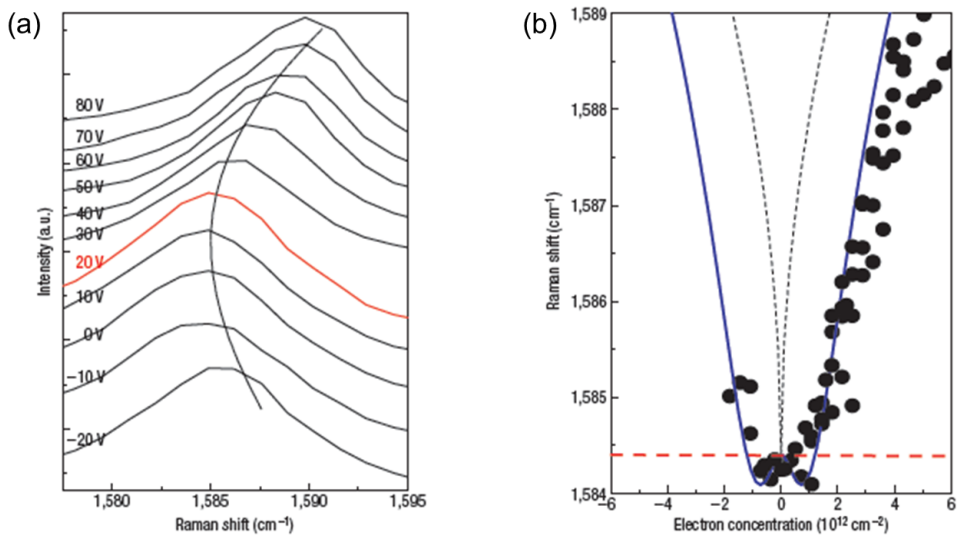

Figure 2.13: Doping effects on Raman spectroscopy of graphene.[22] (a) Dependence of the G peak on V_g at 295 K. The red signal (V_g = 20 V) corresponds to the undoped state (V_g at the CNP). (b) Center of G peak as a function of electron concentration at 295 K. Black circles show experimental data. Black dashed line simplified non-adiabatic calculation. Red dashed line exhibits the adiabatic Born-Oppenheimer approximation calculation. Blue line presents the non-adiabatic calculation.

and Raman spectroscopy, has been studied on graphene for investigating the local properties of graphene. This will be discussed in chapter 5.

2.2.2 Transport models of graphene nanoribbons

The absence of band gap in graphene is a major obstacle in applying graphene for conventional devices (such as switch, logic etc.) widely used in the current semiconductor industry. However, band gap can be opened by patterning graphene into ribbon structure with the width of nm scale. Actually, the effects for graphene formed the nanoribbon structure were theoretically predicted before graphene was experimentally establised in 2004. In 1996, there was a report that the band gap opens in the graphene nanoribbon (GNR) with the armchair geometry and the gap increases as narrowing the width of GNR like semiconductor, while the GNR with zigzag geometry is always metalic in the analytical model.[26]

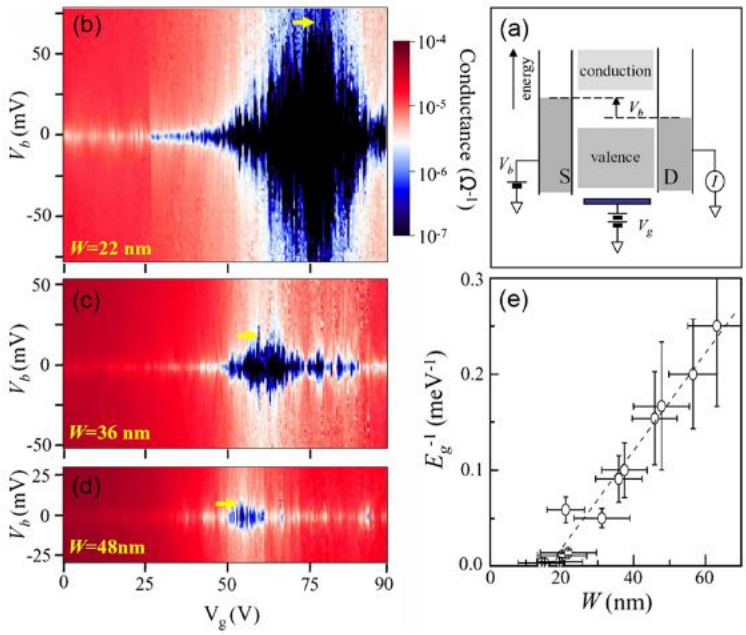

Figure 2.14: Dependence of the conductance on the width of GNR.[27] (a) Illustration of energy band diagram of the GNR applied source-drain bias voltage (V_b). (b) Charge stability diagrams of the GNRs with the width W of 22 nm, (c) 36 nm, and (d) 48 nm measured at 1.6 K. Dark colored regions correspond to low conductance, analogous to the Coulomb diamond characteristic. (e) Inversely energy gap (E_g^{-1}) as a function of W of GNR, obtained from (b)-(d). Dashed line is a linear fit.

The first experimental study on GNR was reported by Han *et al.* in 2007, and the change in the energy gap depending on width was observed as shown in Fig. 2.14.[27] The characteristics analogous to Coulomb blockade were observed in this report. In the same year, Sols *et al.* proposed the model to explain them that a neck was formed by roughness introduced into the graphene edge at the etching process, and the quantum dots

(QDs) structure was accidentally formed resulting in the observed Coulomb blockade characteristics.[28] Then, modeling of the conduction characteristics of GNR by Anderson localization and percolation model have been attempted.

In the theoretical model predicted that the energy gap E_g of graphene is inversely proportional to the width W of GNR following $E_g = \alpha / W$, where α is the constant of 0.2∼1.5 eV/nm, however, that can not explain both the larger gap when W is narrower than 20 nm and the current resonance peaks in the transport gap.

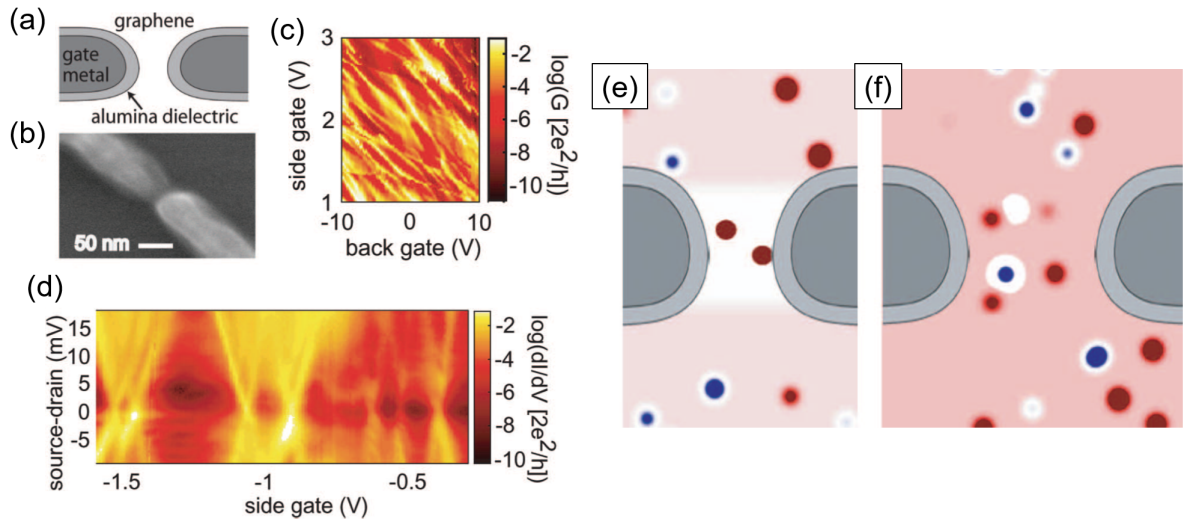

Figure 2.15: GNR transport measurement with metalic side-gates in close proximity at 4.2 K.[29] (a) Schematic of the device structure. (b) SEM image of the GNR device with L of 60 nm, and W of 15 nm, the metal side-gates. (c) Charge stability diagram using the sige-gate and back-gate measured. This is similar to the feature of DQD systems. (d) Coulomb diamond characteristics in charge stability diagram showing the excited state at the side gate voltage of ∼-1 V, and the feature of cotunneling at the side gate voltage of ∼-1.3 V. (e) Illustration of the carrier localization in a GNR with metal side-gates applying low voltage. Blue (red) color corresponds to heavily p-doped (n-doped) region. (f) (e) at high gate voltages. The constriction region becomes empty, leading to the less number of dots.

In 2009, three researches on the transport model of GNR were reported independently. Todd *et al.* fabricated the GNRs with the length L of 60-250 nm and W of 15-55 nm and showed its characteristics of Coulomb diamond at the temperature of 4.2 K as shown in Fig. 2.15.[29] For the observation of the excited state and inelastic cotunneling, those are not the characteristics of single tunnel barrier, it was therefore concluded that

QDs were formed in GNR and Coulomb blockade occurred. In addition, as a result of measuring the same device in different cooling cycles, the shape of Coulomb diamond, that is, the shape of the QDs changed suggesting that QDs were formed not only by the roughness of edges, but also by carrier localization, *i.e.*, local doping in graphene.

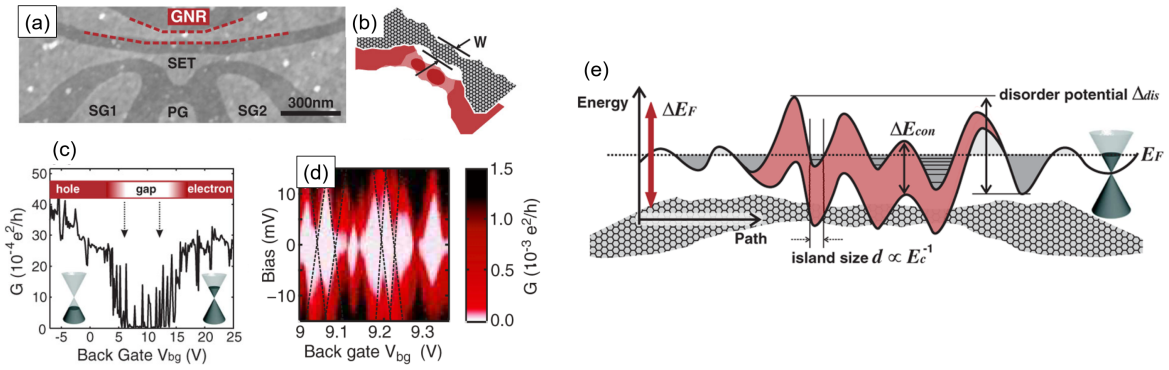

Figure 2.16: Measurements of the tunable GNR device with the SET and side-gates at 1.7 K.[30] (a) SEM image of the measured GNR device. The SET is located with the distance of ∼60 nm from the GNR. (b) Schematic illustration of an GNR with W and local charge islands on the GNR. (c) Conductance (G)-V_g characteristics. The transport gap in the center separates the regimes of electrons and holes transport. (d) Charge stability diagram of the GNR, showing the Coulomb diamond characteristics. (e) Drawing of the potential distribution along the GNR, which forms to the pseudo QDs leading to the large energy gap in the source-drain bias direction.

Stampfer *et al.* reported that Coulomb diamond was observed at 1.7 K in the GNR with L ∼1 um and W ∼45 nm as shown in Fig. 2.16.[30] The energy gap of 110-340 meV in the gate voltage direction (in current-V_g characteristics, called transport gap) was observed However, it does not match the theoretical prediction of ∼8 meV for W = 45 nm. This inconsistency is attributed to the strength of disorder potential of the whole GNR. In contrast, the energy gap appearing in the bias direction (in the plot of current as a function of source-drain bias voltage, called source-drain gap) followed the theoretically predicted value from the W inversely proportion.

Liu *et al.* fabricated a top gate on the GNR, which partially changed the carrier type or concentration such as p-type or n-type as shown in Fig. 2.17, and showed that Coulomb blockade appears strongly when carriers were switched in the middle of GNR.[31] In their study the GNRs were designed at L of 520-2000 nm and W of 40-60 nm, and the width of top gate is 50-

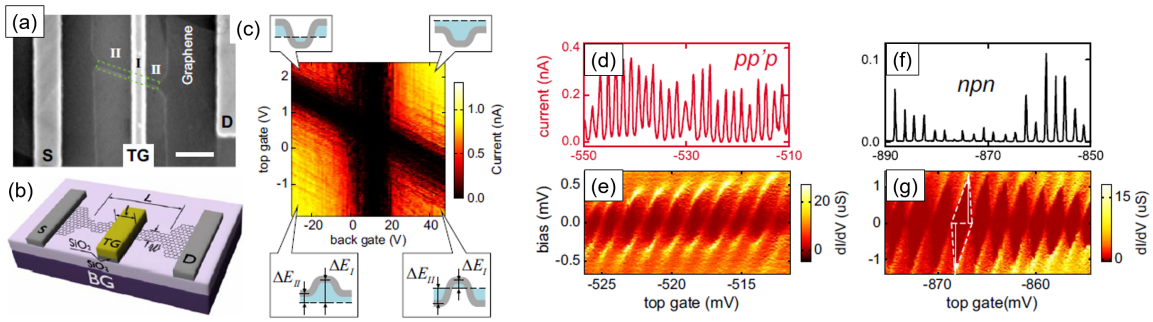

Figure 2.17: Measurements of the GNR device with the top-gate at 4 K.[31] (a) SEM image and schematic illustration of the GNR device. (c) Current as a function of the back gate and top gate voltages. Insets depict the potential landscapes for the four corners of the plot. Gray color indicates the transport gap. Dashed lines show the Fermi level. E_I and E_{II} represent the doping level under the top-gate and other regions of the GNR, respectively. (d),(e) Current as a function of top-gate voltage in the configuration of p-p′(high hole density)-p channel in the GNR. (f),(g) Current as a function of top-gate voltage in the configuration of n-p-n channel in the GNR, showing the stronger Coulomb blockade effect.

500 nm, and its transport properties were measured at 4 K. This indicates that the effective area of the QD is defined by the top gate, meaning that the carrier puddle functions as a QD.

In 2010, Gallagher *et al.* presented systematic study on the GNRs standardized W to 30 nm, L designed at 30-3000 nm, measured at 4.2 K, also performing the annealing process for the GNRs (Fig. 2.18).[32] As results, the following five trends were shown:

- Annealing changes the transport gap and the source-drain gap, those are no longer estimated from the GNR structure alone.
- The transport gap varies independently of the source-drain gap, which is contrast from the previous reports. The transport gap decreased by annealing suggesting that annealing might reduce the disorder potential strength of GNR, as considering the QD model.
- The transport gap approached the zero gate voltage after annealing, infering that the transport gap depended on doping.
- The source-drain gap increased as L got longer.
- Since Coulomb oscillation was observed, the QD model can be considered as more suitable for explaining the transport on GNR than the

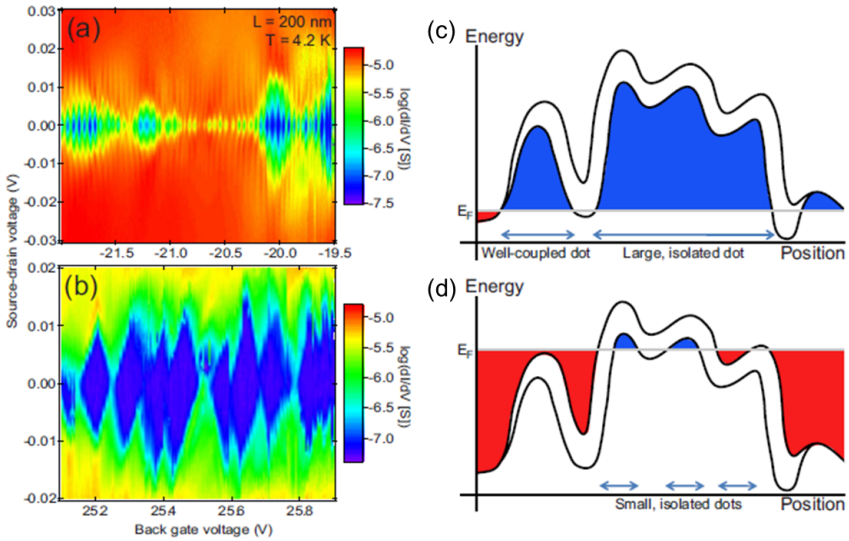

Figure 2.18: (a) Differential conductance on the back-gate voltage and source-drain bias voltage plot of the current-annealed GNR with L of 200 nm at 4.2 K.[32] Periodic Coulomb diamonds are observed. (b) Differential conductance of the same device as shown in (a) for the different range of back-gate voltage, where Coulomb oscillation peaks less periodicity. Overlapping diamond features for serial QDs can be observed. (c),(d) Schematic illustration of a potential distribution profile (Energy vs position along the GNR). In case of (c), a large isolated dot is formed leading to the periodic Coulomb oscillation characteristics. On the other hand, the configuration of (d) causes the formation of many QDs in the GNR resulting in the overlapping diamond behavior.

Anderson localization model.

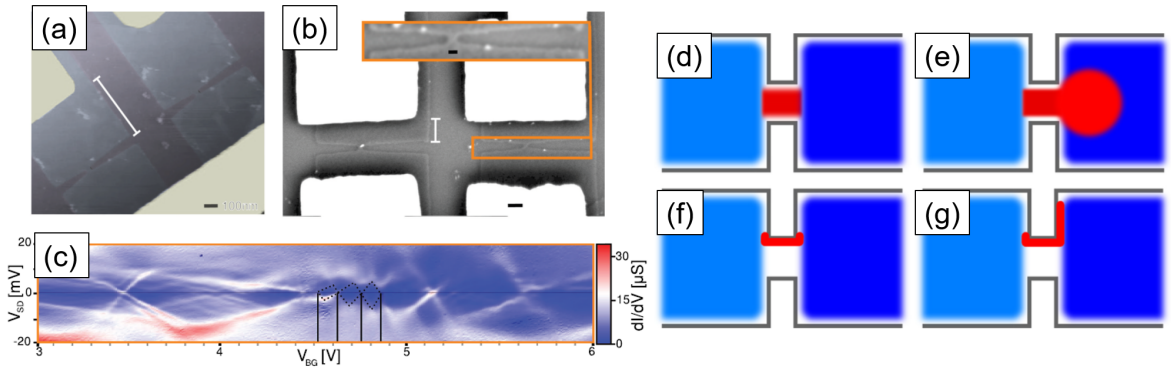

Figure 2.19: Transport property measurements of graphene nano-constrictions on h-BN.[33] (a),(b) SEM image of the four measured devices. Inset of (b) shows the magnified constriction region. (c) Differential conductance plot of the device measured at 1.3 K. Black lines emphasize the signals of Coulomb diamond. (d)-(g) Schematic illustration of possible localized states of wave function. Red color corresponds to the wave function. Blue region is the source and drain leads. The state of (g), carriers are localized along the constriction edge extending to the leads, is in agreement with the result of experiment and calculation.

In 2014, Bischoff *et al.* reported the transport properties on the constriction with $L \times W = 30$ nm $\times$ 30 nm made from the graphene on the h-BN substrate, measured at 1.3 K.[33] As results, the range of the quantum dots (localized carriers) estimated from the observed Coulomb diamond was beyond the area of constriction. As combination of the simulation of wave function, it was concluded that localization occurred along the edge of the constriction, which extended to the outside of the constriction as shown in Fig. 2.19.

According to the reports so far, Coulomb blockade has been observed in almost GNR devices at a cryogenic temperatures. This is due to the carrier localization, the edge roughness, the intensity of disorder potential, leading to the formation of unintentional pseudo QDs on the GNR.

2.2.3 Coulomb blockade in geometrically-defined graphene quantum dots

The devices used in the transport property experiments of QDs carried out with semiconductor materials can be mainly classified into two types. One is for a two-dimensional electron gas (2DEG), defining potential barriers forming the QD structure by creating depletion regions by applying voltage from top gates. This method is often used mainly in GaAs compound semiconductor-based heterojunction structures. Another method is the geometrically patterning of the QD structure by the lithography technique, where the QD is connected to the source and the drain through the narrow constrictions defining the tunnel barriers. This is often used for Si devices since the fine processing technology is well-established. In the case of graphene, in the former method, the absence of band gap and the Klein tunneling effect make difficult to confine the carrier of graphene into the potential barriers. Because the microfabrication technique used in Si devices is compatible to that of graphene, graphene QDs have been studied by the latter method.

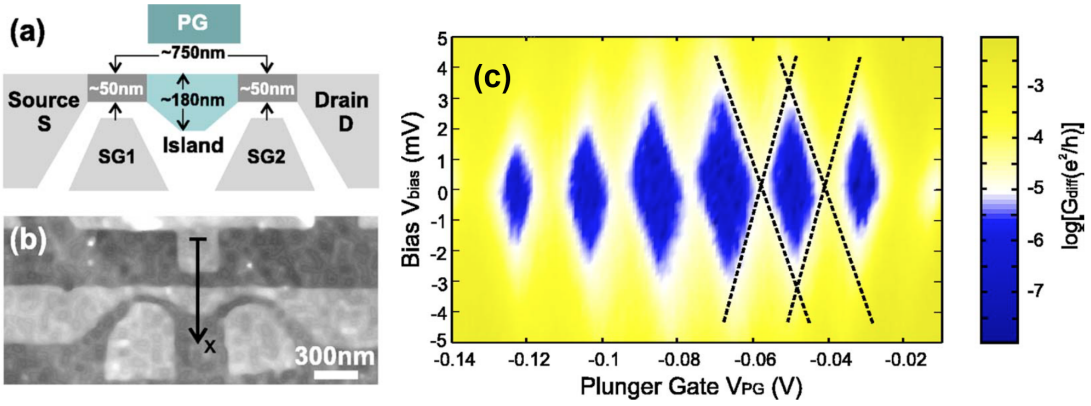

Figure 2.20: Coulomb blockade characteristics on the geometrically-defined graphene QD.[34] (a) Design of the QD device. (b) SEM image of the QD device. (c) Differential conductance as a function of the source-drain bias voltage (V_{bias}) and the side(plunger)-gate voltage (V_{PG}) at 1.7 K. Dotted lines draw the edge of the Coulomb diamond features.

The first experiment of the transport properties on the geometrically-defined graphene QD was reported by Stampfer *et al.* in 2008, the effect of Coulomb blockade, Coulomb oscillation and Coulomb diamond characteristics were observed at 1.7 K as shown in Fig. 2.20.[34] The lateral side gates provided the sufficient tunability to control the potential barrier. As

the energy scale such as charging energy did not significantly differ from that estimated from the geometrically definition, it was indicated that the transport properties were governed by the SQD system.

The researches on geometrically-defined SLG-based SQD[35–40] and DQD,[41–44] as well as SQD,[45–47] and DQD[44,48,49] made from BLG has been actively conducted by several groups. In addition, the trilayer graphene SQD[50] and DQD[51,52] have been less studied so far. For the research on geometrically-defined graphene QDs before 2012, the well-organized review article is available published by Güttinger *et al.* in 2012.[53]

In 2013, Wer *et al.* fabricated well-controllable graphene DQD using metal side-gates, which showed the honeycomb structure characteristic on the charge stability diagram at 35 mK (Fig. 2.21).[43] Even though successfully tuned the interdot tunnel coupling strength between two QDs with controlling the number of electron by applying voltage from the adjacent side-gate, the anomalous behavior was observed; although the tunneling coupling monotonically decreased as decreasing the number of electron inside the QD, it suddenly increased when the tuning gate voltage exceeds a certain voltage range. This is attributed to the edge state induced disorder, as shown to be inevitable in the etched GNR structures. The disorder varies the local electrochemical potential and can form randomly distributed localized carrier puddles, which may or may not contribute to the transport property of the DQD system. The metal side-gates can effectively control the electrostatic potential in the graphene DQD system. However, the capacitive coupling of the metal gate to the puddles can also discretely add or subtract charges to the pseudo QDs, thus suddenly and unexpectedly changing the transport properties. The carrier puddles induced by the disorder of GNR plays an important role for interdot tunnel coupling.

On the report by Bischoff *et al.* in 2013, the often fully-lifted Coulomb diamond characteristics were observed at 1.3 K on the ultra-fine BLG SQD device.[47] Even though it looks like SQD behavior, the signals originated from the coupled dots were observed in the stability diagram by side-gates. This behavior was explained by the model of the high order cotunneling occuring in the triple serial QDs (Fig. 2.22). It was consequently suggested that the QD was formed not only in the geometrically-defined structure, even also in the constrictions with very high precision.

According to these literatures, it can be considered two methods for defining the SQD in graphene. One is to use a BLG whose carrier has a finite effective mass and the band gap can be opened by applying vertical

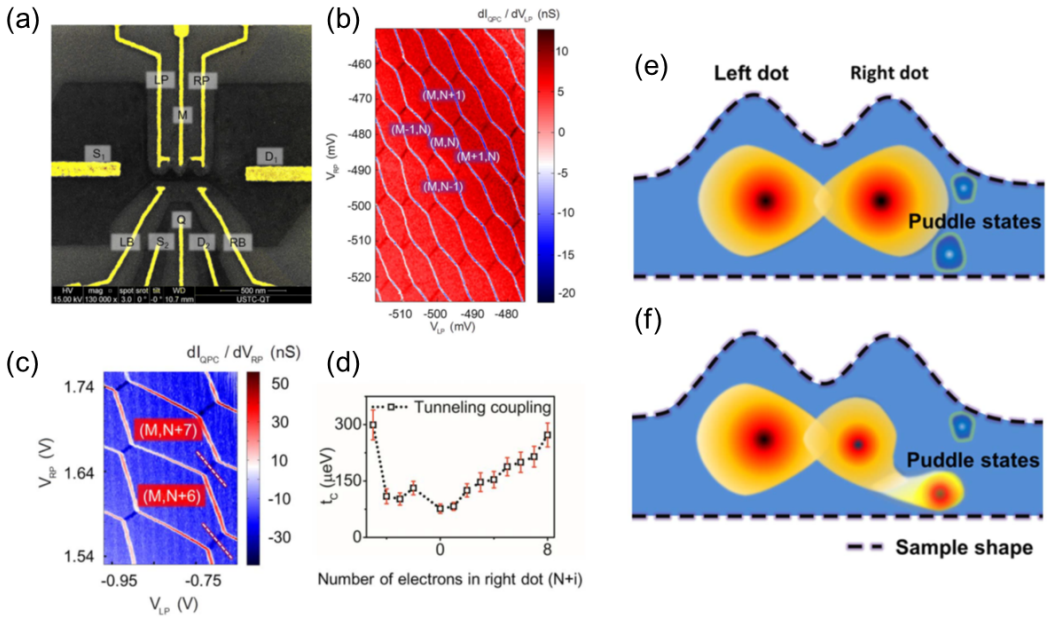

Figure 2.21: Tunable graphene DQD with metal side-gates.[43] (a) SEM image of the device. (b) Charge stability diagram at 35 mK. Honeycomb structure, the feature of the transport on the DQD system can be clearly observed. (c) Region for characterizing the dependence of interdot tunnel coupling (t_c) on the number of electron in QDs. (d) t_c as a function of the number of electrons in right dot (N + i). For (N + i) 0, t_c monotonically increases as increasing the number of electrons. For (N + i) 0, large number of electrons, the non-monotonic change in t_c is observed. (e),(f) Schematic drawing of the influence of localized carrier puddles on t_c. Puddle states induced by disorder of a GNR cause the distortion of the wave function of an electron in DQD as shown in (f), leading to the non-monotonic behavior of t_c.

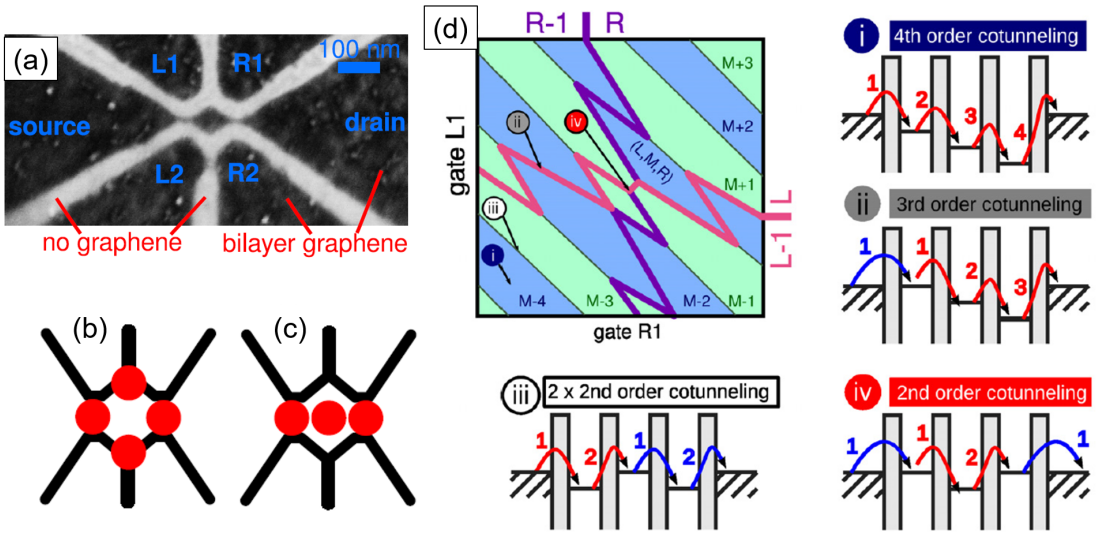

Figure 2.22: Study on the BLG-based SQD devices with constrictions in ultrahigh precision.[47] (a) SEM image of the measured device. (b),(c) Possible situation of the localized site distributed in the geometrically-defined QD structure. (d) Charge stability diagram for the transport model based on the triple QDs system. Purple (pink) line corresponds to the change in the number of electrons in the right (left) dot. Green (blue) region represents constant numbers of electrons in the center dot. Energy diagrams of four different situations are shown as (i)-(iv).

electric field. If energetically defining the QD by potential control without physical etching, the disorder and roughness at the graphene edge should be avoided.[54,55] Another way is to find the minimum required structure for the SQD formation in graphene. Considering the reports on the GNR, it seems that the nano-constriction structure would be a good candidate. Since the nano-constriction is the most principle building block of nanodevices, it must be worth investigating its properties in detail.

References

1) F. Schedin, A. K. Geim, S. V. Morozov, E. W. Hill, P. Blake, M. I. Katsnelson, K. S. Novoselov, Detection of individual gas molecules adsorbed on graphene. *Nat. Mater.* **6**, 652 (2007).

2) J. Sun, M. Muruganathan, H. Mizuta, Room temperature detection of individual molecular physisorption using suspended bilayer graphene. *Sci. Adv.* **2**, e1501518 (2016).

3) O. Leenaerts, B. Partoens, F. M. Peeters, Adsorption of H_2O, NH_3, CO, NO_2, and NO on graphene: A first-principles study. *Phys. Rev. B* **77**, 125416 (2008).

4) A. Pirkle, J. Chan, A. Venugopal, D. Hinojos, C. W. Magnuson, S. McDonnell, L. Colombo, E. M. Vogel, R. S. Ruoff, R. M. Wallace, The effect of chemical residues on the physical and electrical properties of chemical vapor deposited graphene transferred to SiO_2. *Appl. Phys. Lett.* **99**, 122108 (2011).

5) H. Komurasaki, T. Tsukamoto, K. Yamazaki, T. Ogino, *J. Phys. Chem. C* **116**, 10084 (2012).

6) J. Moser, A. Barreiro, A. Bachtold, Current-induced cleaning of graphene. *Appl. Phys. Lett.* **91**, 163513 (2007).

7) M. Ishigami, J. H. Chen, W. G. Cullen, M. S. Fuhrer, E. D. Williams, Atomic structure of graphene on SiO_2. *Nano Lett.* **7**, 1643 (2007).

8) K. S. Novoselov, A. K. Geim, S. V. Morozov, D. Jiang, Y. Zhang, S. V. Dubonos, I. V. Grigorieva, A. A. Firsov, Electric field effect in atomically thin carbon films. *Science* **306**, 666 (2004).

9) K. I. Bolotin, K.J. Sikes, Z. Jiang, M. Klima, G. Fudenberg, J. Hone, P. Kim, H. L. Stormer, Ultrahigh electron mobility in suspended graphene. *Solid State Commun.* **146**, 351 (2008).

10) P. Kumar, A. Kumar, *Appl. Phys. Lett.* **104**, 083517 (2014).

11) K. Kumar, Y. S. Kim, E. H. Yang, The influence of thermal annealing to remove polymeric residue on the electronic doping and morphological characteristics of graphene. *Carbon* **65**, 35 (2013).

12) Y. C. Lin, C. C. Lu, C. H. Yeh, C. Jin, K. Suenaga, P. W. Chiu, Graphene annealing; How clean can it be? *Nano Lett.* **12**, 414 (2012).

13) J. Chen, T. Shi, T. Cai, T. Xu, L. Sun, X. Wu, D. Yu, Self healing of defected graphene. *Appl. Phys. Lett.* **102**, 103107 (2013).

14) O. Balci, C. Kocabas, Rapid thermal annealing of graphene-metal contact. *Appl. Phys. Lett.* **101**, 243105, (2012).

15) Z. Cheng, Q. Zhou, C. Wang, Q. Li, C. Wang, Y. Fang, Toward intrinsic graphene surfaces: A systematic study on thermal annealing and wet-chemical treatment of SiO_2-supported graphene devices. *Nano Lett.* **11**, 767 (2011).

16) Z. H. Ni, H. M. Wang, Z. Q. Luo, Y. Y. Wang, T. Yu, Y. H. Wu, Z. X. Shen, The effect of vacuum annealing on graphene. *J. Raman Spectrosc.* **14**, 479, (2010).

17) H. E. Romero, N. Shen, P. Joshi, H. R. Gutierrez, S. A. Tadigadapa, J. O. Sofo, P. C. Eklund, *ACS Nano* **2**, 2037 (2008).

18) J. H. Chen, C. Jang, S. Adam, M. S. Fuhrer, E. D. Williams, M. Ishigami, Charged-impurity scattering in graphene. *Nat. Phys.* **4**, 377 (2008).

19) Y. Shi, X. Dong, P. Chen, J. Wang, L. J. Li, Effective doping of single-layer graphene from underlying SiO_2 substrates. *Phys. Rev. B* **79**, 115402 (2009).

20) Y. J. Kang, J. Kang, K. J. Chang, Electronic structure of graphene and doping effect on SiO_2. *Phys. Rev. B* **78**, 115404 (2008).

21) J. Martin, N. Akerman, G. Ulbricht, T. Lohmann, J. H. Smet, K. Von Klitzing, A. Yacoby, Observation of electronhole puddles in graphene using a scanning single-electron transistor. *Nat. Phys.* **4**, 144 (2008).

22) S. Pisana, M. Lazzeri, C. Casiraghi, K. S. Novoselov, A. K. Geim, A. C. Ferrari, F. Mauri, Breakdown of the adiabatic BornOppenheimer approximation in graphene. *Nat. Mater.* **6**, 198 (2007).

23) C. Casiraghi, S. Pisana, K. S. Novoselov, A. K. Geim, A. C. Ferrari, Raman fingerprint of charged impurities in graphene. *Appl. Phys. Lett.* **91**, 233108 (2007).

24) A. Das, S. Pisana, B. Chakraborty, S. Piscanec, S. K. Saha, U. V. Waghmare, K. S. Novoselov, H. R. Krishnamurthy, A. K. Geim, A. C. Ferrari, A. K. Sood, Monitoring dopants by Raman scattering in an electrochemically top-gated graphene transistor. *Nat. Nanotech.* **3**, 210 (2008).

25) M. Lazzeri, F. Mauri, Nonadiabatic Kohn anomaly in a doped graphene monolayer. *Phys. Rev. Lett.* **97**, 266407 (2006).

26) K. Nakada, M. Fujita, G. Dresselhaus, M. S. Dresselhaus, Edge state in graphene ribbons: Nanometer size effect and edge shape dependence. *Phys. Rev. B* **54**, 17954 (1996).

27) M. Y. Han, B. Özyilmaz, Y. Zhang, P. Kim, Energy band-gap engineering of graphene nanoribbons. *Phys. Rev. Lett.* **98**, 206805 (2007).

28) F. Sols, F. Guinea, A. H. Castro Neto, Coulomb blockade in graphene nanoribbons. *Phys. Rev. Lett.* **99**, 166803 (2007).

29) K. Todd, H. T. Chou, S. Amasha, D. Goldhaber-Gordon, Quantum dot behavior in graphene nanoconstrictions. *Nano Lett.* **9**, 416 (2009).

30) C. Stampfer, J. Güttinger, S. Hellmüller, F. Molitor, K. Ensslin, and T. Ihn, Energy gap in etched graphene nanoribbons. *Phys. Rev. Lett.* **102**, 056403 (2009).

31) X. Liu, J. B. Oostinga, A. F. Morpurgo, L. M. K. Vandersypen, Electrostatic confinement of electrons in graphene nanoribbons. *Phys. Rev. B* **80**, 121407(R) (2009).

32) P. Gallagher, K. Todd, D. Goldhaber-Gordon, Disorder-induced gap behavior in graphene nanoribbons. *Phys. Rev. B* **81**, 115409 (2010).

33) D. Bischoff, F. Libisch, J. Burgdörfer, T. Ihn, K. Ensslin, Characterizing wave functions in graphene nanodevices: Electronic transport

through ultrashort graphene constrictions on a boron nitride substrate. *Phys. Rev. B* **90**, 115405 (2014).

34) C. Stampfer, J. Güttinger, F. Molitor, D. Graf, T. Ihn, K. Ensslin, Tunable Coulomb blockade in nanostructured graphene. *Appl. Phys. Lett.* **92**, 012102 (2008).

35) L. A. Ponomarenko, F. Schedin, M. I. Katsnelson, R. Yang, E. W. Hill, K. S. Novoselov, A. K. Geim, Chaotic Dirac billiard in graphene quantum dots. *Science* **320**, 356 (2008).

36) C. Stampfer, E. Schurtenberger, F. Molitor, J. Güttinger, T. Ihn, K. Ensslin, Tunable graphene single electron transistor. *Nano Lett.* **8**, 2378 (2008).

37) J. Güttinger, C. Stampfer, T. Frey, T. Ihn, K. Ensslin, Graphene quantum dots in perpendicular magnetic fields. *Phys. Status Solidi B* **246**, 2553 (2009).

38) J. Güttinger, C. Stampfer, F. Libisch, T. Frey, J. Burgdörfer, T. Ihn, K. Ensslin, Electron-hole crossover in graphene quantum dots. *Phys. Rev. Lett.* **103**, 046810 (2009).

39) J. Güttinger, T. Frey, C. Stampfer, T. Ihn, K. Ensslin, Spin states in graphene quantum dots. *Phys. Rev. Lett.* **105**, 116801 (2010).

40) L. J. Wang, G. Cao, T. Tu, H. O. Li, C. Zhou, X. J. Hao, Z. Su, G. C. Guo, H. W. Jiang, G. P. Guo, A graphene quantum dot with a single electron transistor as an integrated charge sensor. *Appl. Phys. Lett.* **97**, 262113 (2010).

41) F. Molitor, S. Dröscher, J. Güttinger, A. Jacobsen, C. Stampfer, T. Ihn, K. Ensslin, Transport through graphene double dots. *Appl. Phys. Lett.* **94**, 222107 (2009).

42) F. Molitor, H. Knowles, S. Dröscher, U.Gasser, T. Choi, P. Roulleau, J. Güttinger, A. Jacobsen, C. Stampfer, K. Ensslin, T. Ihn, Observation of excited states in a graphene double quantum dot. *Europhys. Lett.* **89**, 67005 (2010).

43) D. Wei, H. O. Li, G. Cao, G. Luo, Z. X. Zheng, T. Tu, M. Xiao, G. C. Guo, H. W. Jiang, G. P. Guo, Tuning inter-dot tunnel coupling of

an etched graphene double quantum dot by adjacent metal gates. *Sci. Rep.* **3**, 3175 (2013).

44) L. J. Wang, G. P. Guo, D. Wei, G. Cao, T. Tu, M. Xiao, G. C. Guo, A. M. Chang, Gates controlled parallel-coupled double quantum dot on both single layer and bilayer graphene. *Appl. Phys. Lett.* **99**, 112117 (2011).

45) S. Dröscher, J. Güttinger, T. Mathis, B. Batlogg, T. Ihn, K. Ensslin, High-frequency gate manipulation of a bilayer graphene quantum dot. *Appl. Phys. Lett.* **101**, 043107 (2012).

46) S. Fringes, C. Volk, C. Norda, B. Terrés, J. Dauber, S. Engels, S. Trellenkamp, C. Stampfer, Charge detection in a bilayer graphene quantum dot. *Phys. Status Solidi B* **248**, 2684 (2011).

47) D. Bischoff, A. Varlet, P. Simonet, T. Ihn, K. Ensslin, Electronic triple-dot transport through a bilayer graphene island with ultrasmall constrictions. *New J. Phys.* **15**, 083029 (2013).

48) C.Volk, S. Fringes, B. Terrrés, J. Dauber, S. Engels, S. Trellenkamp, C. Stampfer, Electronic excited states in bilayer graphene double quantum dots. *Nano Lett.* **11**, 3581 (2011).

49) L. J. Wang, H. O. Li, T. Tu, G. Cao, C. Zhou, X. J. Hao, Z. Su, M. Xiao, G. C. Guo, A. M. Chang, G. P. Guo, Controllable tunnel coupling and molecular states in a graphene double quantum dot. *Appl. Phys. Lett.* **100**, 022106 (2012).

50) J. Güttinger, C. Stampfer, D. Graf, T. Ihn, K. Ensslin, Coulomb oscillations in three-layer graphene nanostructures. *New J. Phys.* **10**, 125029 (2008).

51) S. Moriyama, D. Tsuya, E. Watanabe, S. Uji, M. Shimizu, T. Mori, T. Yamaguchi, K. Ishibashi, Coupled quantum dots in a graphene-based two-dimensional semimetal. *Nano Lett.* **9**, 2891 (2009).

52) S. Moriyama, Y. Morita, E. Watanabe, D. Tsuya, S. Uji, M. Shimizu, K. Ishibashi, Fabrication of quantum-dot devices in graphene. *Sci. Technol. Adv. Mater.* **11**, 054601 (2010).

53) J. Güttinger, F. Molitor, C. Stampfer, S Schnez, A Jacobsen, S. Dröscher, T. Ihn, K. Ensslin, Transport through graphene quantum dots. *Rep. Prog. Phys.* **75**, 126502 (2012).

54) A. M. Goossens, S. C. M. Driessen, T. A. Baart, K. Watanabe, T. Taniguchi, L. M. K. Vandersypen, Gate-defined confinement in bilayer graphene-hexagonal boron nitride hybrid devices. *Nano Lett.* **12**, 4656 (2012).

55) M. T. Allen, J. Martin, A. Yacoby, Gate-defined quantum confinement in suspended bilayer graphene. *Nat. Commun.* **3**, 934 (2012).

Chapter 3

Experimental methods

3.1 Fabrication of graphene devices

In this section the fabrication process of graphene devices is described. In general, graphene devices have been fabricated on a Si substrate covered with SiO_2. The Si layer is heavily doped (whichever p or n type) to use as a back-gate for electrical measurements, and the thickness of SiO_2 layer of around 90 nm or 300 nm are widely used because the optical contrast between graphene and SiO_2 substrate is enhanced resulting in graphene to be visible in optical microscopy.[1] We purchase such a SiO_2/Si wafer, heavily n-doped (As) Si covered with ∼300 nm thick SiO_2 (IDB Technologies Ltd., UK). The general fabrication process flow is shown below.

1. Preparation of substrate chips
2. Fabrication of alignment marks
3. Mechanical exfoliation for graphene
4. Confirm the quality and location of graphene
5. Fabrication of metal contact electrodes
6. Etching into nanostructures

Note that the step 5 (electrode fabrication process) can be exchanged with the step 6 (etching process). If the electrode is fabricated ahead, the metal contacts cover a part of bulk graphene, which makes the stability of graphene in the lift-off process. However, an electron beam (EB) resist could not be uniform around graphene, resulting in poor resolution in a patterning structure. On the other hand, if the etching process is former,

an EB resist is uniformly coated leading to the high resolution patterning. Instead of this advantage, due to graphene already in a nanostructure, there is a risk to peel out in the followed lift-off process. This trade-off relation should be considered for the yield of devices on a same chip.

Preparation of substrate chips

The substrate is required to dice into the size of 1 cm × 1 cm or 1.5 cm × 2 cm to perform an electron beam lithography (EBL) process in our system (ELS-7500, ELIONIX INC., Japan). Before dicing, an optical resist is coated on a polished side of the wafer for protecting its surface from damage. The wafer is diced into the small chips using the dicing machine (A-WD-10B, Tokyo Seimitsu Co., Ltd., Japan). After dicing, the SiO_2 layer on the back side of the chip is etched away by reactive ion etching (RIE) with CF_4 plasma. The chip is cleaned with acetone, isopropyl alcohol (IPA), and deionized water (DIW) to remove the optical resist. Piranha clean using hydrogen peroxide (H_2O_2) and sulfuric acid (H_2SO_4) is then performed to remove contaminations from the chip.

Fabrication of alignment marks

Alignment marks are used for (1) identifying the location of graphene flakes after exfoliation, (2) and using the registration function in the EBL system to align the position of exposure patterns. First, Poly(methyl methacrylate) (PMMA) and methyl methacrylate (MMA), bilayer EB resists are coated on the chip. EBL and development using methyl isobutyl ketone (MIBK):IPA = 1:1 are conducted. Then, Cr = 5 nm and Au = 100 nm are deposited by EB evaporation. The chip is immersed in N-methyl-2-pyrrolidone (NMP) for overnight. After that, ultrasonic cleaning is performed to remove resists with above metals.

Mechanical exfoliation for graphene

Graphene flakes are obtained by mechanical exfoliation[2] using an adhesive tape applied to a highly oriented pyrolytic graphite (HOPG) (Bruker, USA). The dicing tape (Adwill d-638, Lintec Co., Japan) is used for this process. The chip is heated on a hot plate at 180°C for 5 mins to remove water molecules from its surface. HOPG flakes are put on the tape and peeled many time until shades of colors are uniform. Then, the tape is stuck on the chip, and gently pressed from front and back sides of the chip,

and consequently, peeled slowly out from the chip. After that, the chip is dipped in hot acetone at 50°C for 30 mins, followed by IPA and DIW to remove tape residues.

Confirm the quality and location of graphene

The location and the number of graphene layers are identified by optical microscopy and Raman spectroscopy. In optical microscopy, the contrast of graphene flakes to the SiO_2 substrate depends on the numbers of graphene layers, because the transparency of a graphene layer for light is discrete.[5] Hence, the numbers of layer can be roughly estimated in optical images. The pictures consisting of graphene and more than two alignment marks are taken by optical microscope, since these directly influence the accuracy in the design of device structures.

The number of graphene layers is identified more precisely by Raman spectroscopy, which also characterize many kind of quality of graphene.[3] In Raman spectroscopy using Invia Raman spectrometer (Renishaw plc, UK) and T64000 (Horiba, Ltd., Japan) with a neodymium-doped yttrium-aluminum-garnet (Nd:YAG) laser whose wave length is 532 nm, Raman spectra are measured in the range of 1000∼3000 cm^{-1} to cover the specific Raman peaks, called the D, G and 2D peaks. The D peak located ∼1345 cm^{-1} originates in the double resonance of the second-order process between different valleys around $\mathbf{K}$ and $\mathbf{K}'$ in the Brillouin zone (intervalley scattering), which corresponds to the A_{1g} breathing mode at $\mathbf{K}$, the in-plane transverse optical phonon. The activation of the D peak requires defects, disorders or edges with armchair geometry. Therefore, graphene flakes without the D peak are selected for further device fabrication. The G peak caused by the doubly-degenerated E_{2g} vibration mode at the Brillouin zone center in the first-order Raman scattering process emerges around 1580 cm^{-1}, whose intensity increases with the number of layers increases. The peak at ∼2700 cm^{-1} is the 2D peak (or called G′ peak), arising from triple resonant process of the second-order intervalley scattering. Although the 2D peak corresponds to the overtone of the D peak, it is not required neither defects nor disorder for activation. The number of graphene layers is identified by fitting to the 2D peak, which has different profile shape with respect to the number of layers. In case of SLG, the 2D peak can be fitted with a single Lorentzian function whose full width at half maximum (FWHM) around 30 cm^{-1}. In case of BLG, four Lorentzian components

are needed for fitting because of the four processes involved phonons with different momenta. Hence, at least, SLG can be clearly distinguished from others.[4]

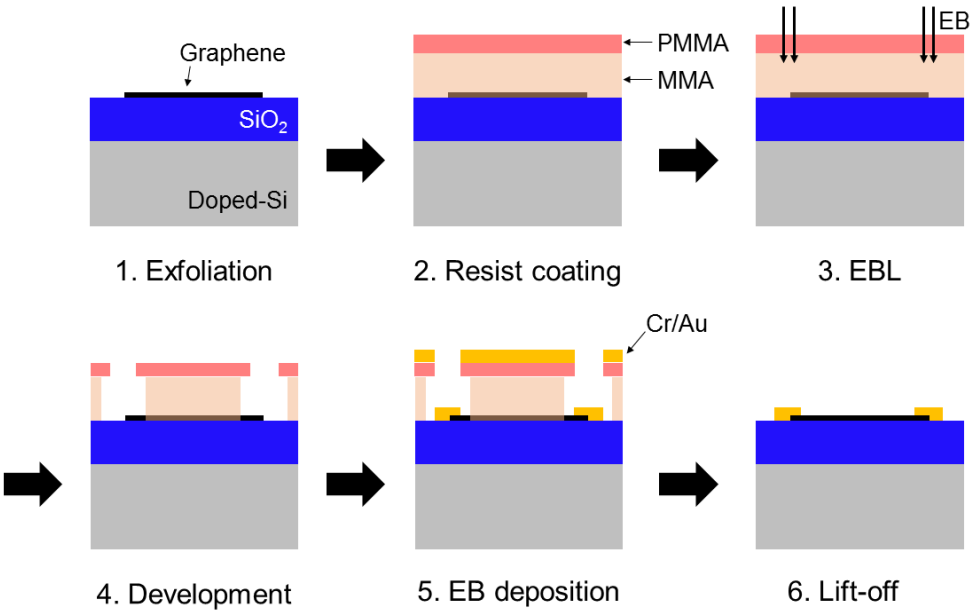

Figure 3.1: Fabrication process flow for electrodes.

Fabrication of metal contact electrodes

The next step is fabrication of the metal contacts. Almost same processes for alignment marks fabrication are employed. Since the lift-off process sometimes fails due to that too thick metal can not be removed with resist, metals of Cr = 2 nm and Ar = 40 nm are deposited for electrodes. During the lift-off process, ultrasonic cleaning must be avoid to prevent peeling off of graphene flakes.

Etching into nanostructures

The final step is the etching process, or this step can be before metal contact fabrication process as mentioned above. A resist for high resolution patterning, PMMA or hydrogen silsesquioxane (HSQ), is coated on the chip, followed by EBL and development. After that, inductive coupled plasma-reactive ion etching (ICP-RIE) is performed with O_2/Ar (1:8) plasma for ∼5 sec/layer. Then, the chip is cleaned by acetone for 15 mins, followed by IPA and DIW cleaning.

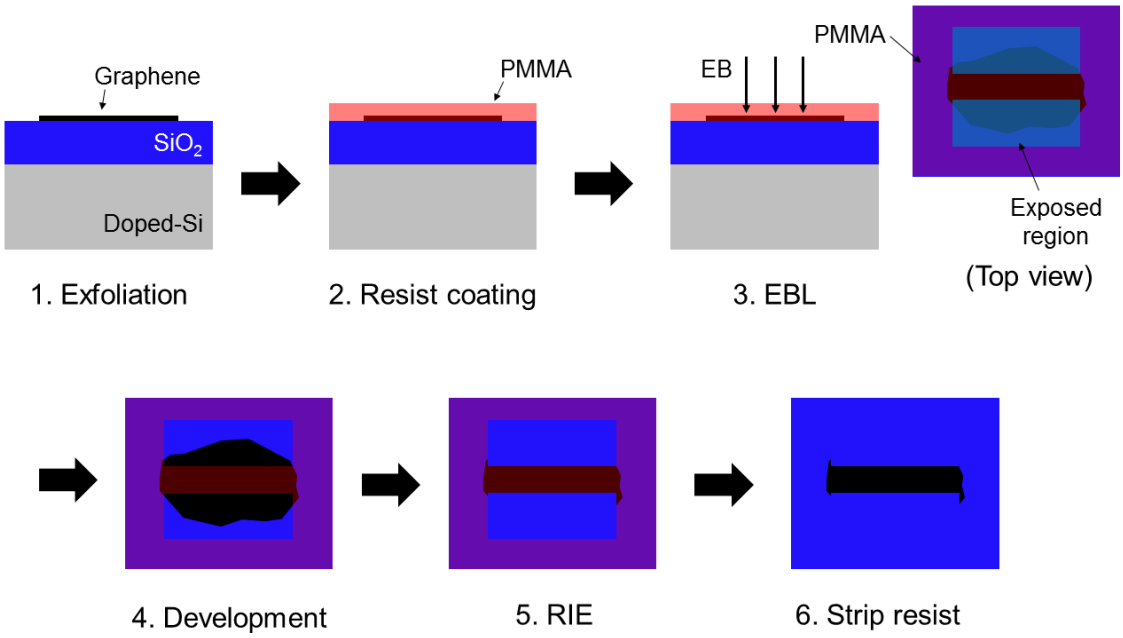

Figure 3.2: Fabrication process flow for etching using a PMMA resist.

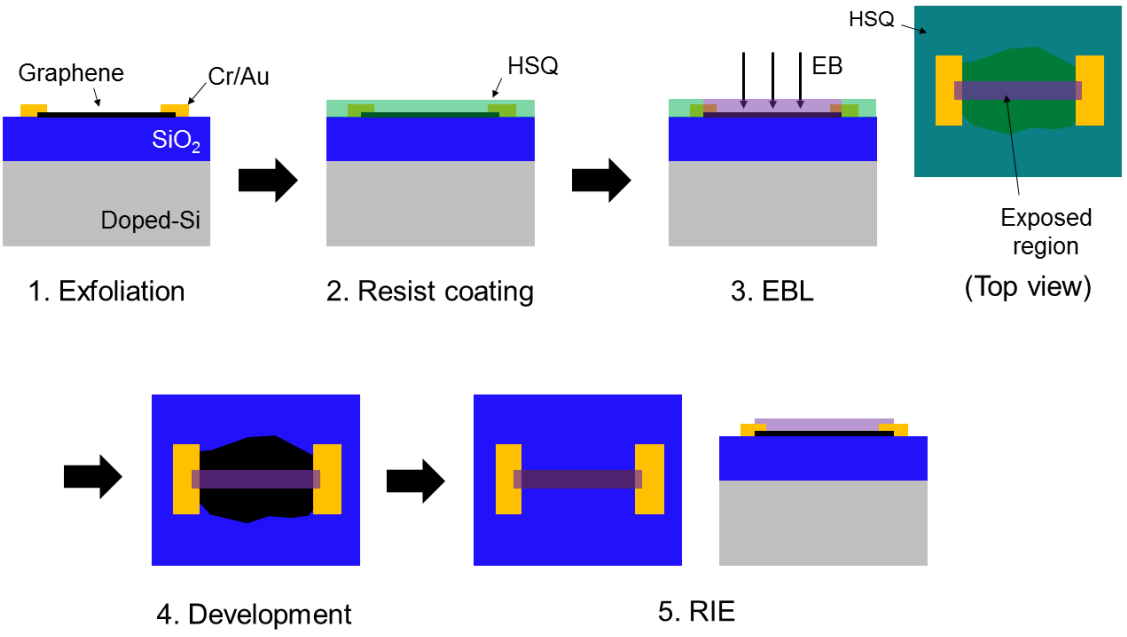

Figure 3.3: Fabrication process flow for etching using a HSQ resist. After RIE, the HSQ still remains on the top of graphene, which acts as a passivation layer.

3.2 Measurement of transport property

For measurements of transport property of graphene devices, two probe direct current (DC) measurement setup using a device analyzer (B1500A, Keysight Technologies, Inc., USA or 4200SCS, Keithley Instruments, Inc., USA) is used. While the measurements, the sample is measured under the vacuum condition of less than 10^{-3} Pa in a prober system (GRAIL 10-308-6-4K-LV-2RF-LLR (custom made), Nagase Techno-Engineering Co., LTD. Japan) that can control temperature in the sample chamber from 5 K to 300 K.

References

1) P. Blake, E. W. Hill, A. H. Castro Neto, K. S. Novoselov, D. Jiang, R. Yang, T. J. Booth, A. K. Geim, Making graphene visible. *Appl. Phys. Lett.* **91**, 063124 (2007).

2) K. S. Novoselov, A. K. Geim, S. V. Morozov, D. Jiang, Y. Zhang, S. V. Dubonos, I. V. Grigorieva, A. A. Firsov, Electric field effect in atomically thin carbon films. *Science* **306**, 666 (2004).

3) A. C. Ferrari, D. M. Basko, Raman spectroscopy as a versatile tool for studying the properties of graphene, *Nat. Nanotech.* **8**, 235 (2013).

4) A. C. Ferrari, J. C. Meyer, V. Scardaci, C. Casiraghi, M. Lazzeri, F. Mauri, Piscanec, D. Jiang, K. S. Novoselov, S. Roth, A. K. Geim, Raman spectrum of graphene and graphene layers, *Phys. Rev. Lett.* **97**, 187401 (2006).

5) T. Enoki *et al.*, グラフェンが拓く材料の新領域, NTS (2012).

Chapter 4

Design optimization for graphene quantum dot formation

In this chapter, the device design and the transport measurements on the geometrically-defined graphene quantum dot is presented. Additionally, the transport measurements and the novel patterning technique on the graphene nanoribbon (GNR) devices is shown.

4.1 Geometrical-defined graphene quantum dots

Here the graphene devices with geometrically-defined QDs are studied. Recently, single carrier transport properties in graphene have been studied by operating graphene-based SET devices at very low temperatures.[1–11] These devices have the graphene channel comprised of the SQD (or QDs), the narrow constrictions, and the side gates, which were fabricated by the conventional EBL and plasma etching processes. The constrictions connect the SQD to the source/drain regions, and define the tunnel barriers. As the conducting carriers can be switched between electrons and holes via gate voltage, thanks to the unique ambipolar behavior of graphene, the devices for the present study hereafter called as graphene single-carrier transistors (SCTs).

Designing the SCT structural parameters properly is undoubtedly crucial for observing single-electron tunneling characteristics. In particular, the constriction dimensions determine the tunnel resistance and capacitance. However, potential inhomogeneities, defects, and edge-disorder in the etched graphene channel cause the formation of carrier puddles which act as unintentional QDs.[12] Hence, observing the single carrier transport is difficult in such devices without potential tuning by application of side

gate voltage. However, the potential tuning also becomes difficult and complicated when the numbers of QDs are increased.[11]

It is imperative to eliminate such obstructive carrier puddles without the side gates tuning as possible, for controlling the single carrier transport in the well-defined graphene QD system. However, the methodology of suppressing such spurious QDs formation, and hence improving their transport properties, has not been established experimentally.

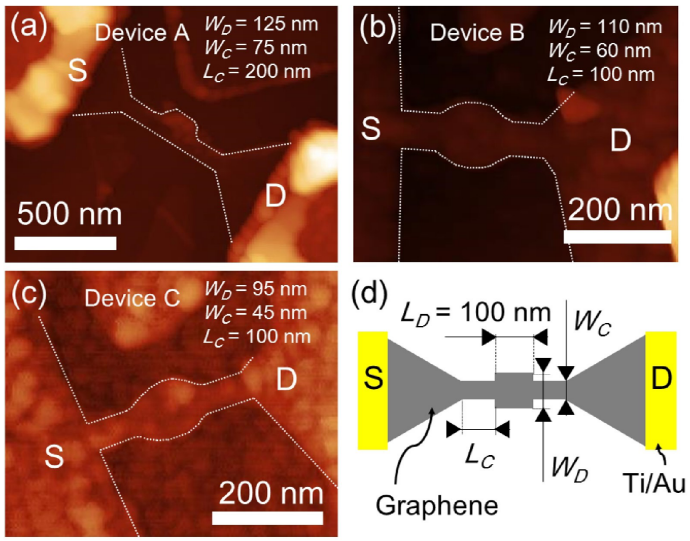

Figure 4.1: (a-c) AFM images of the fabricated devices and (d) the schematic of the graphene SCT design dimension. In AFM images of Devices (a) A, (b) B, and (c) C, white dot lines represent edges of the graphene channel, and S and D mean the source and drain electrodes. (d) schematically shows the device dimensions for Devices B and C. L_D is the dot length (100 nm). L_C is the constriction length, and W_D and W_C are the width of dot and constrictions, respectively.

In this chapter, we present a new engineering approach to avoid the uncontrolled formation of carrier puddles in SCTs by scaling down the channel constriction regions. Even though the SCT with the wider and longer channel constrictions showed Coulomb blockage, its Coulomb diamond characteristics were not fully lifted. This is the result of the multiple QDs formation in the graphene channel. Finally, it was found that the influences of the uncontrolled carrier puddle formation could be overcome in the SCT with narrow channel constrictions.

4.1.1 Design of device structure

The graphene SCT devices in this chapter were fabricated by the process described in Chapter 4. The n-doped Si substrate with SiO_2 of 300 nm

was used. The number of graphene layers was determined by Raman spectroscopy.[13,14]

The atomic force microscope (AFM) images of the fabricated SCTs with their designed structural parameters are shown in Fig. 4.1. Three graphene SCTs were fabricated Hereafter, we focus on three devices with the various sizes of QD and constrictions. Device A as shown in Fig. 4.1(a), which consists of monolayer graphene and has the widest structure (dot width $W_{\mathrm{D}} = 125$ nm, constriction width $W_{\mathrm{C}} = 75$ nm, constriction length $L_{\mathrm{C}} = 200$ nm), Device B as in Fig. 4.1(b) ($W_{\mathrm{D}} = 110$ nm, $W_{\mathrm{C}} = 60$ nm, $L_{\mathrm{C}} = 100$ nm), and Device C as in Fig. 4.1(c) ($W_{\mathrm{D}} = 95$ nm, $W_{\mathrm{C}} = 45$ nm, $L_{\mathrm{C}} = 100$ nm), which are bilayer graphene SCTs. Electrical current measurement was carried out using a three-terminal source, drain, and back-gate in the He cryostat at 1.7 K. Initially, graphene SCTs were measured at room temperature, and then the temperature was decreased to 1.7 K.

4.1.2 Transport property in graphene quantum dots

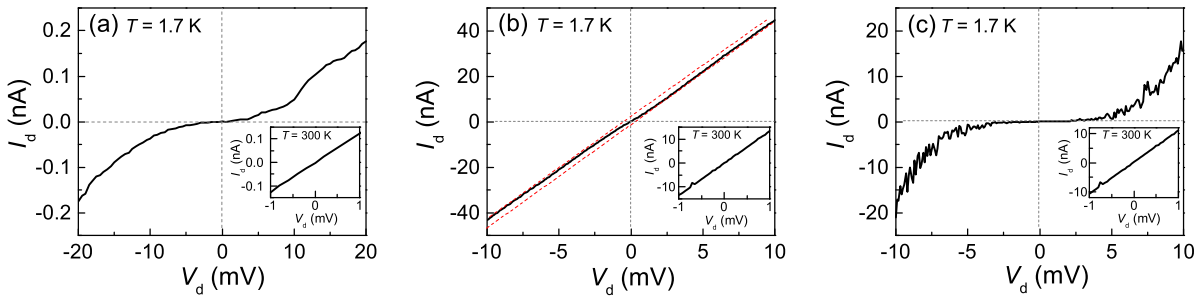

Figure 4.2: Source-drain characteristics of Devices (a) A, (b) B, and (c) C, respectively, at 1.7 K. Insets in all of the plots are I_{d}-V_{d} characteristics at room temperature for each device. The red dot lines in (b) represent the linear fitting lines to the positive and negative V_{d} voltage to indicate non-linearity.

Figure 4.2 shows the drain current-drain voltage (I_{d}-V_{d}) characteristics for Devices A, B, and C measured at 1.7 K. The individual insets show those at room temperature. As shown in Fig. 4.2(a), Device A showed nonlinearity over the wide V_{d} range at 1.7 K. This indicates a large source-drain Coulomb gap,[12] which is mainly attributed to the constrictions of 200 nm in length. We estimated the resistance value at room temperature, R_A is ~ 8.03 MΩ from the inset plot to Fig. 4.2. Device B exhibits weak non-linearity around $V_{\mathrm{d}} = 0$ V, as shown in Fig. 4.2(b), which signifies a small

Coulomb blockade effect. The estimated resistance of Device B at room temperature, $R_B \sim 74.2$ kΩ, which is remarkably smaller than R_A. The smaller resistance for Device B is primarily due to the shorter constrictions, and presumably also helped by a smaller contact resistance between the metal contact and graphene. It is not easy to evaluate the latter influence accurately, since the mechanical exfoliation process results in randomly shaped graphene flakes. On the other hand, the Device C's characteristics in Fig. 4.2(c) show strong nonlinearity for -5 mV $< V_{\mathrm{d}} < 5$ mV. The resistance of Device C at room temperature is extracted to be $R_C \sim 91.6$ kΩ, which is larger than R_B, in agreement with the narrower width in the channel. There is a clear difference between the results for Devices B and C, even though both have the same length of constrictions. This shows the importance of the narrower channel constrictions width to observe clear Coulomb blockade characteristics.

Secondly, the back-gate modulation characteristics were compared for Devices A, B and C. From the back-gate characteristics measured at room temperature, as shown in Fig. 4.3 (a), it was confirmed that Devices A, B and C were all p-doped with the charge neutrality point identified at around 15 V for Device B and over 40 V for Devices A and C. This p-doping is predominantly due to the graphene surface contamination (such as organic solvents, PMMA) caused during the device fabrication processes, and also to oxygen and ambient moisture physisorbed while the devices were prepared for low temperature measurements.[15–18] Figure 4.3 (b) shows the Coulomb oscillation characteristic measured for Device A at 1.7 K over the back gate voltage (V_{g}) from -5 to 5 V with various values of V_{d}. Within a small region indicated using a dashed oval, few growing conductance peaks were identified with increasing V_{d} along with the overall increase in the background current. Such a characteristic is attributable to the existence of many strongly coupled carrier puddles formed in the wide and long channel constrictions of Device A.[19] As the Fermi level is raised, the dimensions of the multiple carrier puddles and their in-between coupling are increased, resulting in the higher background current. Next, the Coulomb oscillation characteristic observed for Device B is shown in Fig. 4.3(c). As described earlier, the channel constriction dimensions of Device B are designed smaller than those for Device A. In contrast to Device A, a number of clear Coulomb oscillation peaks were observed steadily over the whole range of V_{d}. Finally, Fig. 4.3 (d) shows the Coulomb oscillation characteristic for Device C. The overall background current was found to

be remarkably reduced in comparison with Devices A and B. The highest peak-to-valley ratio of the drain current is approximately 10^3 at V_g ~24 V, as shown in the inset of Fig. 4.3(d). The valley currents remain very low even at higher V_d (see, for example, the valley current at V_g ~26 V). The peak voltages of the Coulomb oscillation show virtually no dependence on V_d. In parallel, we found the amplitude and width of those current peaks to be gradually increased a little. This implies the stable nature of the measured transport characteristics of the lithographically defined QD in the channel,[20] and no charge rearrangement in the swept V_g range.[2] Superimposition of the Coulomb oscillation characteristics on the ambipolar background current was seen for all Devices A, B and C.

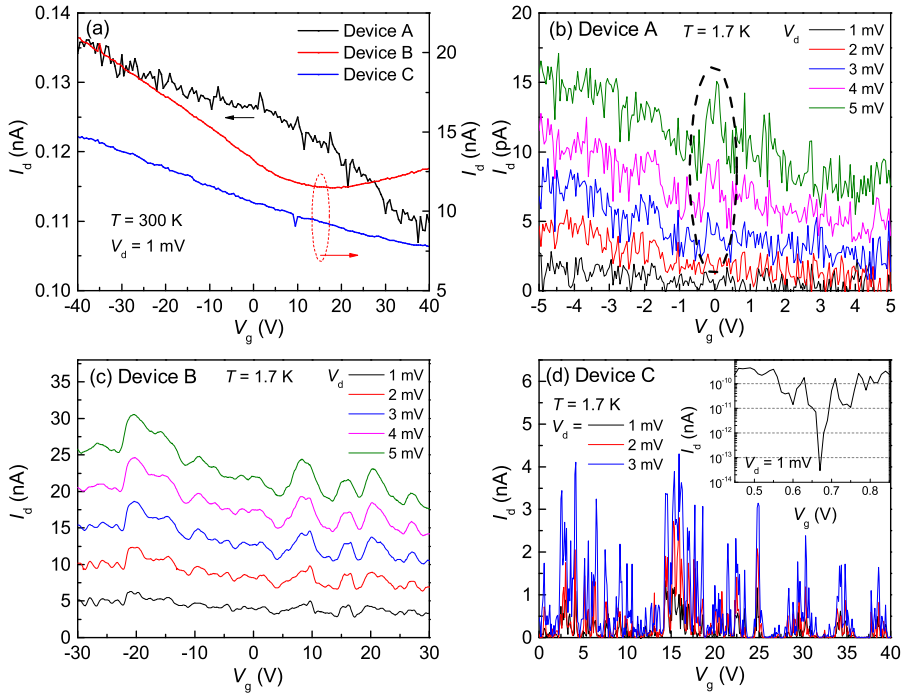

Figure 4.3: I_d-V_g ambipolar characteristics at 300 K for all of the devices. Black line corresponds to the result for Device A on the left axis. Red and blue lines are the results for Devices B and C, respectively, on the right axis. (b-d) I_d plot as a function of V_g for Devices (b) A, (c) B, and (d) C, respectively, at 1.7 K. Colored lines in (b), (c), and (d) represent the measurement results with various V_d values. Dashed circle in (b) emphasizes the stable Coulomb oscillation peaks at various V_d.

The Coulomb diamonds observed at 1.7 K for Devices A, B and C are presented in Fig. 4.4. For a clearly defined single QD device, a Coulomb blockade should be fully lifted periodically (*i.e.*, the individual Coulomb diamonds should be separated clearly from one another). The pattern observed for Device A, as shown in Fig. 4.4 (a), exhibits no blockade lifting, which may result from the presence of strongly coupled random multiple

QDs induced by the carrier puddles in the graphene channel. As the length of channel constrictions is 200 nm (twice as long as that for Devices B and C), it is likely that more QDs were formed due to the edge-disorder-induced carrier puddles in the constriction regions. This would require a higher bias voltage to transport the carrier across the source and drain electrodes. Furthermore, these carrier puddles might be connected naturally in series, which leads to no Coulomb blockade lift-off.[20,21] Such characteristics are often reported for the graphene nanoribbons[12] and heavily-doped silicon single electron devices.[22] For Device B, the Coulomb diamond characteristic was observed as shown in Fig. 4.4(b). The co-existence of bigger outer and smaller inner Coulomb diamonds is shown by yellow and white lines, respectively. This can be ascribed to the presence of well-coupled small and large QDs in the channel.[12] The small QD may be defined by the carrier puddles induced in the channel constriction regions, and the larger QD might be the one defined lithographically. This device characteristic clearly signifies that the Coulomb blockade is lifted off completely, in contrast to Device A, thanks to the narrower constrictions designed for Device B. However, the difference between the Coulomb blockade and conductance regions is not apparent due to the high background current. Figure 4.4(c) shows the Coulomb diamond characteristics for Device C, which features the narrowest channel constrictions of 45 nm.

The detail of the Coulomb diamond patterns for the V_g range from 20 to 30 V (demarked by the dot lines in Fig. 4.4(c)) is shown in Fig. 4.4(d). It should be noted that the Coulomb blockade regions and conductance regions are separated clearly. Compared with the Coulomb diamond characteristics for Devices A and B, Coulomb blockade is clearly lifted with Device C. The intrinsic disorder length associated with the carrier puddles formation in graphene is reported to be around 30 nm from the scanning tunneling microscope experiments.[24] It is likely that the formation of the unwanted carrier puddles is avoided when the characteristic dimension of the narrowest channel region lies within this intrinsic disorder length. At the same time, the energy band gap could be retained, which is important to form the tunnel barriers. Among three device designs used for the present study, Device C with constrictions of about 45 nm in width is the closest to this criterion, therefore, the formation of unwanted carrier puddles is avoided while retaining the tunnel barrier. These results manifest that it is crucial to design the channel constriction width properly in order to realize graphene SCTs with well-controlled Coulomb blockade

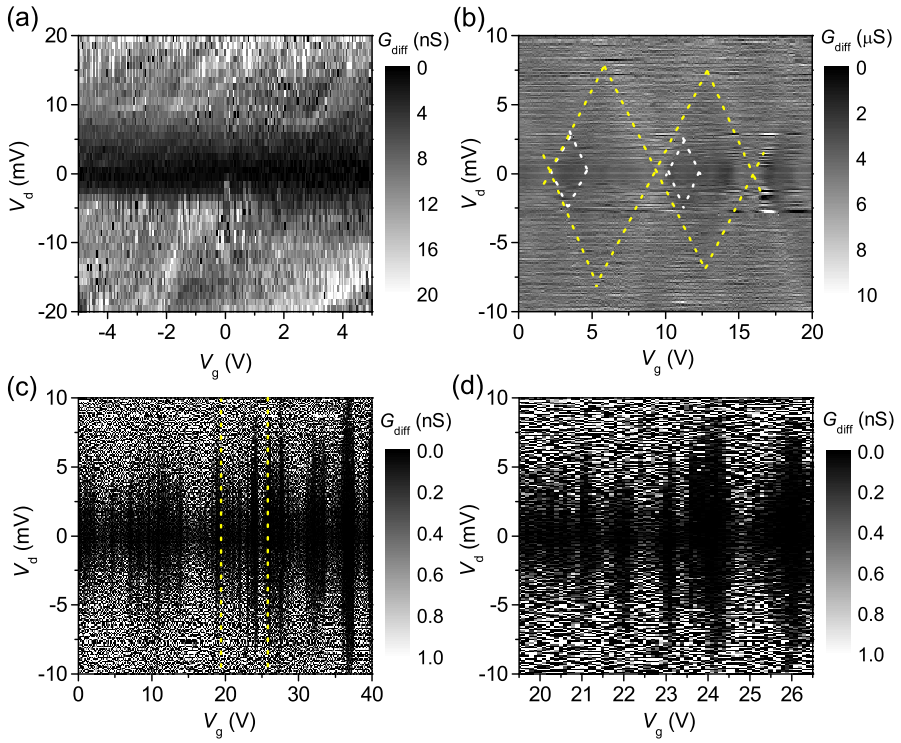

Figure 4.4: Differential conductance (G_{diff}) gray-scale plot as a function of V_{d} and V_{g} for Devices (a) A, (b) B, and (c) C, respectively, at 1.7 K. Dark area corresponds to the low conductance regions. The yellow dot lines in (b) indicate the edge of bigger Coulomb diamond regions, and the white dot lines represent the smaller Coulomb diamond regions. (d) shows the zoom-up plot for Device C, which is marked by the yellow dot lines in (c).

properties.

4.1.3 Summary

In summary, we have fabricated and characterized three graphene SCTs with various dimensions of channel constrictions. From the comparison of Coulomb diamond characteristics for these devices, the narrower constriction device demonstrated strong suppression of the background conductance and observation of a clear Coulomb blockade and fully-lifted diamond characteristics in graphene SCTs. This is attributed to the narrower constriction, which might be near/below the typical intrinsic disorder dimension of the graphene for the multiple carrier puddle formation.

References

1) L. A. Ponomarenko, F. Schedin, M. I. Katsnelson, R. Yang, E. W. Hill, K. S. Novoselov, A. K. Geim, Chaotic Dirac billiard in graphene quantum dots. *Science* **320**, 356 (2008).

2) C. Stampfer, J. Güttinger, F. Molitor, D. Graf, T. Ihn, K. Ensslin, Tunable Coulomb blockade in nanostructured graphene. *Appl. Phys. Lett.* **92**, 012102, (2008).

3) C. Stampfer, E. Schurtenberger, F. Molitor, J. Güttinger, T. Ihn, K. Ensslin, Tunable Graphene single electron transistor. *Nano Lett.* **8**, 2378 (2008).

4) J. Güttinger, T. Frey, C. Stampfer, T. Ihn, K. Ensslin, Spin states in graphene quantum dots. *Phys. Rev. Lett.* **105**, 116801 (2010).

5) F. Molitor, S. Dröscher, J. Güttinger, A. Jacobsen, C. Stampfer, T. Ihn, K. Ensslin, Transport through graphene double dots. *Appl. Phys. Lett.* **94**, 222107 (2009).

6) L. J. Wang, H. O. Li, T. Tu, G. Cao, C. Zhou, X. J. Hao, Z. Su, M. Xiao, G. C. Guo, A. M. Chang, G. P. Guo, Controllable tunnel coupling and molecular states in a graphene double quantum dot. *Appl. Phys. Lett.* **100**, 022106 (2012).

7) L. J. Wang, G. P. Guo, D. Wei, G. Cao, T. Tu, M. Xiao, G. C. Guo, A. M. Chang, Gates controlled parallel-coupled double quantum dot on both single layer and bilayer graphene. *Appl. Phys. Lett.* **99**, 112117 (2011).

8) S. Fringes, C. Volk, C. Norda, B. Terrés, J. Dauber, S. Engels, S. Trellenkamp, C. Stampfer, Charge detection in a bilayer graphene quantum dot. *Phys. Status Solidi B* **248**, 2684 (2011).

9) S. Dröscher, J. Güttinger, T. Mathis, B. Batlogg, T. Ihn, K. Ensslin, High-frequency gate manipulation of a bilayer graphene quantum dot. *Appl. Phys. Lett.* **101**, 043107 (2012).

10) C.Volk, S. Fringes, B. Terrrés, J. Dauber, S. Engels, S. Trellenkamp, C. Stampfer, Electronic excited states in bilayer graphene double quantum dots. *Nano Lett.* **11**, 3581 (2011).

11) D. Wei, H. O. Li, G. Cao, G. Luo, Z. X. Zheng, T. Tu, M. Xiao, G. C. Guo, H. W. Jiang, G. P. Guo, Tuning inter-dot tunnel coupling of an etched graphene double quantum dot by adjacent metal gates. *Sci. Rep.* **3**, 3175 (2013).

12) P. Gallagher, K. Todd, D. Goldhaber-Gordon, Disorder-induced gap behavior in graphene nanoribbons. *Phys. Rev. B* **81**, 115409 (2010).

13) A. C. Ferrari, J. C. Meyer, V. Scardaci, C. Casiraghi, M. Lazzeri, F. Mauri, S. Piscanec, D. Jiang, K. S. Novoselov, S. Roth, A. K. Geim, Raman spectrum of graphene and graphene layers. *Phys. Rev. Lett.* **97**, 187401 (2006).

14) D. Graf, F. Molitor, K. Ensslin, C. Stampfer, A. Jungen, C. Hierold, L. Wirtz, Spatially resolved Raman spectroscopy of single- and few-layer graphene. *Nano Lett.* **7**, 238 (2007).

15) A. Pirkle, J. Chan, A. Venugopal, D. Hinojos, C. W. Magnuson, S. McDonnell, L. Colombo, E. M. Vogel, R. S. Ruoff, R. M. Wallace, The effect of chemical residues on the physical and electrical properties of chemical vapor deposited graphene transferred to SiO_2. *Appl. Phys. Lett.* **99**, 122108 (2011).

16) F. Schedin, A. K. Geim, S. V. Morozov, E. W. Hill, P. Blake, M. I. Katsnelson, K. S. Novoselov, Detection of individual gas molecules adsorbed on graphene. *Nat. Mater.* **6**, 652 (2007).

17) S. Ryu, L. Liu, S. Berciaud, Y. J. Yu, H. Liu, P. Kim, G. W. Flynn, L. E. Brus, Atmospheric oxygen binding and hole doping in deformed graphene on a SiO_2 substrate. *Nano Lett.* **10**, 4944 (2010).

18) O. Leenaerts, B. Partoens, F. M. Peeters, Adsorption of H_2O, NH_3, CO, NO_2, and NO on graphene: A first-principles study. *Phys. Rev. B* **77**, 125416 (2008).

19) J. Xue, J. S. Yamagishi, D. Bulmash, P. Jacquod, A. Deshpande, K. Watanabe, T. Taniguchi, P. J. Herrero, B. J. LeRoy, Scanning tunnelling microscopy and spectroscopy of ultra-flat graphene on hexagonal boron nitride. *Nat. Mater.* **10**, 282 (2011).

20) M. Manoharan, Y. Kawata, Y. Tsuchiya, S. Oda, H. Mizuta, Strongly coupled multiple-dot characteristics in dual recess structured silicon channel. *J. Appl. Phys.* **103**, 043719 (2008).

21) W. G. van der Wiel, S. De Franceschi, J. M. Elzerman, T. Fujisawa, S. Tarucha, L. P. Kouwenhoven, Electron transport through double quantum dots. *Rev. Mod. Phys.* **75**, 1 (2002).

22) R. Augke, W. Eberhardt, C. Single, F. E. Prins, D. A. Wharam, D. P. Kern, Doped silicon single electron transistors with single island characteristics. *Appl. Phys. Lett.* **76**, 2065 (2000).

23) M. Manoharan, S. Oda, H. Mizuta, Impact of channel constrictions on the formation of multiple tunnel junctions in heavily doped silicon single electron transistors. *Appl. Phys. Lett.* **93**, 112107 (2008).

24) J. Martin, N. Akerman, G. Ulbricht, T. Lohmann, J. H. Smet, K. Von Klitzing, A. Yacoby, Observation of electron-hole puddles in graphene using a scanning single-electron transistor. *Nat. Phys.* **4**, 144 (2008).

4.2 High aspect ratio graphene nanoribbons

In the graphene SET with the geometrically-defined QD, the transport characteristics manifested itself from multiple QDs, which could be formed in not only the dot region, but also constriction regions. From the previous experiments, it is clarified that the probability to form multiple QDs tends to be less when narrowing the constriction regions. Therefore, we approach the transport property with no QD formation in graphene by narrowing the width of GNR.

So far, GNR devices have been widely studied since narrowing the graphene width down to tens-of-nanometer is an effective way to open the band gap in graphene owing to quantum confinement.[1,2] Most of the reported GNRs were obtained by chemical approaches or special types of lithographic techniques,[3–6] which are not compatible with integrated circuit manufacturing technology and suffer from low yielding rate. Recently, plasma etching using hydrogen silsesquioxane (HSQ) resist as protective masks is utilized to narrow down the GNRs following the standard nanofabrication procedures. The dimension of the resulting GNR is essentially transferred from the mask. Thus, it heavily relies on the patterning of extremely narrowed down HSQ masks. So far, most of the works only showed relatively wide GNRs with the gap opening of 100 meV.[7–9] Here, we develop a simple method to fabricate ultra-narrow GNRs by introducing lateral etching effect in the regular plasma etching process. With the proposed method, the extremely narrowed down HSQ mask is not necessary. The dimensions of the resulting GNRs are not completely transferred from the 50-nm-wide capping masks, but showing the narrower widths due to the additional lateral etching. The high on/off current ratios of 10^5 and 47 are demonstrated in the GNR FET device at 5.4 K and room temperature, respectively. From the electrical measurement data, the transport gap opening of 145 meV and a nominal width of 5 nm are estimated for the resulting GNR.

4.2.1 High pressured lateral plasma etching

The fabrication process starts with the mechanically exfoliated monolayer graphene flakes on the p-doped silicon substrate covered with 300 nm thermal SiO_2. The metal contacts as source and drain for the FET structure are defined with Cr/Au (10/60 nm) electrodes via conventional fabrication

processes. Ohmic contacts between metal and graphene are verified from linear current-voltage response. The absorbates and organic residues on graphene flakes from the previous fabrication process are removed by using current annealing. Afterward, HSQ resist (XR-1541-002, Dow Corning) is spun onto the samples. Low spin rate of 3000 rpm is used to avoid any rolling or damage of graphene during coating, which results in the thickness of 40 nm. Then, electron-beam lithography (EBL) is employed to pattern HSQ into the desired shape as etching mask for graphene at a low dose of 1 mC/cm^2 (Fig. 1(a)). In this work, we use the HSQ stripes of 50 nm wide, which can be easily achieved with most of the EBL systems. No post-baking is performed afterwards. In the end, the sample is transferred into a reactive ion etcher. We etch graphene by using O_2 plasma with a high power of 75 W and at a high pressure of 26.5 Pa, in contrast to these commonly used parameters, *i.e.*, 40 W and 5 Pa. After the fabrication, the GNRs are characterized as FET devices, where p-doped Si substrate acts as back-gate. The electrical measurements are performed in vacuum (5 Pa) with temperatures varying from 5.4 to 300 K.

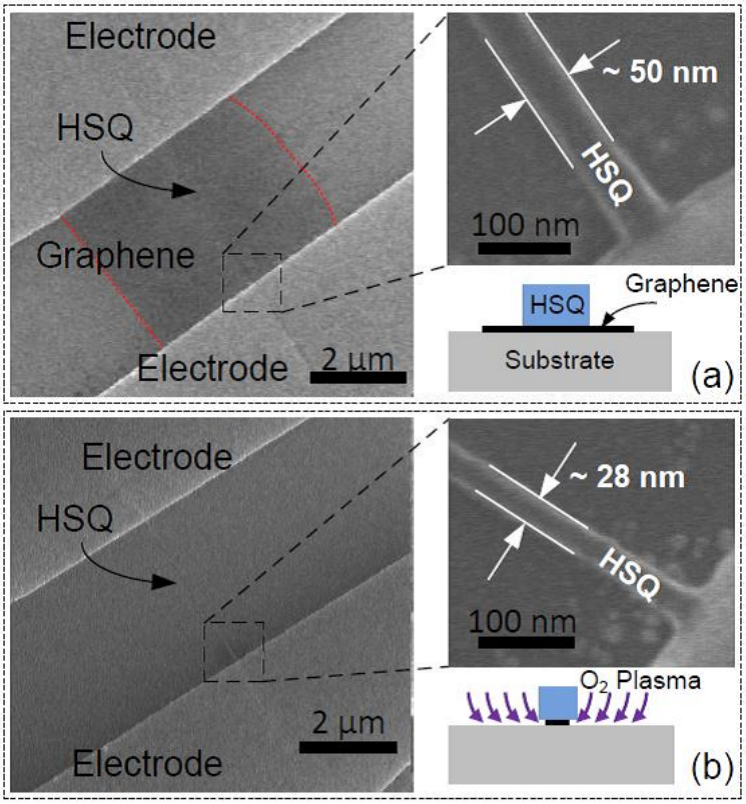

Figure 4.5: SEM images and cross-section sketches of a FET (a) before and (b) after graphene patterning with oxygen plasma etching (70 W, 26.5 Pa), respectively. Red dot-lines in (a) indicate the edges of the graphene flake.

Figure 1 illustrates a graphene FET device before and after the plasma etching. The graphene channel is 3.5 μm long. Before etching, HSQ shows a width of 50 nm as designed. The process with high power of 75 W etches HSQ mildly by physical bombardment. Moreover, owing to high process pressure of 26.5 Pa, the lateral etching effect is induced. As a consequence, after a 50 s plasma etching, a narrower HSQ masks of 28 nm is noted (Fig. 1(b)), echoing the lateral etching effect. Meanwhile, the induced lateral etching also trims down the GNR from its edges (shown as the cartoon in Fig. 1(b)). Known that oxygen plasma has a higher etch rate on graphene, thereby, resulting in a lower width in GNR than the capping HSQ. First, we characterize a fabricated GNR FET. The bandgap opening and width of the resulting GNR are also extracted through the electrical measurement data. Figure 2(a) shows the conductance versus the back-gate voltage V_{g} at different temperatures. The on/off ratio of current is 47 at 300 K and increases to 10^5 at 5.4 K. The strong temperature with strongly suppressed conductance. We can now extract the transport gap ΔE_{g} corresponding to ΔV_{g} by using

$$\Delta E_{\mathrm{g}} = \hbar v_{\mathrm{F}} \sqrt{2\pi C_{\mathrm{g}} \Delta V_{\mathrm{g}} / |e|} \tag{4.1}$$

where $v_{\mathrm{F}} = 10^6$ m/s is the Fermi velocity of graphene and C_{g} is the back-gate capacitance per area.[7] The value of transport gap is calculated as 145±7 meV. Note, at the low dose applied to HSQ, the contribution of the weak hydrogenation from the dissociated HSQ is negligible.[11] Thus, the nominal width of the resulting GNR (W) is 4.6±3 nm estimated via $\mathrm{W} \sim \hbar v_{\mathrm{F}} / \Delta E_{\mathrm{g}}$,[7] thereby leading to the high aspect ratio GNR channel of 800.

Figure 2(b) shows the I_{d}-V_{d} characteristic measurements at various temperatures. The nonlinear response is considered as another evidence of the opening energy gap. The energy gap of 400 meV is obtained by using $\mathrm{e}\Delta V_{\mathrm{d}}$, where ΔV_{d} is the measured nonlinear gap.[10] The difference from the previous estimation is attributed to the presence of Coulomb blockade as the result of the edge disorder and its localized states.[7,12]

In order to understand and highlight the impact of lateral etching to the enhancement of device performance, we first conduct a mild 30-s-long etching to another graphene FET (channel length: 500 nm and HSQ width: 50 nm) at lower power (45 W), which is enough to remove the undesired graphene completely but does not induce heavy lateral etching to the GNR. The gate modulation characteristic measured at 5.4 K exhibits an on/off

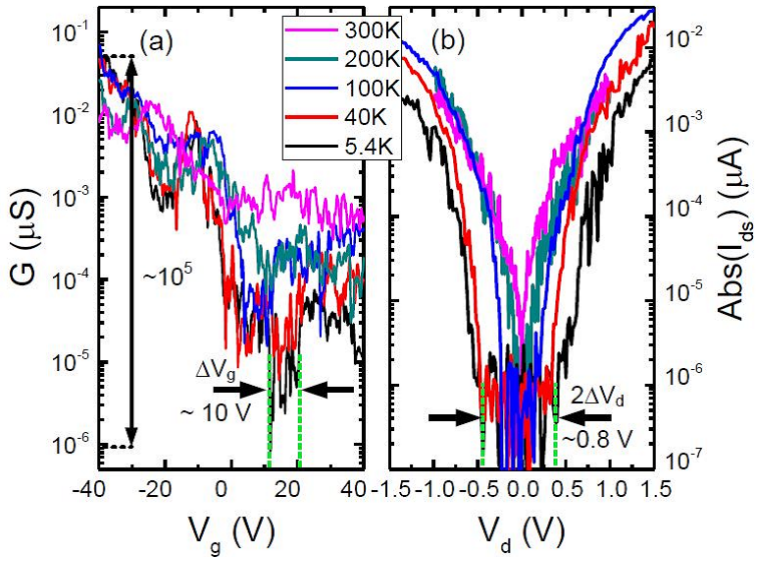

Figure 4.6: (a) Conductance of GNR G as a function of back-gate voltage $V_{\rm g}$ ($V_{\rm d} = 0.75$ V) and (b) drain current (absolute value) as a function of $V_{\rm d}$ ($V_{\rm g} = 0$ V) at various temperatures. The arrows and green dash-line in (a) and (b) indicate the measured transport gap $V_{\rm g}$ and nonlinear gap $V_{\rm d}$, respectively.

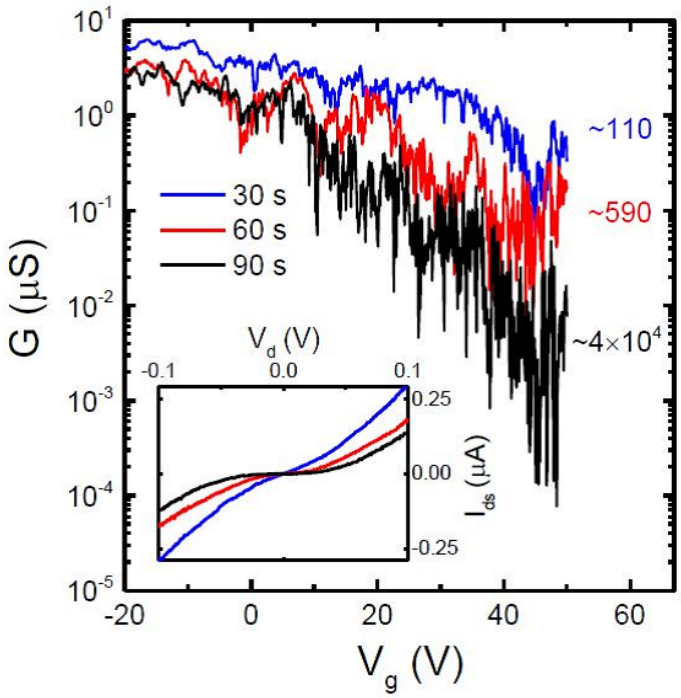

Figure 4.7: (a)Back-gate characteristics of the GNR FET measured at 5.4 K after etching step of 30 second. The legend gives the value of the total etched duration. The numbers on the right side are the on/off current ratio estimated from the curves correspondingly. Inset: $I_{\rm d}$-$V_{\rm d}$ characteristics measured after etching steps at 5.4 K ($V_{\rm g} = 45$ V).

ratio of 110 (Fig. 3). Then, another two 30-s-long etching steps are preformed sequentially. With the increasing etching duration, namely, the heavier lateral etching, the minimum conductance of GNR is reduced by 3 orders of magnitude, and its on/off current ratio is dramatically improved to $\sim 4 \times 10^4$. Additionally, the hole mobilities of the GNR are also estimated after each etching steps by using the model introduced in Ref.[13]. They are extracted as 100 $\mathrm{cm^2/Vs}$, 60 $\mathrm{cm^2V^{-1}s^{-1}}$, and 20 $\mathrm{cm^2V^{-1}s^{-1}}$, respectively, which are similar to those previously reported results.[14] In the I_d-V_d characteristics, the gradually enhanced nonlinearity and ΔV_g gap is also noticed with lengthened etching. They all reveal the trimmed-down width and band-gap opening of GNR in virtue of the lateral etching. In the end, the ΔV_g of 5 V is measured, suggesting the transport energy gap of 100 meV and the width of 6.6 nm. The remaining HSQ mask is 38 nm wide. Furthermore, we notice a good consistency of the etching duration, which is required to open the transport gap corresponding to a ΔV_g of 5 V, in six samples prepared in two different batches. It suggests the stability and controllability of the proposed process.

4.2.2 Transport property of graphene nanoribbons

In addition, a FET device is fabricated with intentionally introduced quantum-dot geometries in the capping HSQ mask (50-nm-wide and 500-nm-long stripe with several dots). A 20 s short plasma etching is conducted with the power of 45 W. Then, the Coulomb diamond characteristic is measured at 5.4 K, which acts as a direct hint of the GNR geometry. The overlapped Coulomb diamond-like shapes with clear outer boundaries are identified (Fig. 4(a)), corresponding to the geometry of several quantum dots in series.[12] Thus, the geometry of the shortly etched GNR is basically transferred from the capping HSQ mask. However, as the etching duration increhighly merged Coulomb diamond-like shapes with barely distinguished boundaries as a stripe (Fig. 4(b)), which indicates a large number of small quantum dots with similar diameters are formed in the GNR as a result of the defective edges. The widths of these merged diamonds (stripe-like shape) are almost uniform. It reveals the back gate voltage independent opening band-gap, in other words, the uniform width formed along the GNR. Owing to the strong lateral etching, the geometry of the resulting GNR is not directly transferred from the HSQ mask. In fact, the lateral etching reshapes the edges of the GNR, giving rise to a different

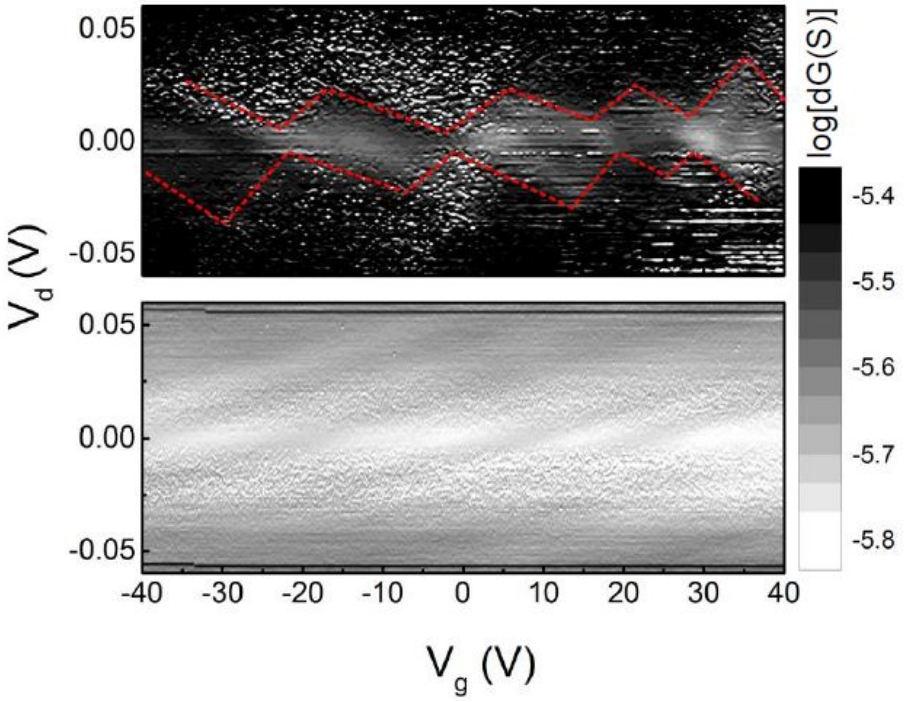

Figure 4.8: Coulomb diamond characteristics of a GNR capped with HSQ mask with intentionally introduced quantum-dot geometries after (a) 20 seconds and (b) 50 seconds plasma etching of 45 W at 5.4 K. The red dash-lines in (a) are provided as a guidance of the outer edges of the overlapped Coulomb diamonds.

geometry from that of the capping HSQ mask.

4.2.3 Summary

In this work, we report that the enhanced on/off ratio of GNR FET is achieved simply by narrowing down GNR to sub-10-nm via lateral plasma etching. The large on/off ratios of 47 and 10^5 are obtained at room temperature and 5.4 K, respectively, in the GNR with a transport gap opening of 145 meV. Moreover, thanks to the passivation of HSQ, the GNR FETs are robust, albeit with high aspect ratio and at large gate voltage. Additionally, desired width of GNR channel could be expected via optimizing the etching conditions. We deem that the lateral etching technique has the potential to realize the GNR FETs of high on/off ratio in wafer-scale with the combination of the state-of-the-art photo-lithographic technology.

However, the GNR structure, especially long length, showed that the characteristics of multiple quantum dots appear even if the constriction are made narrower than the critical size of localized carrier puddle. It is conceivable that the edge disorder is greatly effective and geometric

quantum dots are unintentionally formed. Intuitively, the possibility of the pseudo QDs formation is high as the GNR length is longer. Hence, a shorter constriction structure might be suitable for forming a SQD. This will be discussed again in Chapter 6.

References

1) K. Nakada, M. Fujita, G. Dresselhaus, M. S. Dresselhaus, Edge state in graphene ribbons: Nanometer size effect and edge shape dependence. *Phys. Rev. B* **54**, 17954 (1996).

2) Y. W. Son, M. L. Cohen, S. G. Louie, Energy gaps in graphene nanoribbons. *Phys. Rev. Lett.* **97**, 216803 (2006).

3) X. Li, X. Wang, L. Zhang, S. Lee, H. Dai, Chemically derived, ultrasmooth graphene nanoribbon semiconductors. *Science* **319**, 1229 (2008).

4) G. Son, M. Son, K. J. Moon, B. H. Lee, J. M. Myoung, M. S. Strano, M. H. Ham, C. A. Ross, Sub-10 nm graphene nanoribbon array field-effect transistors fabricated by block copolymer lithography. *Adv. Mater.* **25**, 4723 (2013).

5) T. Kato, R. Hatakeyama, Site- and alignment-controlled growth of graphene nanoribbons from nickel nanobars. *Nat. Nanotech.* **7**, 651 (2012).

6) V. Abramova, A. S. Slesarev, J. M. Tour, Meniscus-mask lithography for narrow graphene nanoribbons. *ACS Nano* **7**, 6894 (2013).

7) M. Y. Han, J. C. Brant, P. Kim, Electron transport in disordered graphene nanoribbons. *Phys. Rev. Lett.* **104**, 056801 (2010).

8) Y. M. Lin, V. Perebeinos, Z. Chen, P. Avouris, Electrical observation of subband formation in graphene nanoribbons. *Phys. Rev. B* **78**, 161409 (2008).

9) W. S. Hwang, K. Tahy, X. Li, H. G. Xing, A. C. Seabaugh, C. Y. Sung, D. Jena, Transport properties of graphene nanoribbon transistors on chemical-vapor-deposition grown wafer-scale graphene. *Appl. Phys. Lett.* **100**, 203107 (2012).

10) M. Y. Han, B. Özyilmaz, Y. Zhang, P. Kim, Energy band-gap engineering of graphene nanoribbons. *Phys. Rev. Lett.* **98**, 206805 (2007).

11) J. Balakrishnan, G. K. W. Koon, M. Jaiswal, A. C. Neto, B. Özyilmaz, *Nat. Phys.* **9**, 284 (2013).

12) P. Gallagher, K. Todd, D. Goldhaber-Gordon, Disorder-induced gap behavior in graphene nanoribbons. *Phys. Rev. B* **81**, 115409 (2010).

13) S. Kim, J. Nah, I. Jo, D. Shahrjerdi, L. Colombo, Z. Yao, E. Tutuc, S. K. Banerjee, Realization of a high mobility dual-gated graphene field-effect transistor with Al_2O_3 dielectric. *Appl. Phys. Lett.* **94**, 062107 (2009).

14) Y. Yang, R. Murali, Impact of size effect on graphene nanoribbon transport. *IEEE Electron Dev. Lett.* **31**, 237 (2010).

Chapter 5

Doping effects in graphene

In this chapter, the doping effects in graphene are presented. Firstly, the spatial distribution of local doping is investigated. Then, the method to control the averaged doping in overall graphene is discussed.

5.1 Spatially localized doping concentration in graphene

Here, local doping in graphene induced by charged impurities is spatially resolved by using the TERS technique, a state-of-the-art technology combining AFM and Raman spectroscopy.

Because of its special mechanical, electronic, magnetic, photonic, optelectronic, thermal properties and *etc.*,[1,2] graphene has been expected for various device applications, such as gas sensors,[3] nanoelectromechanical systems,[4,5] and flexible thin film transistors.[6] It is known that electrical characteristics of graphene are influenced by defects,[7] strain,[8,9] and doping concentration modulation.[3,10–12] As those could be induced either intrinsically in the growth of graphene or extrinsically during the device fabrication process, a method to evaluate the quality of the graphene with high spatial resolution down to nanoscale must be very useful for detailed analysis of graphene nanoelectronic devices.

Raman spectroscopy has been extensively used as a non-destructive method to obtain various properties in graphene,[13] such as the number of layers (Fig. 5.1),[14] edge,[15] disorder,[16] defect,[7,17,18] strain,[19–24] and doping.[24–27] However, conventional Raman spectroscopy only gives the averaged signal over the microscale laser spot size and its spatial resolution is limited by laser diffraction. One of the high resolution scanning methods of analogizing graphene properties is by tip-enhanced Raman spectroscopy, which is the combination of near field tip scanning microscopy and Raman excita-

tion.

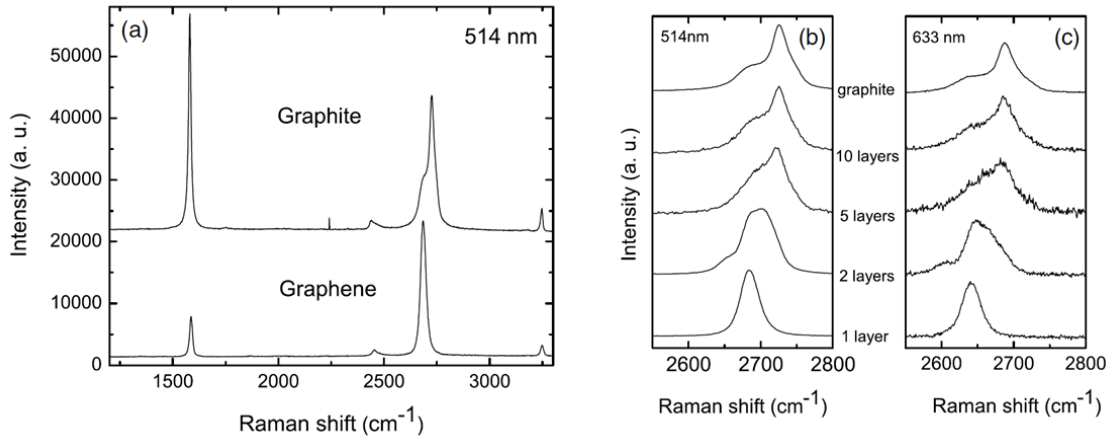

Figure 5.1: Identification of the number of graphene layers by Raman spectroscopy.[14] (a) Raman spectra of bulk graphite and graphene at 514 nm laser excitation. (b) Evolution of the Raman spectra with the number of layers at 514 nm and (b) at 633 nm laser excitation.

Scanning probe microscope (SPM), such as atomic force microscope (AFM), scanning tunneling microscope (STM), is capable of examining the specimen shape with a spatial resolution of the nanoscale. By combining this technology with Raman spectroscopy, tip-enhanced Raman spectroscopy (TERS) was proposed by Wessel in 1985[28] to obtain the Raman scattering signal in high spatial resolution. In 2000, three groups independently demonstrated tip-enhanced Raman scattering for the first time.[29–31] In this technique, Raman spectroscopy is performed simultaneously scanning a sample by SPM using a probe tip coated by metal (or made from metal), such as Au, that its plasmon resonance frequency is similar to the laser excitation wavelength. . The excitation light is irradiated onto the sample and aligned with the position of the top of probe tip, where an electric field of the light is enhanced by the lightning rod effect, surface plasmon resonance, and antenna resonance.[32] Then, the near-field effect results in the enhancement of Raman scattering intensity around the tip apex. The SPM feedback system is used to close the distance between the tip and sample for enabling the near-field effect. Consequently, TERS can pick up a Raman spectrum containing the information only around the tip apex.

So far, three types of TERS setups, back, side, and top illumination as shown in Fig. 5.2, have been used depending on the property of sample,

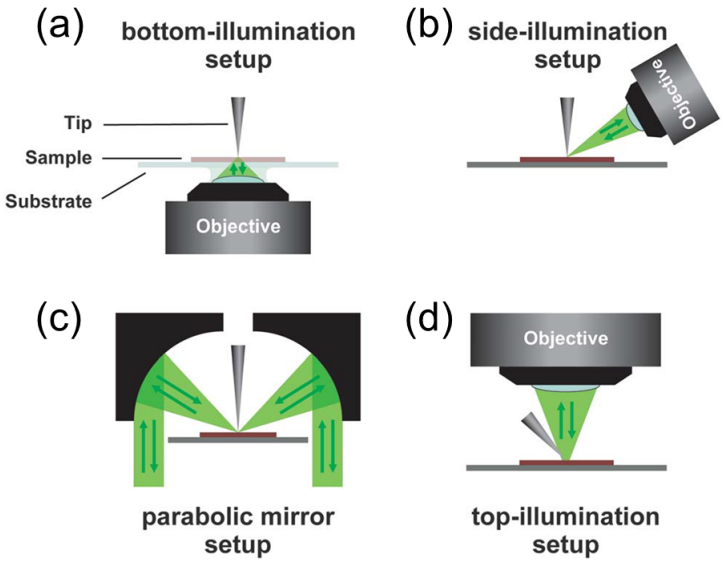

Figure 5.2: Schematic drawings of the different illumination configuration for TERS with (a) Back, (b) side, (c) top using a parabolic mirror, and (d) standard top illumination setups.[32]

in particular transparency with respect to an excitation light. The difference of each configuration is objective lens, which determines a numerical aperture (NA). According to the Rayleigh's criteria for spatial resolution;[33]

$$\delta = \frac{0.61 \times \lambda}{\mathrm{NA}} \tag{5.1}$$

where, δ is a spatial resolution and λ is a wavelength of light, therefore, the spatial resolution depends on the NA. Note that, an amount of collection of Raman scattering signal also depends on the NA.[32] In case of the back illumination, the objective lens with the high NA of 1.4∼1.6 can be employed because of a very short working distance. However, this setup requires the transparency of a sample and a substrate. The back illumination is therefore considered as a suitable method for biological samples. The side and top illuminations can be used for opaque samples and substrates. These setups require the objective lens with a long working distance because of the space for the SPM probe whereas that objective has only the low NA of 0.28∼0.7.[32] The laser spot in the side illumination setup is larger than that of top illumination setup due to the laser incident angle against a sample. In case of the top illumination setup, the main problem is the position of the tip and the laser spot. The parabolic mirror setup can overcome this issue, however, the setup would be very complicated.

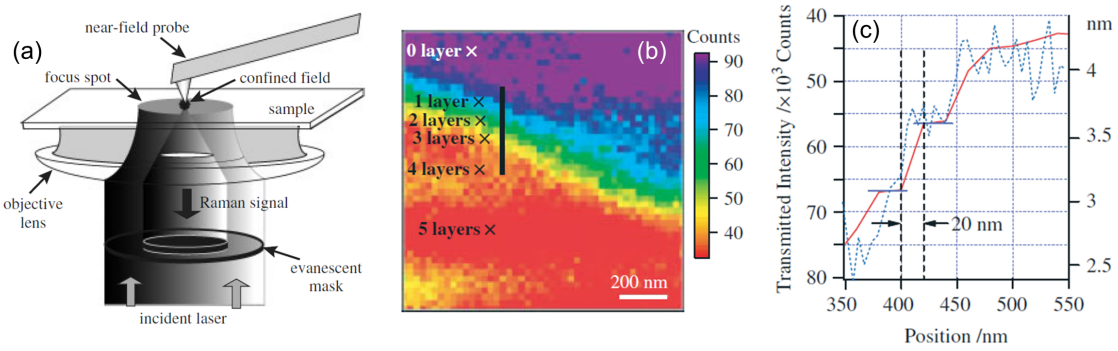

Figure 5.3: Edge boundary detection of graphene layers on a glase plate by TERS with the back illumination setup. (a) Schematic illustration of the experimental setup used in Ref.[35]. (b) TERS mapping of ultrathin graphene sample. Edge boundary and variation of layer thickness can be seen at high contrast. (c) Red line indicates the line profile of the Raman intensity along the line shown in (b) and blue dotted line indicates the AFM height information at the same place.

Since the first TERS measurement for graphene in 2008[34], TERS has been intensively used for investigating local material properties of various types of graphene, such as mechanically-exfoliated graphene on glass,[35–43], on Au,[44] chemical vapor deposition (CVD)-grown graphene on glass[43] or on Cu,[44] epitaxially-grown graphene on SiC,[45–47] and polymerized graphene.[48] For instance, the edge boundary detection was reported for the graphene flake on a transparent glass plate (Fig. 5.3),[35] and moreover, the TERS spatial resolution of ∼12 nm was reported for the graphene flake on Au.[44] As mentioned above, TERS measurements were conducted for graphene under various special circumstances. On the other hand, there has been only little TERS work done for graphene on a opaque SiO_2/Si substrate. It is imperative to investigate the graphene on SiO_2/Si, that is the most widely used architecture for graphene devices, in order to utilize the TERS technique for nanoscale graphene devices.

This thesis work aims the demonstration of TERS measurements on graphene flakes on the SiO_2/Si substrate for realizing analysis of properties involved with the Raman spectrum on nanoscale graphene devices by using TERS technique in future. In this study, exfoliated graphene flakes on SiO_2/Si substrates are used because (1) extrinsic effects caused by device fabrication processes become more prominent thanks to its high crystal quality and (2) comparative study is possible by evaluating electrical characteristics of fabricated devices on the same platform at the same time. For these purposes, graphene nanoribbon transistors are fabricated

on the same substrate by the conventional device fabrication processes. As a result the graphene flakes on the same substrate are exposed to the same chemicals, allowing to investigate the influence of fabrication processes.

5.1.1 Measurement configuration of tip-enhanced Raman spectroscopy

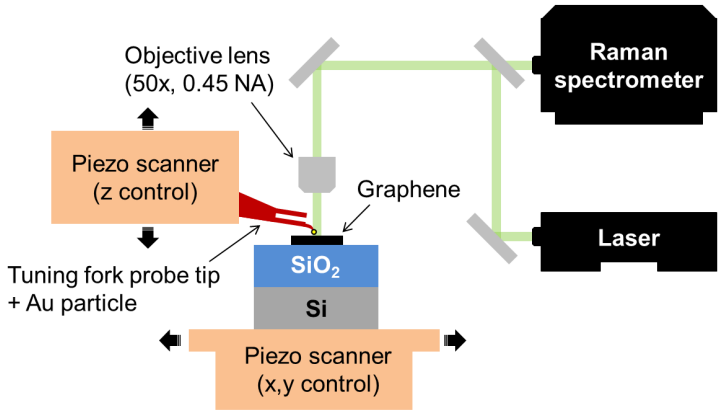

Figure 5.4: The schematic of the TERS measurement setup with the top-illumination configuration.

The integrated system comprised of the Multiview 4000 AFM system (Nanonics Imaging Ltd., Israel) and InVia Raman spectrometer (Renishaw plc, UK) is used for the TERS setup as shown in Fig. 5.4. The sample is exposed to laser from the top (top-illumination configuration), and a Raman scattering signal is collected through the same objective lens ($50\times$ magnification, numerical aperture NA $= 0.45$). The Nd-doped Y-Al-garnet laser with the wavelength λ of 532 nm is used for excitation. A quartz tuning fork with a commercial probe tip is used (Nanonics Imaging Ltd.) for the feedback of AFM imaging. This tip is coated with Au nanoparticles, whose diameter on top of the tip is $\sim$200 nm. The laser power at the sample is kept less than 0.4 mW to avoid damage to the graphene and tip by heating. During scanning measurements, the in-plane position (x, y) of the sample is controlled by the sample piezo stage, and the tip height (z) is controlled by the tuning fork feedback, so as not to misalign the laser spot and the tip location.

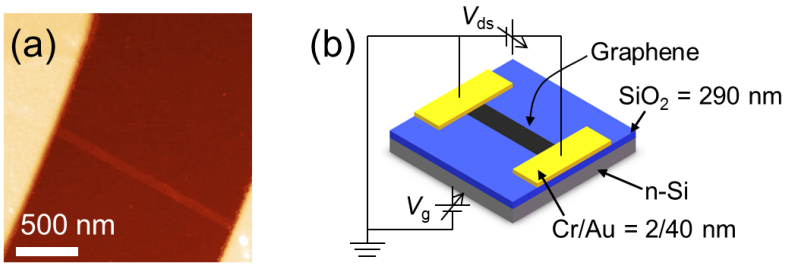

Figure 5.5: (a) AFM topographic image schematic of a graphene nanoribbon transistor. (b) Electrical measurement setup for graphene devices. Source-drain bias voltage V_{ds} is fixed in constant. Back-gate voltage V_g is applied from the heavily n-doped Si on the backside.

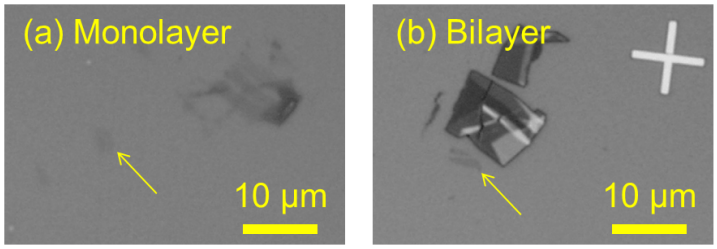

Figure 5.6: Optical images of (a) monolayer and (b) bilayer graphene. Yellow arrows point to the location of each graphene flake.

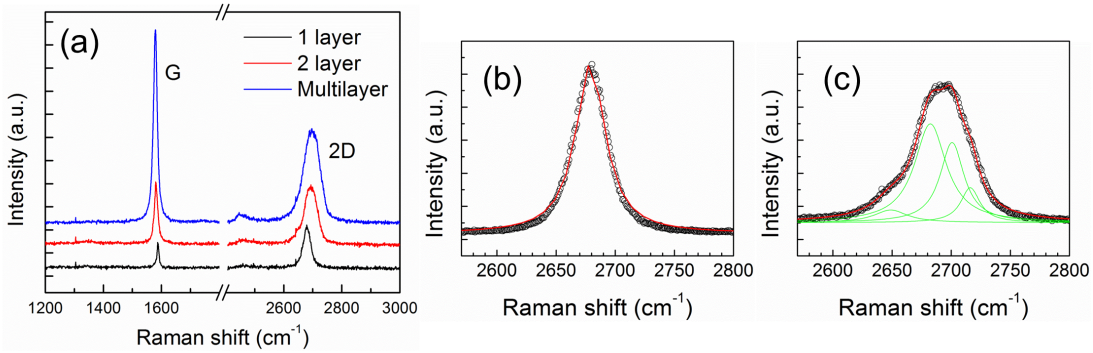

Figure 5.7: (a) Raman spectrum of the mono, bi, and multilayer graphene. The shape of G and 2D peaks is obviously different in the different number of layers. (b) 2D peak of monolayer graphene. (c) 2D peak of bilayer graphene.

5.1.2 Raman spectrum of graphene layers

The optical images of monolayer and bilayer graphene flakes on SiO_2/Si substrate are shown in Fig. 5.6, also its Raman spectrum are shown in Fig. 5.7. The number of graphene layers was identified by the contrast between graphene and SiO_2 in the optical image[49] and by fitting of the Raman spectrum peak. As shown in Fig. 5.7(a), the peak at ∼1590 cm^{-1}, called G peak, is caused by the doubly-degenerated E_{2g} vibration mode at the Brillouin zone center in the first-order Raman scattering process. The D peak located ∼1345 cm^{-1} originates in the double resonance of the second-order process between different valleys around **K** and **K′** in the Brillouin zone (intervalley scattering), which corresponds to the A_{1g} breathing mode at **K**, the in-plane transverse optical phonon.[16] This peak is activated by defects, disorders or edges with armchair geometry.[15,50] The peak at ∼2685 cm^{-1} is the 2D peak (or called G′ peak), which arises from triple resonant process of the second-order intervalley scattering. Although the 2D peak corresponds to the overtone of the D peak, it is not required neither defects nor disorder for activation. The number of graphene layers is identified by fitting to the 2D peak, which has different profile shape with respect to the number of layers.[14] The 2D peak in Fig. 5.7(b) can be fitted with a single Lorentzian function whose full width at half maximum (FWHM) is 30.8±0.2 cm^{-1}, indicating monolayer graphene. On the other hand, four Lorentzian components are needed for bilayer graphene because of the four processes involved phonons with different momenta as shown in Fig. 5.7(c). In the TERS measurement, the Raman spectrum is taken twice at the same location. The first Raman spectrum at the selected point is taken when the tip is approached and then second one when retracted from the sample with the distance between tip and sample of ∼10 μm. The spectrum with the tip approached contains both near-field and far-field effects, while the one with the tip retracted only the far-field effect.[32] The result of the near-field effect is obtained by subtracting the tip-retracted spectrum from the tip-approached one. Figure exhibits tip-approached and retracted spectra at the same point on the monolayer graphene flake. The enhancement of each peak can be confirmed in the subtracted spectrum as shown in Fig. 5.8.

Electrical characteristics for the graphene nanoribbon transistors were measured to evaluate the influence from the fabrication processes, in particular, the doping concentration of the graphene *via* the position of the

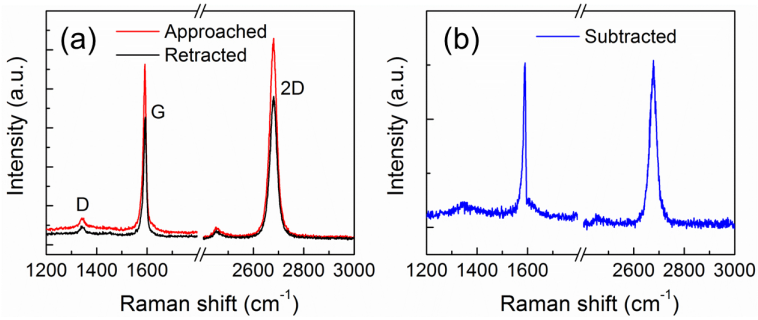

Figure 5.8: (a) Raman spectra of the monolayer graphene by the TERS measurement. The red and black lines represent the spectrum acquired when the tip is approached and retracted, respectively. (b) The subtracted Raman spectrum shown in (b) (*i.e.*, Approached−Retracted).

charge neutrality point (CNP) in resistance vs backgate voltage ($V_{\rm g}$) curves. The CNP is the point where the electron and the hole density become same, a shift of the CNP to the positive (negative) in $V_{\rm g}$ means that Fermi energy in graphene moves far in the valence (conduction) band, *i.e.*, hole (electron) doping concentration is enhanced.

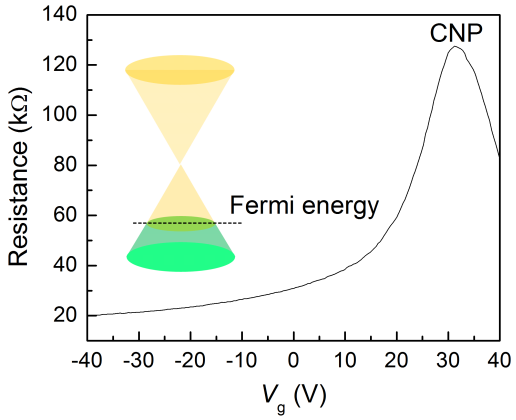

Figure 5.9: The resistance of the graphene nanoribbon transistor as a function of $V_{\rm g}$ at room temperature. The maximum resistance appears at the CNP of $V_{\rm g}$ = 31.2 V. The inset illustrates the band structure of the hole-doped graphene with Fermi energy at the valence band.

Figure 5.9 shows the measured resistance as a function of $V_{\rm g}$, and the CNP appears in the positive $V_{\rm g}$ range. The carrier density n can be estimated by the following equation;

$$n = \frac{C_{\rm g} V_{\rm CNP}}{e} \tag{5.2}$$

where, C_g is the gate capacitance per area, V_{CNP} is the gate voltage at the CNP, and e is the elemental charge. Based on the parallel plate capacitor model, $C_g = \epsilon_0\epsilon_{SiO_2}/d$, where ϵ_0 is the vacuum permittivity, ϵ_{SiO_2} is the dielectric constant of the SiO_2, and d is the thickness of SiO_2 layer, it is calculated to be $\sim$11.9 nF cm^{-2} for the dielectric SiO_2 of 290 nm. Then, the doped hole density of the device shown in Fig. 5.9 is estimated to be $\sim 2.32\times10^{12}$ cm^{-2}.

Note that, all 15 devices fabricated on the same substrate show V_{CNP} >0 V suggesting the device fabrication process is ended up with hole doping. These results suggest all the graphene on the same substrate are hole-doped. Considering the transfer process and the fact that the flakes are directly placed on SiO_2, this hole doping can be attributed to chemical charge transfer from physisorbed O_2, H_2O molecules, and polymer residues on the graphene surface.

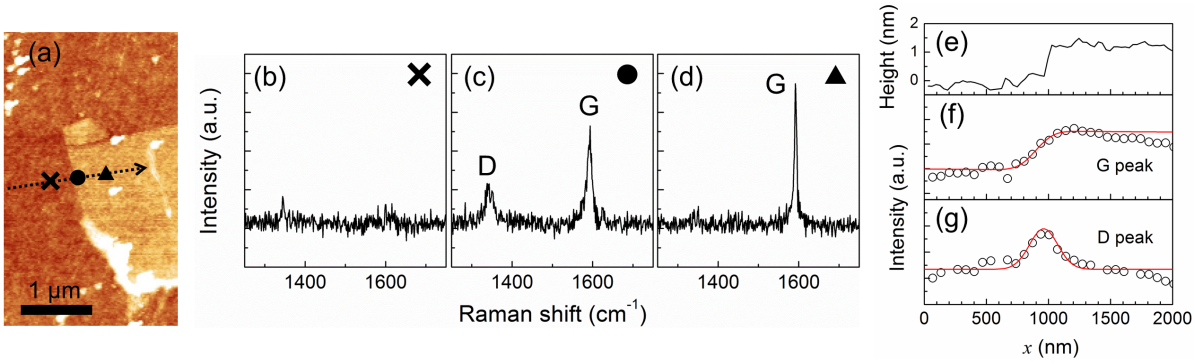

Figure 5.10: (a) The AFM image of the monolayer graphene flake. The spectral line scanning is performed along the dotted arrow. (b) The subtracted Raman spectra acquired at the cross (outside of the graphene flake), (c) the circle (edge), (d) and the triangle (inside) marks (shown in (a)), respectively. (e) The AFM height profile, (f) the intensity profile of the subtracted spectra for the G peaks and (g) the D peaks along the arrow shown in (a). The tail of the arrow corresponds to $x = 0$ nm. The red lines in (f) and (g) are fitting curves using the equation (5.3) and the Gaussian function, respectively.

Figure 5.10(a) shows an AFM topographic image of a monolayer graphene flake on the same substrate where the nanoribbon devices are fabricated. Spectral line scanning is performed across the edge of the flake along the dotted arrow drawn in Fig. 5.10(a). At the outside of the graphene flake marked by the cross mark shown in Fig. 5.10(a), both D and G peaks have not been enhanced, so the subtracted spectrum does not show any peaks (Fig. 5.10(b)). In contrast, both of peaks are enhanced at the edge marked

by the circle in Fig. 5.10(c). At the triangle mark graphene region, the G peak is enhanced while the D peak not as shown in Fig. 5.10(d). In the height profile along the scanning line shown in Fig. 5.10(e), the edge of graphene is identified at the position x ∼1000 nm. The G peak intensity starts to increase around the edge boundary, and remain constant when x >1000 nm (Fig. 5.10(f)). The D peak enhancement is observed only around the edge boundary of x ∼1000 nm as shown in Fig. 5.10(g). From the G peak intensity profile, the TERS spatial resolution is extracted using the following equation;[38]

$$\begin{aligned} I_{\mathrm{G}} &= \sqrt{\frac{\pi}{8}} A_1 w_1 \left\{ 1 - \mathrm{erf}\left(\frac{\sqrt{2}(-x + x_{\mathrm{edge}})}{w_1} \right) \right\} \\ &\quad + \sqrt{\frac{\pi}{8}} A_2 w_2 \left\{ 1 - \mathrm{erf}\left(\frac{\sqrt{2}(-x + x_{\mathrm{edge}})}{w_2} \right) \right\} \end{aligned} \tag{5.3}$$

where I_{G} is the G peak intensity in the subtracted spectrum, A_1 and A_2 are scaling factors, x_{edge} is the position of edge, w_1 and w_2 are the spatial resolution of far-field and near-field spectra, respectively. The far-field resolution is calculated based on the laser spot size to be $w_1 \approx 1.22\lambda/\mathrm{NA}$ ∼1.44 μm, and then, the TERS resolution is extracted to be w_2 ∼228 nm, which is comparable to the Au particle size at the tip. The D peak intensity profile can be fitted by a Gaussian curve with the FWHM of ∼268 nm.

As shown in Fig. 5.10(f), the G peak is enhanced from the edge boundary and remained constant beyond. Taking account of the origin of the G peak that corresponds to the E_{2g} mode, its intensity would increase with increasing the number of excited sp^2 bonded carbon rings within the laser spot. Thanks to the near-field effect the increase of the intensity of G peak in the vicinity of the edge is clearly observed. The intensity does not largely change inside the graphene flake because the exposed area is constant. On the other hand, the D peak intensity is enhanced only around x ∼1000 nm. This indicates that the D mode is strongly localized in the vicinity of the edge, which is consistent with the previous reports.[38,40] Actually in x <1000 nm, the D and the G peaks are observed both in the far-field and tip-approached Raman spectra as the laser spot (∼1 μm) is overlapped with the graphene region. However, the spectra are hardly enhanced in x <1000 nm as shown in Fig. 5.10(b), implying that the near-field spot does not reach to the graphene region. Two comparable spatial resolutions are obtained by two different two ways by curve fitting to the G peak and

the D peak intensity profile. Clearly both spatial resolutions of the TERS measurements in this study are over the diffraction limit of light. The extracted values are mainly due to the size of the Au nanoparticle on top of the tip. The message from this analysis is that TERS is also applicable for device structure analysis with a good level of the spatial resolution which is comparable to the previous TERS studies for materials.

5.1.3 Detection of local doping concentration modulation

The spectral line scanning inside the graphene flake along the arrow was also conducted as shown in Fig. 5.11(a). In the topological profile along the arrow in Fig. 5.11, a hump is identified at x ∼950 nm. Line shapes of the G peak in far-field Raman and in TERS taken at five different positions on the line are plotted in Figs. 5.11(c) and (d), respectively. There is almost no change in the far-field Raman spectra, whereas the shift of the peak positions is clearly identified in TERS. Clear difference between the far-field and tip-enhanced Raman spectra is also observed in monitoring the 2D peak as shown in Figs. 5.11(e) and (f). The peak center and FWHM of each peak are extracted using single Lorentzian curve fitting and plotted with respect to the position along the line in Figs. 5.11(g)-(j). For the far-field spectra, overall peak shift of the G and 2D peaks is less than 2 cm^{-1} in the whole range of x. On the other hand, the G peak center in TERS is 1590.47±0.28 cm^{-1} at x ∼0 nm and then shifted to 1598.14±0.23 cm^{-1} at x = 950 nm. The 2D peak center is observed to be 2675.26±1.09 cm^{-1} at x = 0 nm, and then, shifted to 2682.32±0.25 cm^{-1} at x = 950 nm. For the FWHM, again almost no change in the far-field spectra whereas the FWHM of the G peak is changed from 20 cm^{-1} at around x = 300∼800 nm to 15.69±0.75 cm^{-1} at x = 950 nm. The 2D peak FWHM is ∼30 cm^{-1} around x ∼100 nm, that broadens to be 41.56±1.04 cm^{-1} at x = 950 nm.

The results of line scanning inside the graphene are next discussed by focusing on significant peak variation observed in the TERS spectra. In normal Raman spectroscopy, such behavior could be explained by considering (i) doping and (ii) strain effects. Doping causes an up-shift for the G peak, and the G peak FWHM narrows as increasing both carrier doping as a result of the nonadiabatic Kohn anomaly.[25,26,51] The 2D peak down-shifts or up-shifts by electron or hole doping, respectively, due to charge transfer,[26] and the 2D peak FWHM broadens as increasing doping.[27] Strain effects can be discriminated either uniaxial or biaxial, and then, tensile and

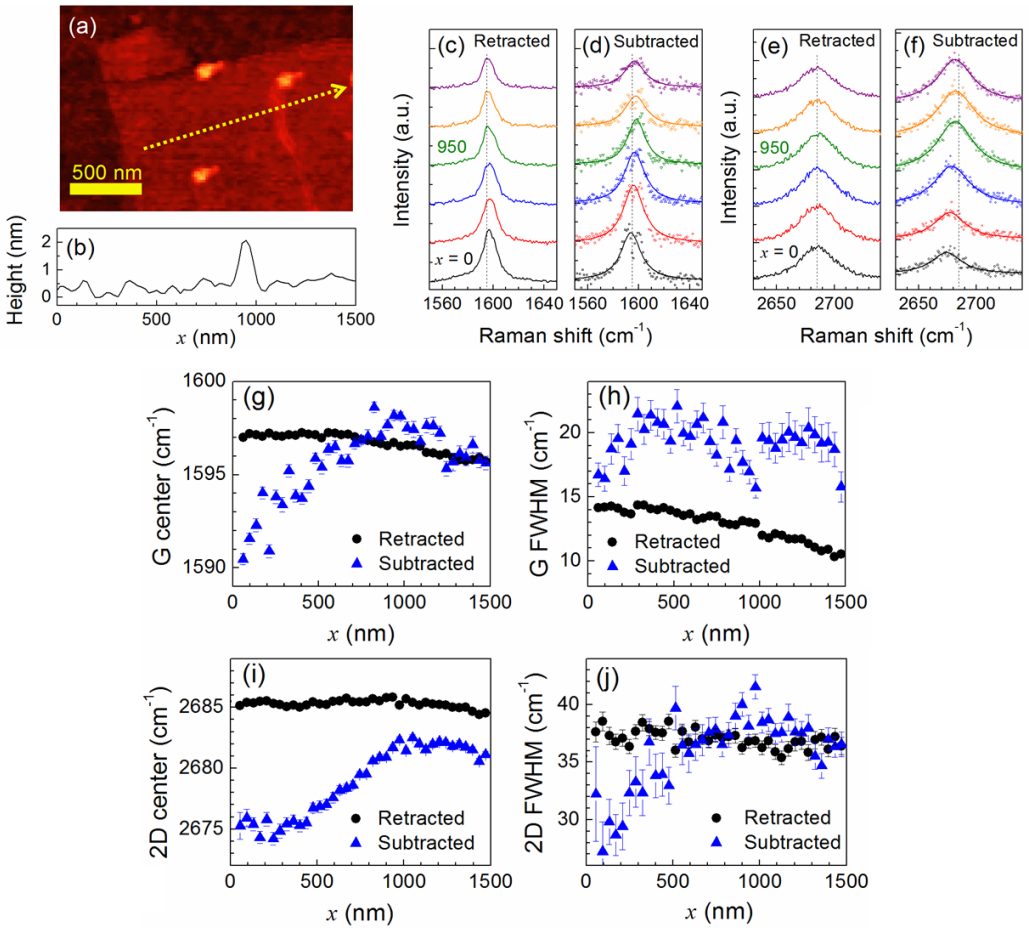

Figure 5.11: (a) The AFM image of the graphene flake. The spectral line scanning is performed along the yellow dotted arrow. (b) The AFM height profile along the arrow shown in (a). The tail of the arrow corresponds to $x = 0$ nm. (c)-(f) The tip-retracted Raman spectra and the subtracted one around the G peak (c),(d) and the 2D peak (e),(f), respectively, at each position along the arrow shown in (a). The subtracted data (symbols) are fitted with the Lorentzian curve (solid line). Each plot has the offset to be seen clearly. The black and green plots correspond to the spectrum at $x = 0$ nm and 950 nm, respectively. The vertical dotted lines in (c),(d) and (e),(f) point to 1595 cm^{-1} and 2685 cm^{-1}, respectively, for eye guides. (g),(h) The center and the FWHM of the G peak along the arrow shown in (a), respectively. (i),(j) The center and the FWHM of the 2D peak along the arrow shown in (a), respectively. In (g)-(j), the black and blue color plots are the results of the Lorentzian function fitting to the tip-retracted and the subtracted data, respectively. The error bars indicate fitting error.

compressive strain. Uniaxial strain splits the G peak into G^- and G^+ with down-shifting, and it splits or broadens the 2D peak,[21,22] while biaxial one does not affect the FWHM of both G and 2D peaks.[23] Tensile strain causes down-shift due to phonon softening, and opposite for compressive one owing to phonon stiffening.[13,19,20] According to Ref.[24], the ratio of the 2D peak shift to the G peak shift is a good index to evaluate which effect is more dominant on the Raman shift. The result of ∼0.87 at $0<x<950$ nm is much closer to 0.75, a typical value for the case that the doping effects are dominant, than to 2.2 for strain effects. Therefore, it can be interpreted that the main contribution of peak shift observed within $x = 0$∼950 nm is doping concentration modulation. Comparing the peak center at $x = 950$ nm to that at $x = 0$ nm, the 2D peak up-shifts as approaching from $x = 0$ nm to $x = 950$ nm suggesting that the position $x = 950$ nm has higher hole doping concentration than $x = 0$ nm. As is shown in the AFM image and the height profile (Figs. 5.10(a), (b)), a hump structure with ∼1.5 nm in height and ∼100 nm in width is clearly observed around $x = 950$ nm, where the enhancement of hole doping concentration is suggested by the analysis of TERS spectra.

Here I discuss how this hump structure is associated with the local doping concentration modulation. One possible explanation is that this hump structure could attract molecules to adsorb onto its surface due to the larger effective surface area than the flat region, and the adsorbates come from an ambient environment, such as moisture and O_2 molecules acting as acceptors for graphene.[3,10] In addition, use of solvent and water during fabrication can intercalate inside the wrinkle (*i.e.*, between graphene and SiO_2), resulting in inducing hole doping into graphene.[52] In contrast, the strain caused by this structure is considered very small because the aspect ratio of the height to the width is significantly small of ∼0.015. The small peak shift observed in the far-field spectra is interpreted as that local doping is averaged within ∼1 μm of the entire laser spot. Note that, Ref.[25] mentioned that the scale of charge inhomogeneity is less than 1 μm, which also agrees with this interpretation.

5.1.4 Summary

The properties of the graphene flakes on the SiO_2/Si substrate were investigated by the TERS and electrical characterization. In the electrical measurements of the graphene nanoribbon transistors on the same sub-

strate, heavily hole doping effect was found in almost devices, indicating that the graphene flakes exposed to the same chemicals in device fabrication processes could be heavily p-doped as well. By spectral line scanning across the edge of graphene, the localization of the D peak enhancement in the vicinity of the edge boundary was observed, and the TERS spatial resolution of ∼228 nm was obtained from the fitting result to the peak intensity profiles. The TERS results of being scanned inside the graphene flake also showed the distinct peak shift at different positions within ∼1 μm range, thus resolving the local doping concentration modulation with nanoscale resolution.

TERS is known as a powerful nanoscale technique for characterization of all-surface materials (1D nanostructures, graphene-like materials and polymer thin films) with the spatial resolution of a few tens of nanometers or less. The spatial resolution of TERS strongly depends on the size of the particle at the top of the AFM tip and can be improved as decreasing the size of this nanoparticle. However, the enhancement of Raman spectrum intensity is reduced, and then the signal/noise ratio decreases with decreasing the particle size. Therefore, the spatial resolution and enhancement of Raman intensity have a trade-off relation. In this study, the tip coated by a gold nanoparticle with 200 nm diameter was used since prioritizing the signal enhancement to detect the weak doping modulation effects in graphene.

Currently, 0.9 NA objectives are readily available for micro Raman spectroscopy, and have diffraction limits of around 300 nm for 532 nm laser. This is not terribly different from the TERS spatial resolution in this study. In micro-Raman, the spectra is obtained directly from the optical image and laser excitation of the graphene flakes, which could heat damage on the surface by the highly focused beam if high NA lens is used. However, TERS approach mitigates that issue by physically image the graphene surface topography, at the same time enhanced the weakly doped graphene Raman signals. The AFM information, such as high resolution topography and height profile, can be also obtained in the case of TERS. Both AFM and TERS data help to consistently analyze the morphological property on nanoscale. This is the advantage of using TERS technique compared to that of high NA micro Raman spectroscopy.

In summary, key messages from this study are (1) external modification, such as doping, is inevitably induced into graphene during device fabrication processes, and (2) TERS enables to reveal this local modifi-

cation thanks to its nanoscale spatial resolution beyond laser diffraction limit.

Even though the fabrication technology has been highly developed, it is inevitable that unintentional, distortion and contaminations can contribute to the doping effect through microfabrication processes. TERS scanning measurements can exhibit the critical position of process-induced disorder, strain, and doping concentration, and hence, one can select the region with the ideal quality of graphene for device fabrication. This study demonstrated a way to analyze the local properties associated with Raman spectroscopy in nanoscale on graphene devices based on graphene/SiO_2/Si architectures and also on opaque substrates.

Here, it is revealed that the local doping effect is distributed in nanoscale. Since it could cause the formation of unintentional QDs formation, the method to reduce these influence should be developed.

References

1) A. K. Geim, K. S. Novoselov, The rise of graphene. *Nat. Mater.* **6**, 183 (2007).

2) A. C. Ferrari, F. Bonaccorso, V. Fal'ko, K. S. Novoselov, S. Roche, P. Bøggild, S. Borini, F. H. L. Koppens, V. Palermo, N. Pugno, J. A. Garrido, R. Sordan, A. Bianco, L. Ballerini, M. Prato, E. Lidorikis, J. Kivioja, C. Marinelli, T. Ryhänen, A. Morpurgo, J. N. Coleman, V. Nicolosi, L. Colombo, A. Fert, M. Garcia-Hernandez, A. Bachtold, G. F. Schneider, F. Guinea, C. Dekker, M. Barbone, Z. Sun, C. Galiotis, A. N. Grigorenko, G. Konstantatos, A. Kis, M. Katsnelson, L. Vandersypen, A. Loiseau, V. Morandi, D. Neumaier, E. Treossi, V. Pellegrini, M. Polini, A. Tredicucci, G. M. Williams, B. H. Hong, J.-H. Ahn, J. M. Kim, H. Zirath, B. J. van Wees, H. van der Zant, L. Occhipinti, A. D. Matteo, I. A. Kinloch, T. Seyller, E. Quesnel, X. Feng, K. Teo, N. Rupesinghe, P. Hakonen, S. R. T. Neil, Q. Tannock, T. Löfwander J. Kinaret, Science and technology roadmap for graphene, related two-dimensional crystals, and hybrid systems. *Nanoscale* **7**, 4598 (2015).

3) F. Schedin, A. K. Geim, S. V. Morozov, E. W. Hill, P. Blake, M. I. Katsnelson, K. S. Novoselov, Detection of individual gas molecules adsorbed on graphene. *Nat. Mater.* **6**, 652 (2007).

4) J. Sun, W. Wang, M. Muruganathan, H. Mizuta, Low pull-in voltage graphene electromechanical switch fabricated with a polymer sacrificial layer. *Appl. Phys. Lett.* **105**, 033103 (2014).

5) J. Sun, M. E. Schmidt, M. Manoharan, H. M. H. Chong, H. Mizuta, Large-scale nanoelectromechanical switches based on directly deposited nanocrystalline graphene on insulating substrates. *Nanoscale* **8**, 6659 (2016).

6) D. Akinwande, N. Petrone, J. Hone, Two-dimensional flexible nanoelectronics. *Nat. Commun.* **5**, 5678 (2014).

7) Z. Moktadir, S. Hang, H. Mizuta, Defect-induced Fermi level pinning and suppression of ambipolar behaviour in graphene. *Carbon* **93**, 325 (2015).

8) M. L. Teague, A. P. Lai, J. Velasco, C. R. Hughes, A. D. Beyer, M. W. Bockrath, C. N. Lau, N. C. Yeh, Evidence for strain-induced local conductance modulations in single-layer graphene on SiO_2. *Nano Lett.* **9**, 2542 (2009).

9) Y. Lee, S. Bae, H. Jang, S. Jang, S.-E. Zhu, S. H. Sim, Y. I. Song, B. H. Hong, J.-H. Ahn, Wafer-scale synthesis and transfer of graphene films. *Nano Lett.* **10**, 490 (2010).

10) Y. Sato, K. Takai, T. Enoki, Electrically controlled adsorption of oxygen in bilayer graphene devices. *Nano Lett.* **11**, 3468 (2011).

11) A. Pirkle, J. Chan, A. Venugopal, D. Hinojos, C. W. Magnuson, S. McDonnell, L. Colombo, E. M. Vogel, R. S. Ruoff, R. M. Wallace, The effect of chemical residues on the physical and electrical properties of chemical vapor deposited graphene transferred to SiO_2. *Appl. Phys. Lett.* **99**, 122108 (2011).

12) J.-H. Chen, C. Jang, S. Adam, M. S. Fuhrer, E. D. Williams, M. Ishigami, Charged-impurity scattering in graphene. *Nat. Phys.* **4**, 377 (2008).

13) A. C. Ferrari, D. M. Basko, Raman spectroscopy as a versatile tool for studying the properties of graphene. *Nat. Nanotech.* **8**, 235 (2013).

14) A. C. Ferrari, J. C. Meyer, V. Scardaci, C. Casiraghi, M. Lazzeri, F. Mauri, Piscanec, D. Jiang, K. S. Novoselov, S. Roth, A. K. Geim, Raman spectrum of graphene and graphene layers. *Phys. Rev. Lett.* **97**, 187401 (2006).

15) Y. You, Z. Ni, T. Yu, Z. Shena, Edge chirality determination of graphene by Raman spectroscopy. *Appl. Phys. Lett.* **93**, 163112 (2008).

16) A. C. Ferrari, Raman spectroscopy of graphene and graphite: Disorder, electron-phonon coupling, doping and nonadiabatic effects. *Solid State Commun.* **143**, 47 (2007).

17) S. Hang, Z. Moktadir, H. Mizuta, Raman study of damage extent in graphene nanostructures carved by high energy helium ion beam. *Carbon* **72**, 233 (2014).

18) A. Eckmann, A. Felten, A. Mishchenko, L. Britnell, R. Krupke, K. S. Novoselov, C. Casiraghi, Probing the nature of defects in graphene by Raman spectroscopy. *Nano Lett.* **12**, 3925 (2012).

19) T. M. G. Mohiuddin, A. Lombardo, R. R. Nair, A. Bonetti, G. Savini, R. Jalil, N. Bonini, D. M. Basko, C. Galiotis, N. Marzari, K. S. Novoselov, A. K. Geim, A. C. Ferrari, Uniaxial strain in graphene by Raman spectroscopy: G peak splitting, Grüneisen parameters, and sample orientation. *Phys. Rev. B* **79**, 205433 (2009).

20) M. B. B. S. Larsen, D. M. A. Mackenzie, J. M. Caridad, P. Bøggild, T. J. Booth, Transfer induced compressive strain in graphene: Evidence from Raman spectroscopic mapping. *Microelectronic Eng.* **121**, 113 (2014).

21) M. Huang, H. Yan, T. F. Heinz, J. Hone, Probing strain-induced electronic structure change in graphene by Raman spectroscopy. *Nano Lett.* **10**, 4074 (2010).

22) O. Frank, M. Mohr, J. Maultzsch, C. Thomsen, I. Riaz, R. Jalil, K. S. Novoselov, G. Tsoukleri, J. Parthenios, K. Papagelis, L. Kavan, C. Galiotis, Raman 2D-band splitting in graphene: Theory and experiment. *ACS Nano* **5**, 2231 (2011).

23) J. Zabel, R. R. Nair, A. Ott, T. Georgiou, A. K. Geim, K. S. Novoselov, C. Casiraghi, Raman spectroscopy of graphene and bilayer under biaxial strain: Bubbles and balloons. *Nano Lett.* **12**, 617 (2012).

24) J. E. Lee, G. Ahn, J. Shim, Y. S. Lee, S. Ryu, Optical separation of mechanical strain from charge doping in graphene. *Nat. Commun.* **3**, 1024 (2012).

25) C. Casiraghi, S. Pisana, K. S. Novoselov, A. K. Geim, A. C. Ferrari, Raman fingerprint of charged impurities in graphene. *Appl. Phys. Lett.* **91**, 233108 (2007).

26) A. Das, S. Pisana, B. Chakraborty, S. Piscanec, S. K. Saha, U. V. Waghmare, K. S. Novoselov, H. R. Krishnamurthy, A. K. Geim, A.

C. Ferrari, A. K. Sood, Monitoring dopants by Raman scattering in an electrochemically top-gated graphene transistor. *Nat. Nanotech.* **3**, 210 (2008).

27) Q. H. Wang, Z. Jin, K. K. Kim, A. J. Hilmer, G. L. C. Paulus, C.-J. Shih, M.-H. Ham, J. D. Sanchez-Yamagishi, K. Watanabe, T. Taniguchi, J. Kong, P. Jarillo-Herrero, M. S. Strano, Understanding and controlling the substrate effect on graphene electron-transfer chemistry *via* reactivity imprint lithography. *Nat. Chem.* **4**, 724 (2012).

28) J. Wessel, Surface-enhanced optical microscopy. *J. Opt. Soc. Am. B* **2**, 1538 (1985).

29) N. Hayazawa, Y. Inouye, Z. Sekkat, S. Kawata, Metallized tip amplification of near-field Raman scattering. *Opt. Commun.* **183**, 333 (2000).

30) R. M. Stöckle, Y. D. Suh, V. Deckert, R. Zenobi, Nanoscale chemical analysis by tip-enhanced Raman spectroscopy. *Chem. Phys. Lett.* **318**, 131 (2000).

31) M. S. Anderson, Locally enhanced Raman spectroscopy with an atomic force microscope. *Appl. Phys. Lett.* **76**, 3130 (2000).

32) J. Stadler, T. Schmid, R. Zenobi, Developments in and practical guidelines for tip-enhanced Raman spectroscopy. *Nanoscale* **4**, 1856 (2012).

33) L. Rayleigh, Investigations in optics, with special reference to the spectroscope. *Philos. Mag.* **8**, 261 (1879).

34) G. G. Hoffmann, G. de With, J. Loos, Micro-Raman and tip-enhanced Raman spectroscopy of carbon allotropes. *Macromol. Symp.* **265**, 1 (2008).

35) Y. Saito, P. Verma, K. Masui, Y. Inouye, S. Kawata, Nano-scale analysis of graphene layers by tip-enhanced near-field Raman spectroscopy. *J. Raman Spectrosc.* **40**, 1434 (2009).

36) V. Snitka, R. D. Rodrigues, V. Lendraitis, Novel gold cantilever for nano-Raman spectroscopy of graphene. *Microelectronic Eng.* **88**, 2759 (2011).

37) K. Ikeda, M. Takase, N. Hayazawa, S. Kawata, K. Murakoshi, K. Uosaki, Plasmonically nanoconfined light probing invisible phonon modes in defect-free graphene. *J. Am. Chem. Soc.* **135**, 11489 (2013).

38) W. Su, D. Roy, Visualizing graphene edges using tip-enhanced Raman spectroscopy. *J. Vac. Sci. Technol. B* **31**, 041808 (2013).

39) R. H. Rickman, P. R. Dunstan, Enhancement of lattice defect signatures in graphene and ultrathin graphite using tip-enhanced Raman spectroscopy. *J. Raman Spectrosc.* **45**, 15 (2014).

40) R. Beams, L. G. Cancado, S. H. Oh, A. Jorio, L. Novotny, Spatial coherence in near-field Raman scattering. *Phys. Rev. Lett.* **113**, 186101 (2014).

41) R. Beams, L. G. Cancado, A. Jorio, A N. Vamivakas, L. Novotny, Tip-enhanced Raman mapping of local strain in graphene. *Nanotechnology* **26**, 175702 (2015).

42) F. Pashaee, F. Sharifi, G. Fanchini, F. L. Labarthet, Tip-enhanced Raman spectroscopy of graphene-like and graphitic platelets on ultraflat gold nanoplates of 20 nm. *Phys. Chem. Chem. Phys.* **17**, 21315 (2015).

43) M. Ghislandi, G. G. Hoffmann, E. Tkalya, L. Xue, G. De With, Tip-enhanced Raman spectroscopy and mapping of graphene sheets. *Appl. Spectrosc. Rev.* **47**, 371 (2012).

44) J. Stadler, T. Schmid, R. Zenobi, Nanoscale chemical imaging of single-layer graphene. *ACS Nano* **5**, 8842 (2011).

45) K. F. Domke, B. Pettinger, Tip-enhanced Raman spectroscopy of 6H-SiC with graphene adlayers: Selective suppression of E1 modes. *J. Raman Spectrosc.* **40**, 1427 (2009).

46) S. Vantasin, I. Tanabe, Y. Tanaka, T. Itoh, T. Suzuki, Y. Kutsuma, K. Ashida, T. Kaneko, Y. Ozaki, Tip-enhanced Raman scattering of the local nanostructure of epitaxial graphene grown on 4H-SiC (000$\bar{1}$). *J. Phys. Chem. C* **118**, 25809 (2014).

47) T. Suzuki, T. Itoh, S. Vantasin, S. Minami, Y. Kutsuma, K. Ashida, T. Kaneko, Y. Morisawa, T. Miurae, Y. Ozaki, Tip-enhanced Raman spectroscopic measurement of stress change in the local domain of epitaxial graphene on the carbon face of 4H-SiC(000-1). *Phys. Chem. Chem. Phys.* **16**, 20236 (2014).

48) A. Shiotari, T. Kumagai, M. Wolf, Tip-enhanced Raman spectroscopy of graphene nanoribbons on Au(111). *J. Phys. Chem. C* **118**, 11806 (2014).

49) P. Blake, E. W. Hill, A. H. Castro Neto, K. S. Novoselov, D. Jiang, R. Yang, T. J. Booth, A. K. Geim, Making graphene visible. *Appl. Phys. Lett.* **91**, 063124 (2007).

50) C. Thomsen, S. Reich, Double resonant Raman scattering in graphite. *Phys. Rev. Lett.* **85**, 5214 (2000).

51) M. Lazzeri, F. Mauri, Nonadiabatic Kohn anomaly in a doped graphene monolayer. *Phys. Rev. Lett.* **97**, 266407 (2006).

52) H. H. Kim, J. W. Yang, S. B. Jo, B. Kang, S. K. Lee, H. Bong, G. Lee, K. S. Kim, K. Cho, Substrate-induced solvent intercalation for stable graphene doping. *ACS Nano* **7**, 1155 (2013).

5.2 Reduction of doping effects by annealing

Here, the systematic study for annealing on the graphene FETs is presented. The simple method to control the CNP is proposed, which would be useful for various graphene device applications.

Graphene has attracted great interest in recent years owing to its exceptional electrical field-effect properties, such as high carrier mobility and the symmetric ambipolar characteristic[1,2]. Thus, graphene-based field-effect transistors (GFETs) have been used to investigate carrier transport properties and scattering mechanisms in graphene[3–5], as well as for various device applications, such as gas sensors[6–9], logic circuit switches[10,11] and flexible electronics[12]. The electrical properties of graphene devices are strongly affected by the measurement environment due to the large surface to volume ratio of this atomically-thick material. Consequently, clean graphene with as few external effects is required to study the intrinsic characteristics in graphene. However, contamination of the graphene surface and the interface between graphene and the substrate during conventional device fabrication is a well-known problem. One such contaminant is electron-beam (EB) resist used as patterning mask, which remains on the graphene surface and degrades the carrier mobility[13]. Furthermore, gas molecules and moisture adsorbed onto the graphene surface influence the electronic properties of graphene[6]. Thermal annealing methods are commonly used to clean the graphene surface and the interface between graphene and the substrate; for instance, annealing in a vacuum removes adsorbed molecules and polymeric residues from the graphene surface[14]. Poly (methyl methacrylate) (PMMA), a typical EB resist, was shown to be effectively removed by annealing in hydrogen gas diluted by an inert gas (argon or nitrogen)[15,16]. Moreover, thermal annealing with argon gas cures defects in graphene owing to recombination of carbon adatoms with vacancies by thermal energy[17]. In addition, rapid thermal annealing improves the contact resistance of graphene-metal junctions[18].

Even though many morphological effects of thermal annealing in graphene have been reported, the effects on the electronic transport properties of GFETs are still not fully understood, although some progress regarding the latter has been made in the past few years. It has been argued that vacuum annealing induces p-doping into graphene[19,20], however, n-doping in graphene after vacuum annealing has been reported[21,21]. This inconsistency has not yet been solved. Nevertheless, transport properties of

graphene devices will depend on the graphene surface and the interface between graphene and substrate, both of which can be modified during the annealing process. It is imperative to investigate the annealing effect in detail to make best use of the thermal annealing method for graphene.

Here, transport properties of GFETs are systematically investigated by electrical measurements before and after vacuum and hydrogen annealing, respectively. The vacuum-annealed GFETs measurements offer a solution to the inconsistency of the doping effects mentioned above. We show that the hydrogen-annealed GFET cannot return to its initial electrical properties, which sets it apart from vacuum annealing where repeatable property switching is observed. This is attributed to partial hydrogenation of the SiO_2 substrate below the graphene channel. Moreover, the asymmetric electron-hole transport is observed after each annealing, which suggests that both annealing methods affect graphene, including the region in the vicinity of the metal contacts. Finally, the experimental observations are explained with the help of density functional theory (DFT) simulation results of a trilayer graphene/SiO_2 interface model. In particular, the results imply that thermal annealing modifies the graphene surface, the interface between graphene and SiO_2, and graphene in the vicinity of the metal contacts, thus varying the transport properties of the GFET.

The transformation of systematic vacuum and hydrogen annealing effects in graphene devices on the SiO_2 surface is reported based on experimental and van der Waals interaction corrected density functional theory (DFT) simulation results. Vacuum annealing removes p-type dopants and reduces charged impurity scattering in graphene. Moreover, it induces n-type doping into graphene, leading to the improvement of the electron mobility and conductivity in the electron transport regime, which are reversed by exposing to atmospheric environment. On the other hand, annealing in hydrogen/argon gas results in smaller n-type doping along with a decrease in the overall conductivity and carrier mobility. These characteristics changes are irreversible even the graphene devices are exposed to ambience. This was clarified by DFT simulations: initially, silicon dangling bonds were partially terminated by hydrogen, subsequently, the remaining dangling bonds became active and the distance between the graphene and SiO_2 surface decreased. Moreover, both annealing methods affect the graphene channel including the vicinity of the metal contacts, which plays an important role in asymmetric carrier transport.

5.2.1 Experiment procedures

Graphene flakes were deposited by the mechanical exfoliation method from a highly ordered pyrolytic graphite on the n-doped Si substrate covered with 300 nm of SiO_2. Before deposition, the substrate was heated using a hot plate to reduce moisture on the surface. After deposition, the sample was cleaned by hot acetone at 50 °C and isopropyl alcohol. The shape and number of graphene layers were identified by the optical contrast between the substrate and the graphene flakes. In addition, Raman spectroscopy with 532 nm laser excitation was conducted for confirmation. Using a PMMA resist, EB lithography and reactive ion etching were performed to pattern the ribbon structure. Metal contacts of Cr/Au (5 nm/100 nm) were then defined by EB lithography with PMMA/MMA bilayer resists, electron beam deposition, and consecutive lift-off. The sample was not annealed during the fabrication process. For the electrical characterization, conductance of the GFETs was measured by two probe direct current measurements using a semiconductor device analyzer (Agilent B1500A) in the vacuum prober system at a low pressure of $\sim 10^{-3}$ Pa with $in-situ$ annealing capability. The hydrogen annealing was performed in the infrared lamp furnace at 370 °C with hydrogen/argon forming gas (10% H_2), using a gas flow rate of 1 L/min at atmospheric pressure for 2 hours.

The experiment was performed as follows: Step(1), measurement of the GFETs in the vacuum chamber ($\sim 10^{-3}$ Pa) before annealing; Step(2), vacuum annealing (200°C at a low pressure of $\sim 10^{-3}$ Pa for 5 hours), directly followed by electrical measurements in the vacuum without exposing the samples to an atmospheric environment; Step(3), hydrogen annealing (370°C at an atmospheric pressure for 2 hours, detailed in the experimental method section), followed by vacuum annealing and subsequently, electrical measurement.

All DFT calculations were performed based on a linear combination of numerical atomic orbitals and normconserving Troullier-Martins pseudopotentials implemented in the Atomistix ToolKit (ATK) package.[23–25] During geometric optimization, a maximum force criterions on each atom in the supercell of less than 0.01 eV $Å^{-1}$ was used. Double zeta plus polarized basis sets were used in all of these calculations. A minimum vacuum distance of 10 Å was kept between adjacent supercells in the vertical direction in all these calculations in order to avoid any spurious interactions. Energy mesh cutoff of 150 Ha and a k-point mesh of 9×9×1 in the Monkhorst-

Pack scheme were used in these calculations. For the density of states calculations, a k-point mesh of 21×21×1 in the Monkhorst-Pack grid was employed.

5.2.2 Vacuum annealing effects

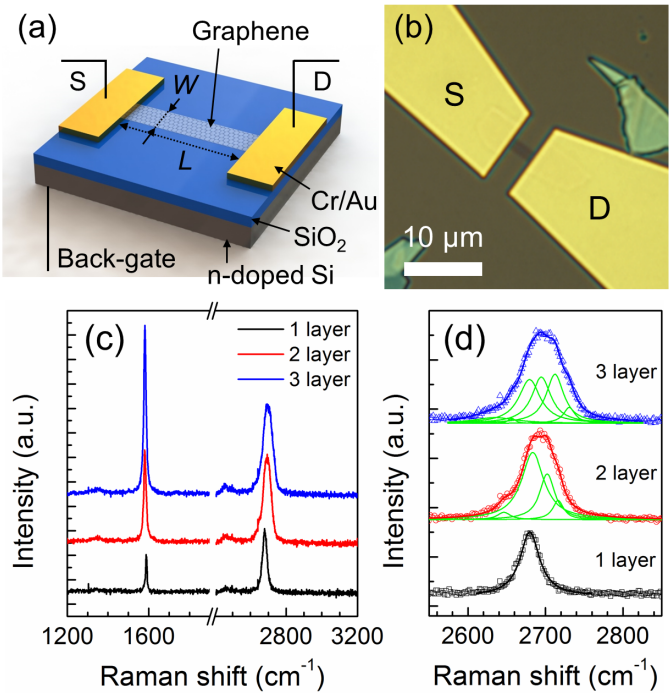

Figure 5.12: (a) Schematic of GFET comprising graphene channel contacted by source (S) and drain (D) contacts. The gate voltage is applied to the highly conducting silicon substrate. Graphene channel is patterned into the ribbon structure with designed length (L) and width (W). (b) Optical image of a typical GFET. (c) Raman spectrum of mono, bi, and trilayer GFET channels using the laser with an excitation wavelength of 532 nm. Data is vertically shifted for better visibility. (d) 2D peaks fitting results of mono, bi, and trilayer GFETs channels. Symbols, green lines, and solid lines are experimental signals, Lorentzian fit components, and fitting results, respectively.

Figures 5.12(a) and (b) present the schematic and the optical image, respectively, of a typical GFET used in this work, comprising a graphene channel with 1-3 layers, source and drain contacts, and a highly doped n-type Si substrate covered with 300 nm of SiO_2 used for back-gate modulation. Fabrication details can be found in the supplementary information. Figure 5.12(c) shows the Raman spectra of the graphene channel of various fabricated GFETs. The G peak at ∼1580 cm^{-1} and the 2D peak at ∼2700 cm^{-1} are observed in all three spectra from devices with mono, bi or trilayer graphene, respectively. The 2D peak shape is obviously different

with respect to the number of graphene layers, thereby allowing distinction of the number of layers[26]. As shown in Fig. 5.12(d), the 2D peak can be fitted with one, four, and six Lorentzian components, suggesting mono, bi, and trilayer graphene, respectively[26,27]. The effect of defects in the measured graphene can be neglected as the D peak around ∼1350 cm^{-1} is significantly smaller compared to the G peak.

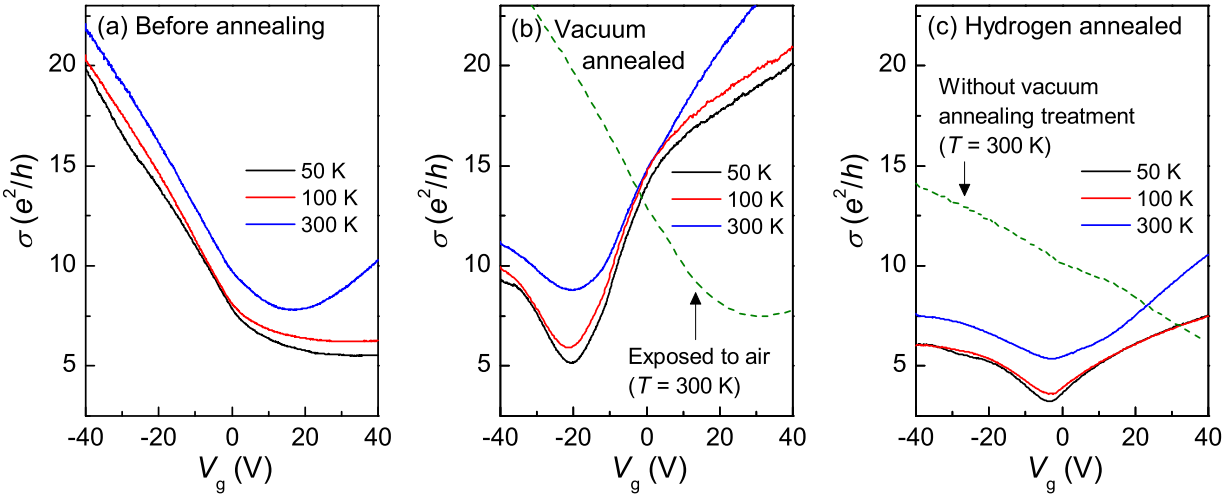

Figure 5.13: GFET channel conductivity σ versus back-gate voltage V_g curves of the trilayer GFET (a) before annealing, (b) after vacuum annealing, and (c) after hydrogen annealing, at various temperatures. V_{ds} = 1 mV for all measurements. The dotted green line in (b) is data from the sample exposed to air after vacuum annealing. The dotted green line in (c) is data measured after hydrogen annealing and before the vacuum annealing treatment.

From here, the discussion will focus on the trilayer GFET results as the results for mono and bilayer GFETs are in good agreement (see the Supporting Information)[28]. Figure 5.13 shows the conductivity (σ) of the trilayer GFET as a function of back-gate voltage (V_g) measured at various temperatures for all experiment steps. The conductivity is calculated by $\sigma = (I_d/V_{ds})(L/W)$,[3,10] where I_d is the drain current, V_{ds} is the source-drain bias voltage, L and W are the channel length and width, respectively. The charge neutrality point (CNP) is defined as the gate voltage at which the conductivity is minimized, *i.e.*, the minimum conductivity (σ_{min}) is described by $\sigma_{min} = \sigma(V_g = V_{CNP})$. At the CNP, the electron and the hole density are identical. When applying $V_g > V_{CNP}$ ($V_g < V_{CNP}$), the dominant carriers in graphene are electrons (holes). A shift of the CNP to the positive (negative) V_g range means that the graphene is p-(n-)doped. Hence, $V_{CNP} = 0$ V is observed when graphene is undoped.

Before annealing in Step(1), the CNP is observed at V_{CNP} ∼16.1 V with σ_{min} ∼$7.80e^2/h$ (e is the elementary charge, h is the Planck constant) at 300 K as shown in Fig. 5.13(a), thus the graphene is p-doped. This p-doping is caused by charge transfer from physisorbed O_2 and H_2O molecules onto the graphene surface[6,7] or the water layer at the interface between graphene and SiO_2[6,29]. The overall conductivity decreases with decreasing temperature (T), caused by the decrease in the number of thermally excited carriers in trilayer graphene.[30,31] The σ-V_{g} curves broaden around the CNP and depend linearly on V_{g} far away from the CNP (*i.e.*, $|V_{\mathrm{g}} - V_{\mathrm{CNP}}| \gg 0$, corresponding to high carrier density). These characteristics indicate that the transport is governed by charged-impurity scattering[3,4]. Therefore, the GFET is dominated by charged-impurity scattering in Step(1), which is caused by the high impurity density arising from the physisorbed molecules and the water layer.

After vacuum annealing in Step(2), a negative shift of the CNP is observed (V_{CNP} ∼−20.6 V) as shown in Fig. 5.13(b), as a result of the removal of contaminations and adsorbates from the graphene surface by the vacuum annealing[15,16]. Furthermore, thermal annealing either in a vacuum or a forming gas is known to remove the water layer at the interface between graphene and substrate, resulting in a reduction of the distance between graphene and substrate.[14] After that, charge in the SiO_2 substrate is transferred to graphene resulting in n-doping. This charge injection originates from the difference between the work functions of graphene and SiO_2[32]. Furthermore, the amount of transferred charge increases as the distance between the graphene layer and the SiO_2 substrate decreases[21]. Therefore, the n-type behavior observed in the vacuum-annealed GFET can be attributed to the removal of p-type dopants from the graphene surface and the interface of graphene/SiO_2 as well as charge transfer from SiO_2 to graphene. This interpretation will be explained later by the DFT simulation. Compared to Step(1), the overall conductivity slightly increases to σ_{min} ∼$8.78e^2/h$ at 300 K. This is presumably due to the improved contact resistance between the graphene and metal contacts after vacuum annealing[18]. The σ-V_{g} curve becomes sub-linear at high carrier density, indicating that short-range and ripple scattering dominate the carrier transport in graphene rather than charged impurities[3,33]. Consequently, the successful removal of charged impurities from the graphene by vacuum annealing is demonstrated in the transport measurement results. To confirm the reversibility of these effects, the sample was exposed to air after vac-

uum annealing and transport measurement. Indeed, the σ-V_g curve returns to the p-type characteristic similar to that in Step(1) (dashed green line in Fig. 5.13(b)). However, the CNP shifts to a larger value than in Step(1) (V_{CNP} ~30.8 V). The sites on the graphene cleaned by vacuum annealing are easily occupied by O_2 and H_2O molecules during exposure to air[14,20,34]. Therefore, the heavier p-doping effect is attributed to the larger amount of adsorption of O_2 and H_2O molecules on graphene. These results clarify the differences in the doping type in graphene after vacuum annealing reported in different studies. The n-type behavior in graphene has been observed after vacuum annealing[21,22] because the measurements were conducted in vacuum without exposure to air. On the other hand, the heavier p-doped graphene was reported[19,20] when the samples were measured in an ambient atmosphere after vacuum annealing.

5.2.3 Hydrogen annealing effects

After hydrogen annealing (Step(3)), the GFET was first measured without vacuum annealing treatment. As plotted in Fig. 5.13(c), the CNP is outside of the measured V_g range (V_{CNP} >40 V), corresponding to a heavier p-doping effect than before hydrogen annealing. It is known that the cleaning effect of hydrogen annealing on graphene is stronger than that of vacuum annealing, *i.e.*, PMMA is more effectively removed[15,16]. Thus, a larger number of p-dopants can adsorb on uncovered sites resulting in the observed transport characteristics. Next, vacuum annealing treatment was performed and unlike in Step(2), the CNP was found at V_{CNP} ~−3.4 V after the annealing and the conductivity decreased to σ_{min} ~$5.35e^2/h$. It is important to note that this reduction and the CNP shift are irreversible; even after 18 hours of continuous vacuum annealing, the conductivity and the CNP shift were not restored to the values before hydrogen annealing. However, the latter now exhibits a slight shift to the negative signifying weak n-doping. As discussed above, p-doping is reduced by vacuum annealing, and heavy n-doping can be avoided by hydrogen intercalation between graphene and the SiO_2 surface as a result of this process[28]. This result will also be discussed in detail later with the DFT calculation analysis.

5.2.4 Asymmetric transport characteristics

For a better understanding of the observed results, the annealing impacts on the relationship between electron and hole transport will be discussed,

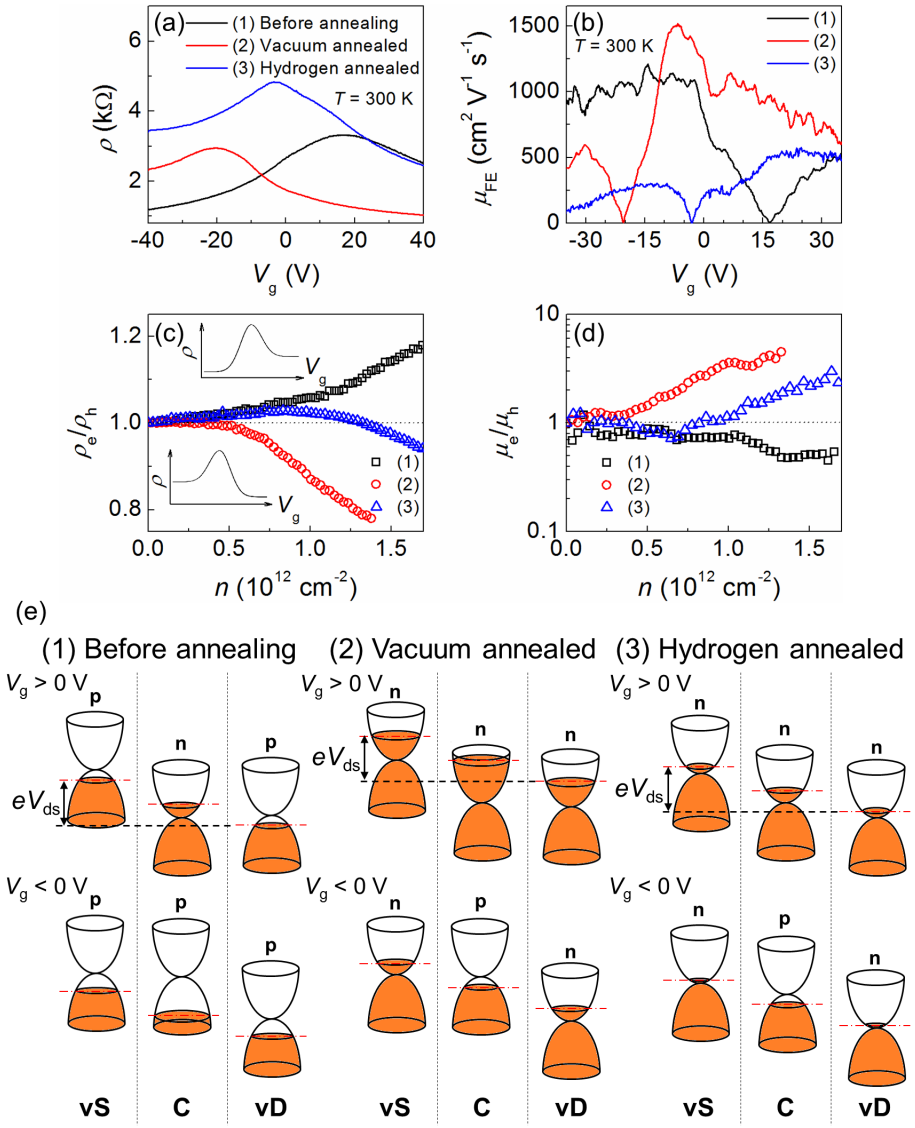

Figure 5.14: (a) Resistivity ρ versus back-gate voltage V_g characteristics at 300 K of the trilayer GFET before annealing (black), after vacuum annealing (red), and after hydrogen annealing with the vacuum annealing treatment (blue), respectively. Colors and numbers are commonly used throughout this figure. (b) Field-effect mobility μ_{FE} of the trilayer GFET as a function of V_g for all experimental steps at 300 K. The mobility is extracted following equation (5.4). (c) Ratio of the resistivity in the electron regime ρ_e and the hole regime ρ_h as a function of the carrier density n. The inset illustrates examples for asymmetric ρ-V_g curves. The upper (lower) one corresponds to the case of $\rho_e/\rho_h > 1$ ($\rho_e/\rho_h < 1$). The dotted line signifies $\rho_e/\rho_h = 1$. (d) Ratio of the mobility in the electron regime μ_e and the hole regime μ_h in a logarithmic scale as a function of the carrier density n. The dotted line signifies $\mu_e/\mu_h = 1$. (e) Schematic energy diagram in the trilayer GFET for all experimental steps, when applying $V_g < V_{CNP}$ and $V_g > V_{CNP}$. Left, center, right parabolic structures represent the band structure of trilayer graphene in the vicinity of source metal contact (vS), at the channel center (C), and in the vicinity of drain metal contact (vD), respectively. The Fermi energies in the individual regions are shown by red dashed lines.

in particular, the symmetricity between electron and hole transport in resistivity and mobility. The field-effect mobility (μ_{FE}) is extracted by the direct transconductance method[10,35,36] using the following equation:

$$\mu_{\mathrm{FE}} = \frac{dI_{\mathrm{d}}}{dV_{\mathrm{g}}}\frac{L}{WC_{\mathrm{g}}V_{\mathrm{ds}}} \tag{5.4}$$

where, C_{g} is the gate capacitance per unit area (C_{g} ~1.15×10^{-8} F cm^{-2} for SiO_2 with 300 nm thickness). As shown in Figs. 5.14(a) and (b), the asymmetric resistivity and carrier mobility between the electron regime and the hole regime are observed. In order to be seen clearly, the ratio of the resistivity in the electron regime $\rho_{\mathrm{e}} = \rho(V_{\mathrm{g}} > V_{\mathrm{CNP}})$ to the hole regime $\rho_{\mathrm{h}} = \rho(V_{\mathrm{g}} < V_{\mathrm{CNP}})$ is plotted as a function of carrier density (n) induced by applying V_{g}, described by $n = (C_{\mathrm{g}}/e)(V_{\mathrm{g}} - V_{\mathrm{CNP}})$ (Fig. 5.14(c)). In the same way, Fig. 5.14(d) exhibits the ratio of the electron mobility $\mu_{\mathrm{e}} = \mu_{\mathrm{FE}}(V_{\mathrm{g}} > V_{\mathrm{CNP}})$ to the hole mobility $\mu_{\mathrm{h}} = \mu_{\mathrm{FE}}(V_{\mathrm{g}} < V_{\mathrm{CNP}})$.

The asymmetric carrier transport is basically associated with the additional resistance from the p-n junction formed in graphene at the vicinity of the metal contacts[37–39]. The back-gate modulates the Fermi level in graphene including the region in the vicinity of the metal contacts. However, the metal contacts induce the high density of state in graphene in the vicinity of the metal, where the Fermi level shifting by applying V_{g} becomes smaller than that in the channel center region. Consequently, the CNP in graphene near the metal is misaligned with that in the channel center region, leading to the formation of p-n junction in graphene near the source and drain electrodes[40].

Before annealing, higher resistivity is observed in the electron regime than the hole regime, and the hole mobility is higher than the electron mobility. The highest electron and hole mobility are μ_{e} ~528 $\mathrm{cm}^2\mathrm{V}^{-1}\mathrm{s}^{-1}$, and μ_{h} ~1210 $\mathrm{cm}^2\mathrm{V}^{-1}\mathrm{s}^{-1}$, respectively. Seemingly, the hole transport is predominant over electron transport. In the case when no external electric field is applied, the graphene including the vicinity of the metal contacts is p-doped. When changing the Fermi level of graphene by applying $V_{\mathrm{g}} > V_{\mathrm{CNP}}$, the channel center region is tuned to n-type. However, the region near the metal remains p-type because of the smaller Fermi level shifting[38,39], *i.e.*, the Fermi level is maintained in the valence band (Fig. 5.14(e)). Consequently, the GFET forms the p-n-p ($V_{\mathrm{g}} > V_{\mathrm{CNP}}$) and p-p-p ($V_{\mathrm{g}} < V_{\mathrm{CNP}}$) junctions in graphene, which leads to low ρ_{h} and high μ_{h}.

On the other hand, the electron transport is dominant after vacuum

annealing. The electron and hole mobility are μ_e ~1518 $cm^2V^{-1}s^{-1}$ and μ_h ~597 $cm^2V^{-1}s^{-1}$, respectively. Similar to Step(1), applying V_g changes the Fermi level in graphene. The graphene at the channel center is modulated to be p-type, whereas the region in the vicinity of the metal remains n-type (Fig. 5.14(e)), leading to the formation of n-n-n ($V_g > V_{CNP}$) and n-p-n ($V_g < V_{CNP}$) junctions in the GFET, resulting in low ρ_e and high μ_e.

After hydrogen annealing and the vacuum annealing treatment, the GFET exhibits the symmetric resistivity and mobility of ρ_e/ρ_h ~1 and μ_e/μ_h ~1 at low carrier concentrations ($n < 1 \times 10^{12}$ cm^{-2}). The maximum electron mobility is μ_e ~574 $cm^2V^{-1}s^{-1}$ at high n, whereas the hole mobility is μ_h ~305 $cm^2V^{-1}s^{-1}$. By increasing n, the proportion of electron transport is enhanced, *i.e.*, ρ_e/ρ_h decreases and μ_e/μ_h increases, pointing to n-doped graphene similar to that in Step(2).

Importantly, both annealing processes change the symmetricity of carrier transport in graphene. Taking all annealing steps into account, the doping type in graphene in the vicinity of the source/drain electrodes is changed from p-type (Step(1)) to n-type (Steps(2) and (3)). Hence, this result indicates that annealing affects not only the graphene near the channel center but also the region in the vicinity of the metal contacts[37–39].

Here the monolayer and bilayer graphene FETs are discussed.

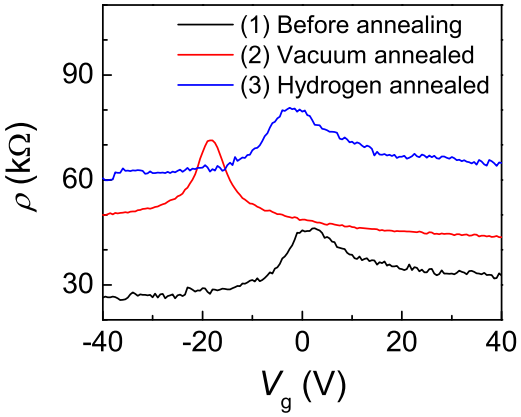

Figure 5.15: Resistivity ρ versus back-gate voltage V_g characteristics at 300 K of the monolayer GFET before annealing (black), after vacuum annealing (red), and after hydrogen annealing with the vacuum annealing treatment (blue), respectively.

Figures 5.15 and 5.16 show the resistivity (ρ) of the monolayer and bilayer GFETs as a function of back-gate voltage (V_g) measured at room temperature for all experiment steps, respectively. Before annealing, almost GFETs including monolayer and bilayer devices show the charge near CNP in the positive V_g at 300 K. The p-doping effect is caused by physisorbed

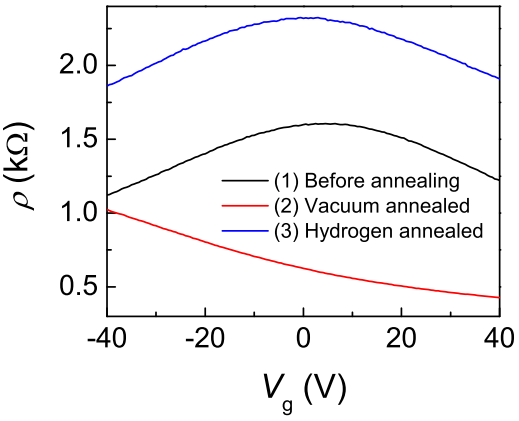

Figure 5.16: Resistivity ρ versus back-gate voltage V_g characteristics at 300 K of the bilayer GFET before annealing (black), after vacuum annealing (red), and after hydrogen annealing with the vacuum annealing treatment (blue), respectively.

O_2 and H_2O molecules onto the surface. However, some devices randomly exhibit the CNP in the negative side or near 0 V, which might be attributed to unintentional contaminations or impurities. After vacuum annealing, a negative shift of the CNP is observed in the almost GFETs. This result can be ascribed to the removal of p-type dopants from the graphene surface and the interface of graphene/SiO_2.After hydrogen annealing and the vacuum annealing treatment, the CNP is found around V_g ~0 V and the overall resistivity increases as well as the trilayer GFETs. The observation of the CNP close to 0 V indicates that either p- or n-doping level was reduced. According to our DFT calculation, the small shift of the CNP and the irreversible reduction of the overall conductivity can be attributed to a decrease in distance between the graphene and the SiO_2 substrate due to partial hydrogenation at the SiO_2 surface.

5.2.5 Simulation of interaction between graphene and SiO_2

In order to gain a better understanding of the microscopic details of hydrogen annealing effects on the GFET, DFT simulations were performed. In these simulations, graphene layers were placed on the quartz SiO_2 (0001) surface. A SiO_2 slab supercell with 16 layers was used, and the backside of the SiO_2 was passivated with hydrogen atoms. As the lattice mismatch is small between the graphene and the SiO_2 slab, the interface has a low mean absolute strain of 0.09%. This small strain is maintained in the SiO_2 layer in order to keep the graphene in a pristine state. Interaction between graphene and SiO_2 varies according to the surface state

of the SiO_2. In first-principles calculations of Graphene/SiO_2 systems, local density approximation (LDA)[41,42] and generalized gradient approximation (GGA) exchange-correlation functionals are used[21,43]. For the DFT calculations of layered materials, LDA exchange-correlation functionals include the local interactions only; hence, long-range dispersion interactions are not properly described. On the other hand, in the GGA functionals van der Waals (vdW) interactions are not included. In order to choose the most suitable exchange-correlation functional for graphene/SiO_2 relevant to the explanation of the reported experimental results, monolayer graphene/SiO_2 system simulations were performed with and without hydrogenation at the graphene/SiO_2 interface (details are given in the Supporting Information). For the LDA functional, formation of strong Si-C bonds with 1.9 Å bond length was observed when one of the two silicon dangling bonds is terminated by hydrogen, leading to a high density of defect states around the Fermi level and the band-gap opening at low and higher energies (Fig. S3). In the case of the Revised Perdew-Burke-Ernzerhof parametrization of the GGA (GGA-RPBE)[44] functional with the Grimme DFT-D3 dispersion correction[45], slight n-doping with defects states was reflected in the graphene density of states (DOS) (Fig. S3) with ambipolar characteristics. This result is more relevant to the experimental results reported[28] than LDA functional calculations. Based on these results, the GGA-RPBE functional with Grimme DFT-D3 dispersion correction was chosen for further simulations of trilayer graphene with a SiO_2 substrate. As the DFT-D3 correction method includes more accurate dispersion coefficients based on local geometry, this functional will give more accurate modeling of the vdW interaction between trilayer graphene and SiO_2 substrate. The adsorption energy of monolayer graphene onto a SiO_2 substrate is calculated through the difference between the total energy of the combined graphene/SiO_2 substrate supercell and the sum of the total energies of the isolated graphene and SiO_2 substrate supercells. The adsorption energy of 19.88 meV/Å^2 is consistent with the adsorption energy of 21.77 meV/Å^2 calculated by the Tkatchenko and Scheffler method (vdW-TS) based on the mean-field ground-state electron density of molecules and solids for the reconstructed SiO_2 substrate[46]. Also, the calculated equilibrium distance of 3.2078 Å between the graphene and SiO_2 is in good agreement with the vdW-TS method[46].

Monolayer graphene/SiO_2 system simulations were done with and without hydrogenation at the graphene/SiO_2 interface. Details of the simu-

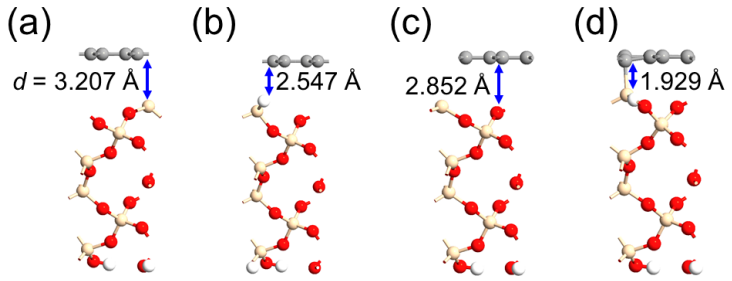

Figure 5.17: Atomic configuration side view of the geometrically optimized structure of monolayer graphene on Quartz SiO_2 (0001) surface: (a) without any defects, and (b) one of the silicon dangling bonds in (a) is terminated by a hydrogen with GGA-RPBE exchange correlation functionals with DFT-D3 corrections; (c) without any defects, and (d) one of the silicon dangling bonds in (a) is terminated by a hydrogen with LDA exchange correlation functionals.

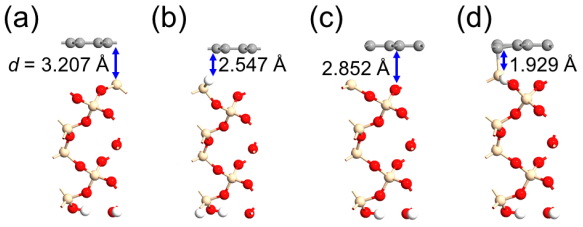

Figure 5.18: PDOS plot of the monolayer graphene of the geometrically optimized structures shown in Fig. 5.17 with exchange correlation functionals of GGA-RPBE with DFT-D3 corrections and LDA.

lation method are given in the main text. To analysis the interaction between monolayer graphene and SiO_2 substrate, DFT calculations were done with revised Perdew-Burke-Ernzerhof parametrization of the GGA (GGA-RPBE)[44] functional with the Grimme DFT-D3 dispersion and LDA functional. For DFT-D3 calculation, distance between the graphene and the top SiO_2 surface is 3.207 Å , which is reduced to 2.547 Å when a single dangling bond of a Si atom is terminated by the hydrogen (Figs. 5.17(a) and (b)). In the case of For the LDA functional, optimized distance between the graphene and the top of SiO_2 surface is 2.852 Å . This value is lower than interlayer distance of graphite. When a single dangling bond of a Si atom is terminated by the hydrogen then strong Si-C bond is formed with 1.9 Å bond length (Figs. 5.17(c) and (d)). This leads to a high density of defect states around the Fermi level and the band-gap opening at low and higher energies (Fig. 5.18(d)).

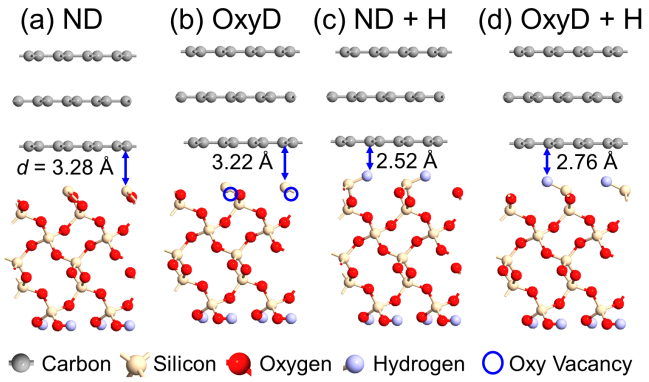

Figure 5.19: Side view of the geometrically optimized structure of trilayer graphene on Quartz SiO_2 (0001) surface used for DFT simulation (a) without any defects (ND), (b) oxygen deficiency (OxyD), (c) one of the Si dangling bonds in (a) is terminated with a hydrogen (ND + H), and (d) one of the dangling bonds in the oxygen deficiency supercell in (b) is terminated with a hydrogen (OxyD + H). Gap between the bottom graphene layer and topmost atom of the SiO_2 layer is shown. These side views are taken for two supercells in the horizontal direction.

The geometrically optimized structure of trilayer graphene on the defectless SiO_2 substrate is shown in Fig. 5.19(a). In the model for SiO_2 layer with no defect (ND), the distance between the topmost atoms of SiO_2 to bottommost atoms of graphene is 3.28 Å. The projected density of states (PDOS) of trilayer graphene in this configuration clearly shows the ambipolar characteristics (Fig. 5.20(a)). As explained before, long duration vacuum annealing of graphene devices leads to n-type doping, which is attributed to the significant surface state density in SiO_2[13,32]. These states

originate from oxygen deficiency induced Si dangling bonds[47]. In order to clarify if the impact of oxygen deficiencies is consistent with the reported graphene device characteristics, one oxygen atom was removed from the top surface of SiO_2 supercell and then geometrical optimization was performed as shown in Fig. 5.19(b) (OxyD). The reduction in the gap between graphene and the SiO_2 layer, from 3.28 Å to 3.22 Å , is clearly visible in Fig. 5.19(b). This small decrease in the gap is consistent with the experimental observation of almost comparable conductivity in the vicinity of the CNP and field-effect mobility of the trilayer graphene devices before and after vacuum annealing (see Figs. 5.13 and 5.14). Device characteristics are strongly affected by the gap. Surface states are induced in the SiO_2 layer below the Fermi level due to the oxygen deficiencies as indicated by red arrow in Fig. 5.20. These states will also affect the graphene device doping characteristics. This leads to n-doping of graphene in the transport characteristics in order to balance the chemical potential at the interface[21].

The measurements of the hydrogen-annealed device shown earlier were clearly irreversible (see Figs. 5.13 and 5.14), and can be explained based on the DFT simulations. Hydrogen intercalation at room temperature and molecular hydrogen production at a low temperature of 400 K have already been reported for the graphene/metal interface[48]. As the hydrogen annealing in this study was performed at 643 K in an infrared lamp furnace at atmospheric pressure for 2 hours, hydrogen intercalation at the graphene/SiO_2 interface was expected[28]. To simulate the impact of hydrogen intercalation at this interface, one of the topmost Si atoms was terminated by hydrogen in our model (Fig. 5.19(c), ND + H). Then, geometrical optimization was performed while allowing the upper SiO_2 atoms and the graphene atoms to move freely. The gap between the bottom graphene atoms and the topmost atoms of the SiO_2 supercell decreased significantly from 3.28 Å to 2.52 Å. When one of the two Si dangling bonds is satisfied by a hydrogen atom, the other dangling bond becomes more active, resulting in the forceful decrease of the gap and charge rearrangement. This is reflected as the weak n-doping after hydrogen annealing observed.

On the other hand, it is possible to partially terminate the dangling bond created by the oxygen deficiencies at the SiO_2 surface *via* hydrogen annealing. When one of these dangling bonds is terminated by hydrogen it also leads to a decrease in the gap between the bottom graphene layer and SiO_2 layer topmost atom from 3.22 Å to 2.76 Å (Fig. 5.19(d), OxyD + H). Furthermore, the decrease in the gap clearly justifies the decrease in the

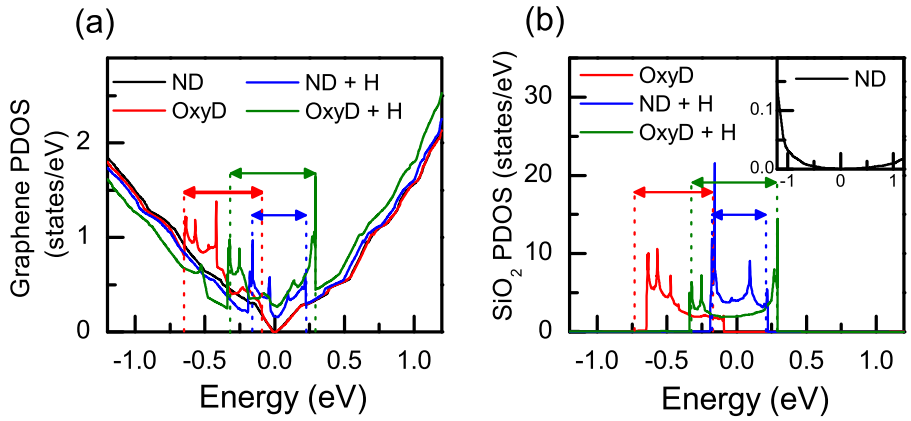

Figure 5.20: (a) PDOS of the trilayer graphene of the geometrically optimized structures shown in Fig. 5.19. (b) PDOS of the SiO_2 layers shown in Fig. 5.19, inset shows the PDOS plot of the SiO_2 layer without any defects (ND). Energy range of surface states for individual structures is highlighted by colored arrows.

conductivity and field-effect mobility of the trilayer graphene devices after hydrogen annealing. This reduced gap might suppress further hydrogen intercalation to terminate another dangling bond that coexists in the same Si atom. The decrease in the gap is also consistent with the degradation of experimental conductivity and field-effect mobility results after hydrogen annealing. These two cases of hydrogen terminations lead to defect states around the Fermi level as indicated by blue and green arrows, rather than far below the Fermi level compared with the oxygen deficiency supercell (Fig. 5.20).

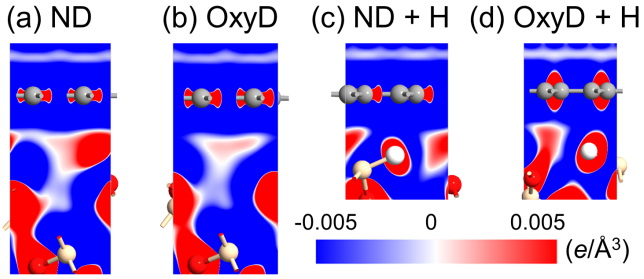

Figure 5.21: Cut plane images of electron difference density super imposed on the atomic structure for the SiO_2 (0001) surface: (a) without any defects (ND), (b) with an oxygen deficiency (OxyD), (c) one of the Si dangling bonds in (a) is terminated with a hydrogen (ND + H), and (d) one of the dangling bonds in (b) is terminated with a hydrogen (OxyD + H). For (a) and (b) plots, cut planes are kept in the same position of the supercell. Cut planes in the plots of (c) and (d) are kept across the hydrogen atom for more clarity. In these plots, the bottom layer graphene and the top layer of the SiO_2 slab are shown.

Finally, the charge redistribution caused by the hydrogen termination

of the SiO_2 dangling bonds was evaluated by the electron difference density, *i.e.*, the difference between the self-consistent valence charge density and the superposition of atomic valence densities. A clear charge isolation (zero electron difference density is depicted by the white region) was found between the graphene layer and the SiO_2 layer for the defectless substrate (compare Fig. 5.21(a)). In contrast, when an oxygen deficiency was introduced in the SiO_2 layer, a continuous charge depletion region connecting the SiO_2 and graphene can be clearly noticed (Fig. 5.21(b)). This elucidates the n-doping process of graphene after the vacuum annealing (Fig. 5.13(b)). As the gap between the graphene layer and the SiO_2 layer is reduced when one of the Si dangling bonds or oxygen deficiency dangling bonds is terminated with a hydrogen, clear charge mixing between the bottom graphene layer and the SiO_2 layer exists as shown in Figs. 5.21(c) and (d). These results substantiate the experimental observation of the decrease in the conductivity and mobility of the hydrogen annealed graphene devices.

5.2.6 Summary

We report the effects of vacuum and hydrogen annealing in the GFETs on SiO_2 surface by experimental and vdW-corrected DFT simulation results. It is found that vacuum annealing removes p-type dopants and reduces charged-impurity scattering in graphene. Simultaneously, it induces n-doping into graphene due to charge transfer from SiO_2 to graphene, improving the electron mobility and the conductivity in the electron regime. In contrast, hydrogen annealing irreversibly degrades the overall conductivity and carrier mobility while minimizing the doping concentrations. DFT simulation results show that the hydrogen annealing leads to the decrease in the distance between the graphene and the SiO_2 substrate due to partial hydrogenation at the SiO_2 surface. Both annealing methods affect the graphene channel including the vicinity of the metal contacts, which plays an important role in asymmetric carrier transport. This systematic study clarifies the microscopic impact of vacuum and hydrogen annealing on graphene devices, providing guidance for future graphene sensors as well as other devices.

Vacuum annealing can be used to control the position of the CNP, *i.e.*, doping effects on graphene reversibly. This must be useful for the transport measurements on the graphene nanodevices as well.

References

1) K. S. Novoselov, A. K. Geim, S. V. Morozov, D. Jiang, Y. Zhang, S. V. Dubonos, I. V. Grigorieva, A. A. Firsov, Electric field effect in atomically thin carbon films. *Science* **306**, 666 (2004).

2) A. K. Geim, K. S. Novoselov, The rise of graphene. *Nat. Mater.* **6**, 183 (2007).

3) J. H. Chen, C. Jang, S. Adam, M. S. Fuhrer, E. D. Williams, M. Ishigami, Charged-impurity scattering in graphene. *Nat. Phys.* **4**, 377 (2008).

4) S. Xiao, J. H. Chen, S. Adam, E. D. Williams, M. S. Fuhrer, Charged-impurity scattering in bilayer graphene. *Phys. Rev. B* **82**, 041406(R) (2010).

5) Y. W. Tan, Y. Zhang, K. Bolotin, Y. Zhao, S. Adam, E. H. Hwang, S. Das Sarma, H. L. Stormer, P. Kim, Measurement of scattering rate and minimum conductivity in graphene. *Phys. Rev. Lett.* **99** 246803 (2007).

6) F. Schedin, A. K. Geim, S. V. Morozov, E. W. Hill, P. Blake, M. I. Katsnelson, K. S. Novoselov, Detection of individual gas molecules adsorbed on graphene. *Nat. Mater.* **6**, 652 (2007).

7) Y. Sato, K. Takai, T. Enoki, Electrically controlled adsorption of oxygen in bilayer graphene devices. *Nano Lett.* **11**, 3468 (2011).

8) M. Muruganathan, J. Sun, T. Imamura, H. Mizuta, Electrically tunable van der Waals interaction in graphene-molecule complex. *Nano Lett.* **15**, 8176 (2015).

9) J. Sun, M. Muruganathan, H. Mizuta, Room temperature detection of individual molecular physisorption using suspended bilayer graphene. *Sci. Adv.* **2**, e1501518 (2016).

10) F. Schwierz, Graphene transistors. *Nat. Nanotech.* **5**, 487 (2010).

11) D. Reddy, L. F. Register, G. D. Carpenter, S. K. Banerjee, Graphene field-effect transistors. *J. Phys. D: Appl. Phys.* **44**, 313001 (2011).

12) B. K. Sharma, J. H. Ahn, Graphene based field effect transistors; Efforts made towards flexible electronics. *Solid State Electron.* **89**, 177 (2013).

13) A. Pirkle, J. Chan, A. Venugopal, D. Hinojos, C. W. Magnuson, S. McDonnell, L. Colombo, E. M. Vogel, R. S. Ruoff, R. M. Wallace, The effect of chemical residues on the physical and electrical properties of chemical vapor deposited graphene transferred to SiO_2. *Appl. Phys. Lett.* **99**, 122108 (2011).

14) K. Kumar, Y. S. Kim, E. H. Yang, he influence of thermal annealing to remove polymeric residue on the electronic doping and morphological characteristics of graphene. *Carbon* **65**, 35 (2013).

15) M. Ishigami, J. H. Chen, W. G. Cullen, M. S. Fuhrer, E. D. Williams, Atomic structure of graphene on SiO_2. *Nano Lett.* **7**, 1643 (2007).

16) Y. C. Lin, C. C. Lu, C. H. Yeh, C. Jin, K. Suenaga, P. W. Chiu, Graphene annealing: How clean can it be? *Nano Lett.* **12**, 414 (2012).

17) J. Chen, T. Shi, T. Cai, T. Xu, L. Sun, X. Wu, D. Yu, Self healing of defected graphene. *Appl. Phys. Lett.* **102**, 103107 (2013).

18) O. Balci, C. Kocabas, Rapid thermal annealing of graphene-metal contact. *Appl. Phys. Lett.* **101**, 243105 (2012).

19) Z. Cheng, Q. Zhou, C. Wang, Q. Li, C. Wang, Y. Fang, Toward intrinsic graphene surfaces: A systematic study on thermal annealing and wet-chemical treatment of SiO_2-supported graphene devices. *Nano Lett.* **11**, 767 (2011).

20) Z. H. Ni, H. M. Wang, Z. Q. Luo, Y. Y. Wang, T. Yu, Y. H. Wu, Z. X. Shen, The effect of vacuum annealing on graphene. *J. Raman Spectrosc.* **14**, 479 (2010).

21) H. E. Romero, N. Shen, P. Joshi, H. R. Gutierrez, S. A. Tadigadapa, J. O. Sofo, P. C. Eklund, n-type behavior of graphene supported on Si/SiO_2 substrates. *ACS Nano* **2**, 2037 (2008).

22) P. Joshi, H. E. Romero, A. T. Newal, V. K. Toutam, S. A. Tadigadapa, Intrinsic doping and gate hysteresis in graphene field effect devices fabricated on SiO_2 substrates. *J. Phys.: Condens. Matter* **22**, 334214 (2010).

23) Atomistrix ToolKit version 2015.1, QuantumWise A/S Home Page. www.quantumwise.com (accessed Jan. 6, 2017).

24) M. Brandbyge, J. L. Mozos, P. Ordejón, J. Taylor, K. Stokbro, Density-functional method for nonequilibrium electron transport. *Phys. Rev. B* **65**, 165401 (2002).

25) J. M. Soler, E. Artacho, J. D. Gale, A. García, J. Junquera, P. Ordejón, D. Sánchez-Portal, The SIESTA method for ab initio order-N materials simulation. *J. Phys.: Condens. Matter* **14**, 2745 (2002).

26) L. M. Malarda, M. A. Pimentaa, G. Dresselhaus, M. S. Dresselhaus, Raman spectroscopy in graphene. *Phys. Rep.* **473**, 51 (2009).

27) C. Cong, T. Yu, K. Sato, J. Shang, R. Saito, G. F. Dresselhaus, M. S. Dresselhaus, Raman characterization of ABA- and ABC-stacked trilayer graphene. *ACS Nano* **5**, 8760 (2011).

28) T. Iwasaki, J. Sun, N. Kanetake, T. Chikuba, M. Akabori, M. Muruganathan, H. Mizuta, Hydrogen intercalation: An approach to eliminate silicon dioxide substrate doping to graphene. *Appl. Phys. Express* **8**, 015101 (2015).

29) H. Komurasaki, T. Tsukamoto, K. Yamazaki, T. Ogino, Layered structures of interfacial water and their effects on Raman spectra in graphene-on-sapphire systems. *J. Phys. Chem. C* **116**, 10084 (2012).

30) M. F. Craciun, S. Russo, M. Yamamoto, J. B. Oostinga, A. F. Morpurgo, S. Tarucha, Trilayer graphene is a semimetal with a gate-tunable band overlap. *Nat. Nanotech.* **4**, 383 (2009).

31) W. Zhu, V. Perebeinos, M. Freitag, P. Avouris, Carrier scattering, mobilities, and electrostatic potential in monolayer, bilayer, and trilayer graphene. *Phys. Rev. B* **80**, 235402 (2009).

32) Y. Shi, X. Dong, P. Chen, J. Wang, L. J. Li, Effective doping of single-layer graphene from underlying SiO_2 substrates. *Phys. Rev. B* **79**, 115402 (2009).

33) E. H. Hwang, S. Adam, S. Das Sarma, Carrier transport in two-dimensional graphene layers. *Phys. Rev. Lett.* **98**, 186806 (2007).

34) S. Ryu, L. Liu, S. Berciaud, Y. J. Yu, H. Liu, P. Kim, G. W. Flynn, L. E. Brus, Atmospheric oxygen binding and hole doping in deformed graphene on a SiO_2 substrate. *Nano Lett.* **10**, 4944 (2010).

35) Z. Chen, J. Appenzeller, Mobility extraction and quantum capacitance impact in high performance graphene field-effect transistor devices. *IEDM Tech. Dig.* 509 (2008).

36) H. Zhong, Z. Zhang, H. Xu, C. Qiu, L. M. Peng, Comparison of mobility extraction methods based on field-effect measurements for graphene. *AIP Adv.* **5**, 057136 (2015).

37) B. Huard, N. Stander, J. A. Sulpizio, D. Goldhaber-Gordon, Evidence of the role of contacts on the observed electron-hole asymmetry in graphene. *Phys. Rev. B* **78**, 121402(R) (2008).

38) K. Nagashio, T. Moriyama, R. Ifuku, T. Yamashita, T. Nishimura, A. Toriumi, Is graphene contacting with metal still graphene? *IEDM Tech. Dig.*, 27 (2011).

39) Z. Chen, J. Appenzeller, Gate modulation of graphene contacts - on the scaling of graphene FETs. *Proc. Symp. VLSI Technol.*, 128 (2009).

40) D. B. Farmer, R. Golizadeh-Mojarad, V. Perebeinos, Y. M. Lin, G. S. Tulevski, J. C. Tsang, P. Avouris, Chemical doping and electron-hole conduction asymmetry in graphene devices. *Nano Lett.* **9**, 388 (2009).

41) N. T. Cuong, M. Otani, S. Okada, Semiconducting electronic property of graphene adsorbed on (0001) surfaces of SiO_2. *Phys. Rev. Lett.* **106**, 106801 (2011).

42) Y. J. Kang, J. Kand, K. J. Chang, Electronic structure of graphene and doping effect on SiO_2. *Phys. Rev. B* **78**, 115404 (2008).

43) H. Jippo, T. Ozaki, M. Ohfuchi, First-principles electronic transport calculations of graphene nanoribbons on SiO_2/Si. *Appl. Phys. Express* **7**, 025101 (2014).

44) Y. Zhang, W. Yang, Comment on *Generalized gradient approximation made simple. Phys. Rev. Lett.***80**, 890 (1998).

45) S. Grimme, J. Antony, S. Ehrlich, H. Krieg, Consistent and accurate ab initio parametrization of density functional dispersion correction (DFT-D) for the 94 elements H-Pu. *J. Chem. Phys.* **132**, 154104 (2010).

46) W. Gao, P. Xiao, G. Henkelman, K. M. Liechti, R. Huang, Interfacial adhesion between graphene and silicon dioxide by density functional theory with van der Waals corrections. *J. Phys. D: Appl. Phys.* **47**, 255301 (2014).

47) P. Kumar, A. Kumar, Carrier type modulation in current annealed graphene layers. *Appl. Phys. Lett.* **104**, 083517 (2014).

48) A. Politano, M. Cattelan, D. W. Boukhvalov, D. Campi, A. Cupolillo, S. Agnoli, N. G. Apostol, P. Lacovig, S. Lizzit, D. Farías, G. Chiarello, G. Granozzi, R. Larciprete, Unveiling the mechanisms leading to H_2 production promoted by water decomposition on epitaxial graphene at room temperature. *ACS Nano* **10**, 4543 (2016).

Chapter 6

Single carrier transport in graphene constrictions

In Chapter 4, the graphene devices with the geometrically defined single dot were fabricated. It was suggested that pseudo dots were formed in the dot and also in the constriction parts, resulting in transport characteristics through multiple dots. When fabricated into the simple nanoribbon structure, the current blockade region of Coulomb diamond chareacteristics became an overlapping diamond shape, even though it was processed as thin as 5 nm, suggesting that multiple dots were formed. In Chapter 5, it was revealed from the measurement result of TERS that the doping concentration varied greatly in graphene within the range of 1 μm. In addition, by annealing, it was found that the doping state of the entire graphene can be brought close to neutral.

From the above results, it is conceivable that the chance for dots formation strongly depend on the device dimension and is increased by how long and narrow it is made. Therefore, if graphene is processed to have a narrow and short confinement structure, the single dot could be formed without being largely influenced by edge roughness/local doping effects.

In this chapter, the devices with a short and narrow constriction are studied. Firstly the devices are measured at low temperature without annealing. Then vacuum annealing (with same parameters described in Chapter 5) is performed to investigate the influence of the doping effect for transport properties in the graphene constrictions.

6.1 Design of device structure

The schematic illustration of device studied in this chapter is shown in Fig. 6.1. The constriction devices are fabricated following the process

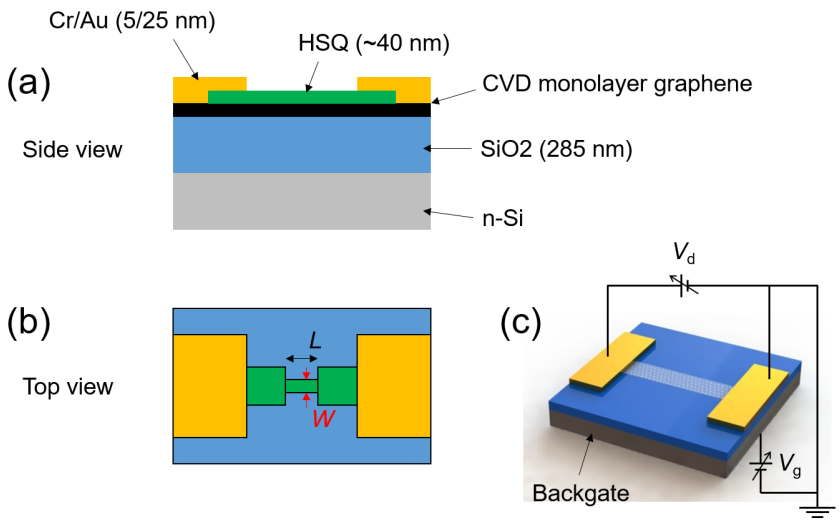

Figure 6.1: Schematic illustration of the constriction device. (a) Side view. HSQ resist is used for a patterning mask. (b) Top view. L and W are the length and width of constriction, respectively. L is designed to 25∼55 nm, W is 25∼100 nm. (c) Measurement configuration. Bias voltage V_{d} is applied to the graphene constriction through the source and drain metal contacts. Back gate voltage V_{g} is applied from the back side doped Si substrate.

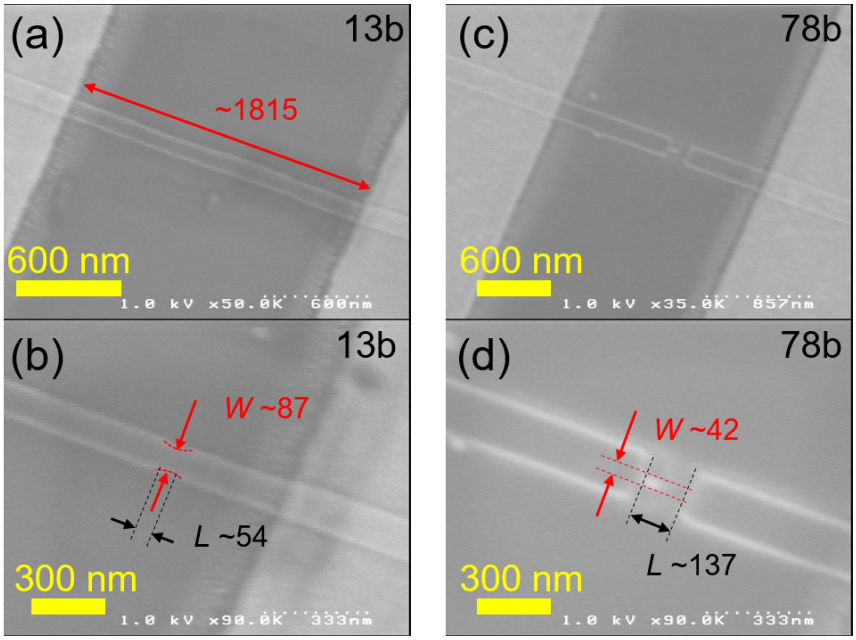

Figure 6.2: SEM images of typical graphene constrictions covered with HSQ. (a),(b) Device named as 13b. L ∼54 nm, W ∼87 nm. (c),(d) Device named as 78b. L ∼137 nm, W ∼42 nm. These images are taken after all of measurements.

described in Chapter 4. Here the CVD graphene is used to investigate the large number of devices for obtaining the trend of change in transport behavior. The CVD graphene sample consisting the SiO_2/Si substrate is purchased from Graphene Platform Co. (Japan). For the etching process, the plasma pressure used for constriction devices is lower than that used in Chapter 4. Hence the lateral etching effect is not expected largely, the visible structure in the SEM images shown in Fig. 6.2 will be referred for analysis.

6.2 Transport properties in grapheen constrictions

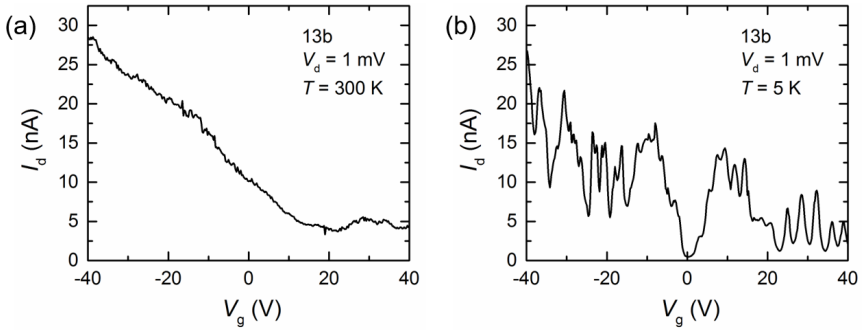

Figure 6.3: I_d-V_g characteristics of graphene constriction device 13b. (a) At room temperature. The current is minimized around V_g ∼22 V. (b) At 5 K. Periodic peaks are observed in V_g = 25∼40 V with the space about 3.6 V.

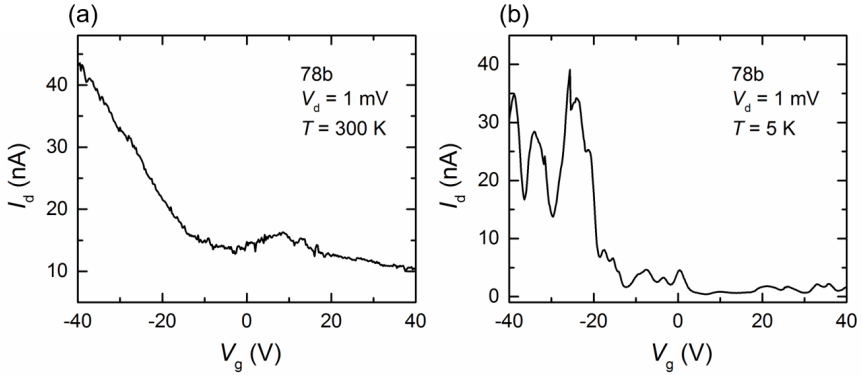

Figure 6.4: I_d-V_g characteristics of graphene constriction device 78b. (a) At room temperature. The current is minimized over V_g >40 V. (b) At 5 K. Current is suppressed in V_g = 5∼40 V.

Figure 6.3 shows the I_d-V_g characteristics of the device 13b. At room temperature, the current is minimized around V_g ∼22 V, suggesting that

the CNP is located around there and graphene is p-doped. This p-doping effect could be due to impurities or water at the interface of graphene-substrate or graphene-HSQ. It has been reported that the HSQ coating on graphene causes n-doping to graphene if the HSQ is not exposed to the EB (EBL process) or plasma (etching process). This doping effect turns into the opposite polarity p-doping to graphene when the chemical structure of HSQ is broken due to the EBL or plasma etching process. Si-H bond in HSQ is firstly broken and Si-O bond in HSQ is broken late, since the bonding energy of Si-H, Si-O are 4.08 eV, 8.95 eV, respectively. Consequently, hydrogen (donor) is escaped and oxygen (acceptor) is adsorbed onto the graphene surface leading to p-doping.

At 5 K, the oscillation behavior is observed in the overall gate voltage range shown in Fig. 6.3. In particular, the periodic peaks could be observed in $V_{\mathrm{g}} = 25{\sim}40$ V. The background current level increasing in the negative gate voltage range seems to follow the ambipolar characteristic at room temperature. At $V_{\mathrm{g}} = 0$ V, the sudden drop of the current is observed, it might be caused by the local neutral point where the locally, heavily doped region in graphene is neutralized. These peaks are stable for various source-drain bias voltage (Fig. 6.5(b)). Furthermore, in the Coulomb diamond characteristic shown in Fig. 6.5(a), the region where current is suppressed forms the lifted diamond shapes. In addition these suppression regions are extended to the similar bias voltage range, *i.e.*, the charging energy is fixed. These features suggest the transport occurred through the single dot. In other gate voltage range, the diamond regions overlap each other and have the different charging energy. This behavior can be considered as the stochastic Coulomb blockade phenomena in the multiple dots system.

From the average peak spacing of periodic peaks, the effective dot size can be extracted by parallel capacitor model;

$$C_{\mathrm{g}} = \frac{e}{\Delta V_{\mathrm{g}}}, \tag{6.1}$$

where the C_{g} is the gate capacitance, e is the elemental charge, and ΔV_{g} is the average peak spacing.[1] Then, the effective area A_{dot} of dot is calculated from $C_{\mathrm{g}} = \epsilon_0 \epsilon_{\mathrm{SiO_2}} A / t_{\mathrm{SiO_2}}$, where ϵ_0 is the vacuum permittivity, $\epsilon_{\mathrm{SiO_2}}$ is the dielectric constant of SiO_2, and $t_{\mathrm{SiO_2}}$ is the thickness of SiO_2. For the device 13b, $\Delta V_{\mathrm{g}} \sim 3.6$ V, $C_{\mathrm{g}} \sim 0.044$ aF, $A_{dot} \sim 0.36{\times}10^{-15}$ m^2 are obtained. The effective area extracted from the measurement is smaller than that extracted from the area of constriction $L \times W = 4.7{\times}10^{-15}$ m^2. This indicates that the single dot could be formed in the constriction region.

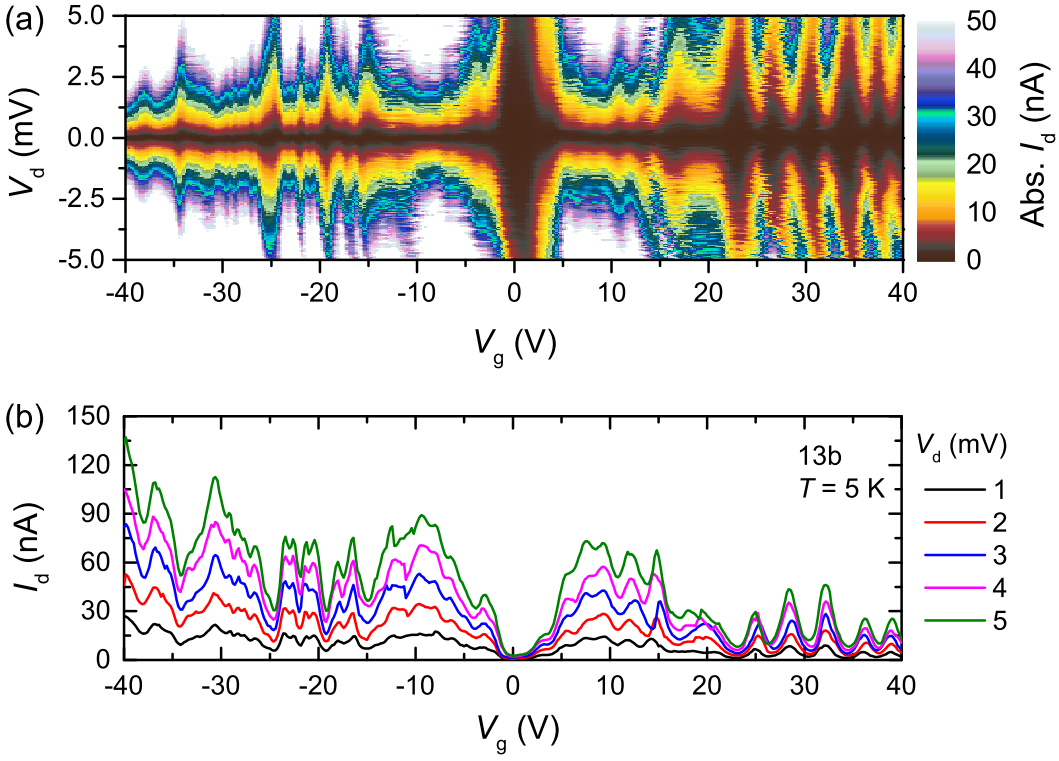

Figure 6.5: Coulomb oscillation and diamond characteristics of constriction device 13b at 5 K. (a) Absolute drain current (Abs. I_d) plot as a function of source-drain bias voltage and gate voltage. Brown colored region corresponds to the blockade region where the drain current is suppressed. Diamond shapes are found in $V_g = 25 \sim 40$ V. (b) I_d-V_g plot at 5 K for various source-drain bias voltage.

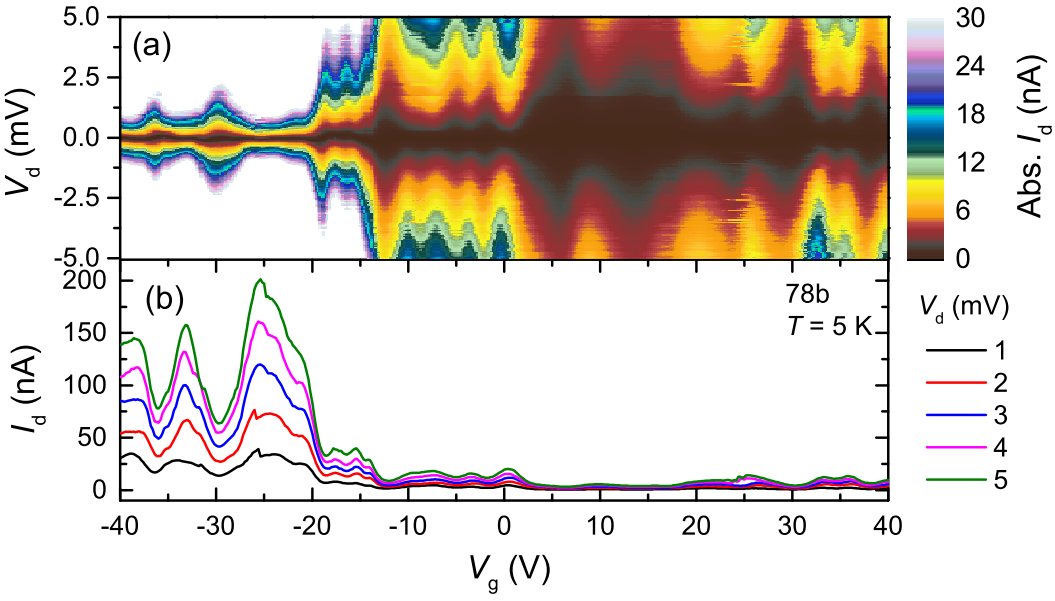

Figure 6.6: Coulomb oscillation and diamond characteristics of constriction device 78b at 5 K. (a) Absolute drain current (Abs. I_{d}) plot as a function of source-drain bias voltage and gate voltage. Brown colored region corresponds to the blockade region where the drain current is suppressed. (b) I_{d}-V_{g} plot at 5 K for various source-drain bias voltage.

For the device 78b, since it is seems that the p-doping in this device is heavier than that of the device 13b (*i.e.*, the CNP is more positive side), the periodic peaks could not be observed (Fig. 6.4). This makes the quantitative analysis difficult.

The temperature dependence of I_{d}-V_{g} characteristics is shown in Fig. 6.7. These measurements are carried out from the lowest temperature. Except the data at 10 K, the I_{d}-V_{g} curve at each temperature have the similar trend, such as high current at the negative gate voltage range. At 10 K, the oscillation behavior is distinctively observed in the overall range and the current level is higher than that at higher temperatures. This can be attributed to the interplay of the single particle level spacing, thermal energy, and the coupling of the energy level to the source/drain electrodes. If the source/drain strongly couple with the ground energy state of the dot, the peak height decreases as increasing temperature. When the source/drain weakly couple with the ground state and strongly couple with the excited state, the peak is enhanced by thermal activation, *i.e.*, thermal energy $k_{\mathrm{B}}T$ is larger than the single particle level spacing.[2]

After these measurements, vacuum annealing is conducted keeping the vacuum condition. As expected, the CNP is shifted to close to $V_{\mathrm{g}} = 0$ V since the charged impurities are removed (Fig. 6.8(a)). At 5 K, the

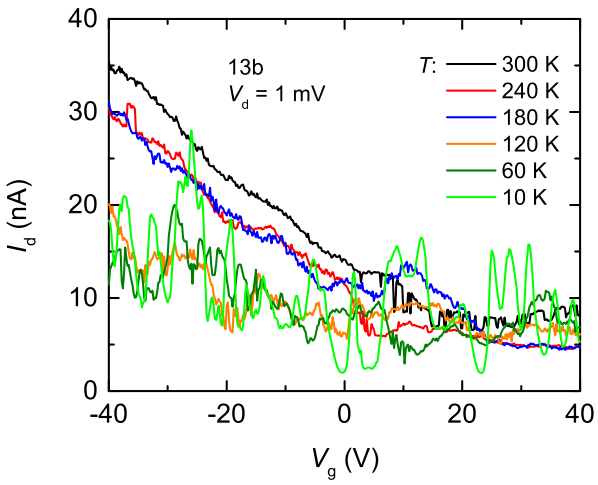

Figure 6.7: Temperature dependence of I_d-V_g characteristics of device 13b.

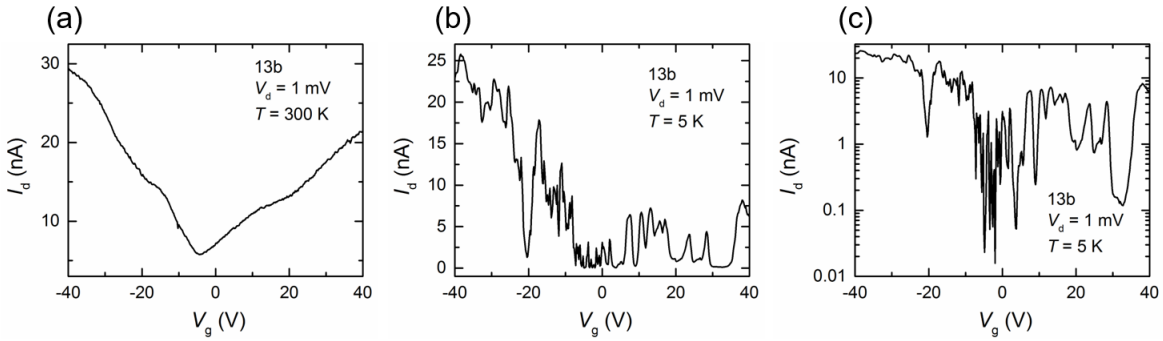

Figure 6.8: I_d-V_g characteristics of graphene constriction device 13b after vacuum annealing. (a) At room temperature. Drain current is minimized at $V_g \sim -4.4$ V. (b) At 5 K. Oscillation behavior is observed in overall range. Current is strongly suppressed in $V_g = -7 \sim 7$ V. (c) Logarithmic scale of (b). Strongly suppressed region is distinctive.

oscillation behavior is observed with the transport gap around $V_g = -7 \sim 7$ V as shown in Fig. 6.8(b) and (c). In this region (at the CNP), the carrier type is expected to be switched between electron and hole. At room temperature the transport between electrons and holes is asymmetric, which can be ascribed to the formation of p-n junction in graphene as a result of local doping.[3–5] Therefore, although the general doping level in the device is near to neutral by vacuum annealing, it seems that local doping can not be fully controlled by vacuum annealing.

As shown in Fig. 6.9, the Coulomb diamond characteristics are measured at 5 K. It is obvious that the current suppression region in the bias voltage direction is larger than that before annealing, for example, $V_g = -7 \sim 7$ V, and $18 \sim 35$ V. In the transport gap ($V_g = -7 \sim 7$ V), the regular diamond shapes are observed in $V_g = -6.8 \sim -4.8$ V, and splitting diamond shape is found in $0.7 \sim 2.8$ V, suggesting the transport via the SQD.[2] Using the periodic peaks in $V_g = -6.8 \sim -4.8$ V, some parameters are extracted like that before annealing. For the device 13b after annealing, ΔV_g ~0.54 V, C_g ~0.296 aF, A_{dot} ~2.4×10^{-15} m^2 are obtained. It should be emphasized that the effective dot area is close to the geometric structure (~4.7×10^{-15} m^2). However, the single dot transport observed around $V_g = 25 \sim 40$ V before annealing disappears after vacuum annealing. This can be attributed to the change in the position of charged impurities, *i.e.*, the location of localized carrier puddle, by annealing.[6]

Table 6.1: Extracted parameters from Coulomb oscillation and diamond characteristics of the device 13b.

Parameters	ΔV_g (V)	C_g (aF)	A_{dot} (10^{-15} m^2)	E_C (meV)	C_Σ (aF)	C_S, C_D (aF)
Before annealing	3.6	0.044	0.36	3.5	45.7	22.8
After annealing	0.54	0.296	2.4	6	26.7	13.2

From the charging energy E_C, the total capacitance C_Σ of the device can be estimated. From the Coulomb diamond plot in Fig. 6.5 and 6.9, the charging energy before and after annealing are ~3.5 meV and ~6 meV, respectively. Then, the total capacitance before and after annealing are extracted to be ~45.7 aF and ~26.7 aF, respectively. The extracted parameters are summarized in Table 6.1. The electrostatic coupling between dot and source/drain electrodes (C_S and C_D) are calculated by assuming $C_\Sigma \approx C_S + C_D + C_g$ and $C_S \approx C_D$. Importantly, the effective dot area

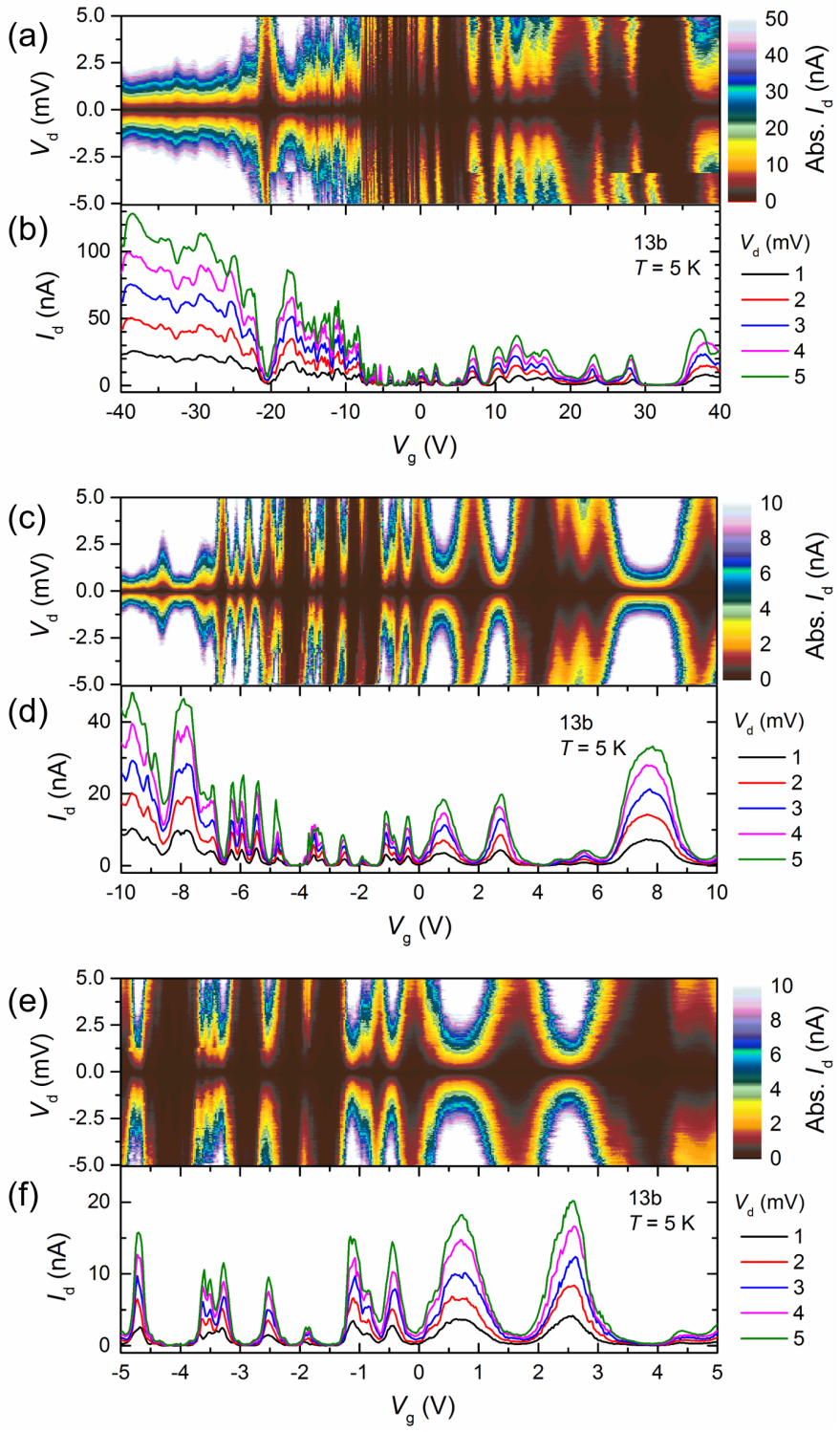

Figure 6.9: Coulomb oscillation and diamond characteristics of the device 13b at 5 K. (a),(b) $V_g = -40 \sim 40$ V. (c),(d) $V_g = -10 \sim 10$ V. (e),(f) $V_g = -5 \sim 5$ V.

for both before and after annealing are smaller than that of the geometric structures of device, inferring that the single dot can be formed in the constriction region. Despite the gate capacitance before annealing is smaller than that after annealing, the total capacitance before annealing is larger than that after. It means that coupling between the source/drain and the dot dominates the total coupling and becomes weak after vacuum annealing as shown in Table 6.1. These peculiar results can be attributed to that the localized area is spanned on the overall constriction region by annealing, and then isolated from the source/drain region since the edge structure at the entrance of the constriction region limits the carrier transport to form the potential barriers. For investigating this assumption and the origin of the potential barriers, it is required to modify the edge structure, such as a taper structure. However, in this chapter the CVD grown graphene was used in order to get the large number of devices as the early investigation.

6.3 Summary

The transport properties of graphene constrictions have been studied. It has been found that the narrow constriction structure leads to less number of pseudo dots compared with a geometrically-defined QD structure or a narrow GNR. Importantly, the transport property through the SQD was observed in the certain gate voltage range. The extracted parameters from the Coulomb diamond characteristics were comparable with the data deduced from the geometric structures. After in-situ vacuum annealing, the stochastic Coulomb blockade behavior was still observed even though the CNP was shifted to nearly zero voltage. This result indicates that by vacuum annealing, local doping is reduced, and however, is not fully controlled. In addition, it has been revealed that local doping plays an important role to form the pseudo dots in graphene nanostructures. As conclusion, the single dot behavior was successfully observed in the graphene nanostructure.

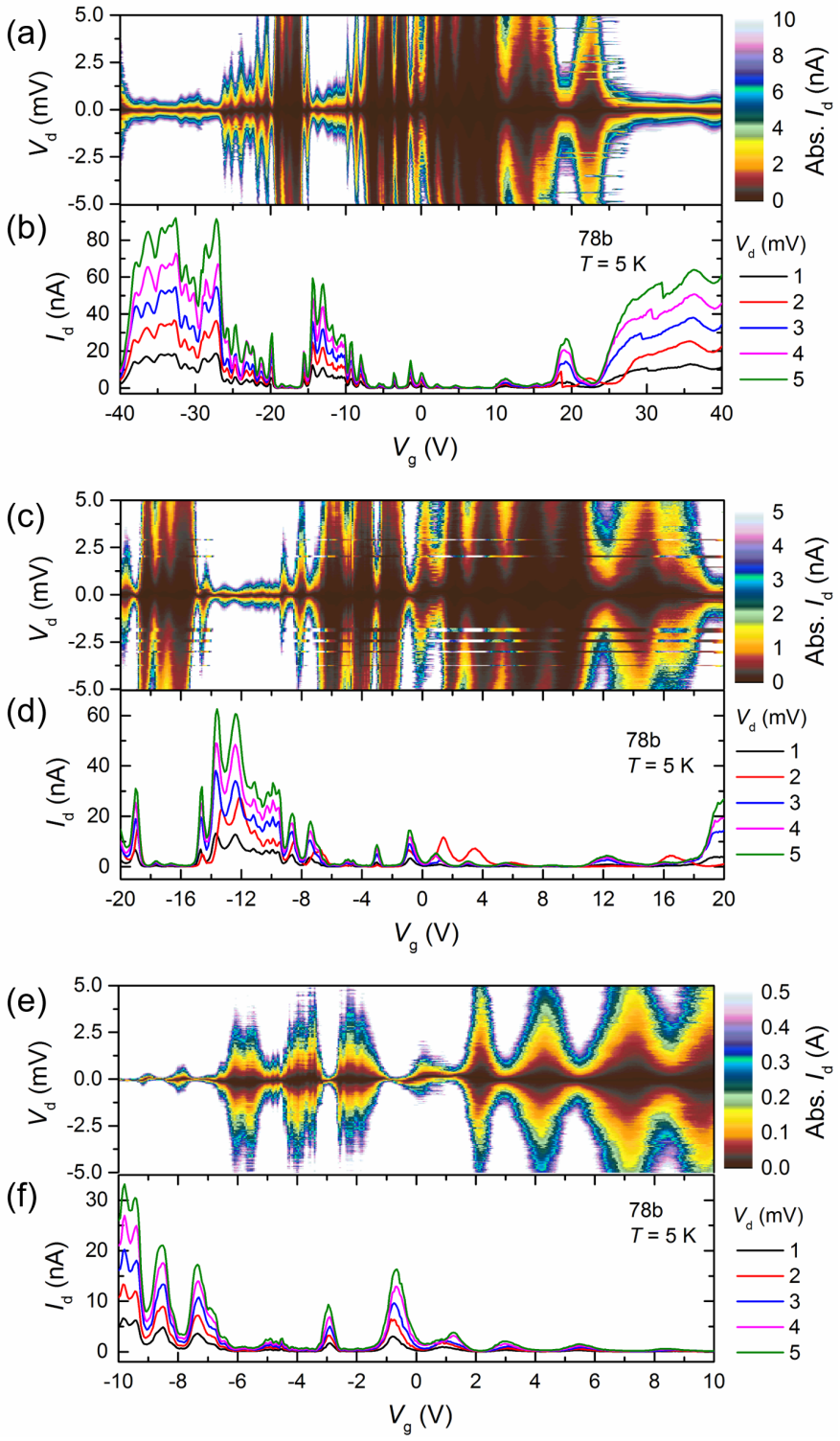

Figure 6.10: Coulomb oscillation and diamond characteristics of the device 13b at 5 K. (a),(b) $V_g = -40 \sim 40$ V. (c),(d) $V_g = -20 \sim 20$ V. (e),(f) $V_g = -10 \sim 10$ V.

References

1) D. Bischoff, F. Libisch, J. Burgdörfer, T. Ihn, K. Ensslin, Characterizing wave functions in graphene nanodevices: Electronic transport through ultrashort graphene constrictions on a boron nitride substrate. *Phys. Rev. B* **90**, 115405 (2014).

2) S. Dröscher, H. Knowles, Y. Meir, K. Ensslin, T. Ihn, Coulomb gap in graphene nanoribbons. *Phys. Rev. B* **84**, 073405 (2011).

3) K. Nagashio, T. Moriyama, R. Ifuku, T. Yamashita, T. Nishimura, A. Toriumi, Is graphene contacting with metal still graphene? *IEDM Tech. Dig.*, 27 (2011).

4) Z. Chen, J. Appenzeller, Gate modulation of graphene contacts - on the scaling of graphene FETs. *Proc. Symp. VLSI Technol.*, 128 (2009).

5) D. B. Farmer, R. Golizadeh-Mojarad, V. Perebeinos, Y. M. Lin, G. S. Tulevski, J. C. Tsang, P. Avouris, Chemical doping and electron-hole conduction asymmetry in graphene devices. *Nano Lett.* **9**, 388 (2009).

6) P. Gallagher, K. Todd, D. Goldhaber-Gordon, Disorder-induced gap behavior in graphene nanoribbons. *Phys. Rev. B* **81**, 115409 (2010).

Chapter 7

Conclusions and future works

In conclusion, as aimed to obtain transport property through a single quantum dot (SQD) in the clean graphene, two approaches have been carried out to overcome the problems on graphene nanostructure devices: (1) investigating the influence of device structure to define a quantum dot in graphene with taking account for extrinsic disturbances, and (2) reducing the impact from charged impurities to graphene (in other words, developing the method to clean graphene devices).

Consequently, the achievements can be considered to be five contributions, and however, all results aimed for the SQD formation in graphene. (i) The effects of doping induced by charged impurities on carrier transport properties in graphene devices (FETs, nanoribbons, geometrically-defined QDs) have been clarified. (ii) The novel device fabrication technique that etching from the side by high pressure plasma using the HSQ as the protecting mask has been proposed, which allow to easily fabricate GNRs with high aspect ratio. It has revealed that pseudo multiple quantum dots in series are formed in the GNR even the width of GNR is narrower than the critical length scale of carrier puddles. It can be deduced from the results of (i) and (ii) that the long length leads to the formation of multiple QDs since if the localized charge behaves as a pseudo QD its shape is no longer a circle, the only requirement seems to be the sufficient area for the single localized puddle. Therefore, a nano-constriction that is the GNR with the short length can be considered as the suitable structure for the SQD formation. (iii) The detection of the spatially-localized doping concentration difference (carrier localization) in graphene by TERS has succeeded for the first time, and it has been clarified that local doping on nanoscale is introduced in graphene during the device fabrication process. This result leads to locally evaluate doping and stress in graphene at the nanoscale,

and it will be greatly useful for future development of nanoscale graphene devices. (iv) The method for reducing the effect of charge impurities (*i.e.*, doping effects) by annealing is proposed and the detailed mechanism for the change in the transport properties clarified, and hence, it is realized that the CNP can be controlled by the annealing treatment. This method can make graphene devices such as the gas sensor refresh the condition without irreversible change. (v) The SQD behavior in graphene nano-constriction has been observed without lateral side gate control, suggesting that the nano-constriction structure in this study might be the minimum required component to form the SQD in graphene. Graphene constriction, that is, the most basic building block in graphene quantum devices, and therefore, will contribute greatly to the development of graphene quantum devices, which is highly expected in both academic interests and industrial applications in the future.

In Chapter 7, the CVD grown graphene was used in order to get the large number of devices as the early investigation. As the future work, the exfoliated graphene-based constriction devices should be investigated since the transport properties of CVD graphene and exfoliated graphene must be different due to the influence of grain boundary. The constriction devices based on the exfoliated single crystal graphene should be studied to investigate the effect of edge roughness, local doping and annealing effect for the inherent properties of graphene in the future. Furthermore, the origin of tunnel barriers has not been fully understood. One of way to investigate this assumption is the first principle calculation with the model having the different edge structure at the entrance to the constriction region.

Publication list

Journals

1. T. Iwasaki, J. Sun, N. Kanetake, T. Chikuba, M. Akabori, M. Muruganathan, H. Mizuta, Hydrogen intercalation: An approach to eliminate silicon dioxide substrate doping to graphene. *Appl. Phys. Express* **8**, 015101 (2015).

2. T. Iwasaki, M. Muruganathan, H. Mizuta, Fabrication and characterization of graphene single carrier transistor. *IEICE Tech. Rep.* **114**, 69 (2015).

3. J. Sun, T. Iwasaki, M. Muruganathan, H. Mizuta, Lateral plasma etching enhanced on/off ratio in graphene nanoribbon field-effect transistor. *Appl. Phys. Lett.* **106**, 033509 (2015).

4. T. Iwasaki, T. Zelai, S. Ye, H. M. H. Chong, Y. Tsuchiya, H. Mizuta, Local hole doping concentration modulation on graphene probed by tip-enhanced Raman spectroscopy. *Carbon* **111**, 67 (2017).

5. T. Iwasaki, M. Muruganathan, M. E. Schmidt, H. Mizuta, Partial hydrogenation induced interaction in a graphene-SiO_2 interface: Irreversible modulation of device characteristics. *Nanoscale* **9**, 1662 (2017).

International conferences

1. N. Kalhor, S. Hang, T. Iwasaki, Z. Moktadir, S. Boden, M. Manoharan, H. Mizuta, Sharp edged sub-25 nm graphene single-electron devices fabrication by Helium ion beam milling technique. *JSAP-MRS Joint Symposia*, 17p-PM1-16, Kyoto, Japan, 16-20 Sep. (2013).

2. H. Mizuta, Z. Motadir, S. Hang, N. Kalhor, J. Reynolds, T. Iwasaki, M. Schmidt, M. Muruganathan, Helium ion beam based novel fabrica-

tion of downscaled graphene nanodevices. *The 15th Takayanagi Kenjiro Memorial Symposium*, 3-2, Shizuoka, Japan, 12-13 Nov. (2013).

3. T. Iwasaki, M. Muruganathan, H. Mizuta, Bilayer graphene single carrier transistors. *IEEE Silicon Nanoelectronics Workshop (SNW)*, 5-3, Hawaii, USA, 8-9 June (2014).

4. T. Iwasaki, M. Muruganathan, H. Mizuta, Graphene single carrier transistors. *The 9th India-Japan bilateral conference on Advanced Materials Science and Engineering (BICON2014)*, Jaipur, India, 12-17 Oct. (2014).

5. H. Mizuta, T. Iwasaki, N. Kalhor, J. Sun, M. Muruganathan, Downscaled graphene nanodevices: helium ion beam based nanofabrication, graphene single-carrier transistors (GSCTs) and nano-electromechanical (GNEM) switches (invited talk). *IEEE 12th International Conference on Solid-State and Integrated Circuit Technology (ICSICT)*, Guilin, China, 28-31 Oct. (2014).

6. H. Mizuta, T. Iwasaki, N. Kalhor, J. Sun, M. Muruganathan, Downscaled graphene nanoelectronic and nano-electro-mechanical (NEM) devices (invited talk). *QNERC Workshop on Nano Devices and Materials*, Tokyo, Japan, 4th Nov. (2014).

7. J. Sun, T. Iwasaki, M. Muruganathan, H. Mizuta, High aspect ratio graphene nanoribbon patterned using hydrogen-silsesquioxane semi-soft mask. *The 27th International Microprocesses and Nanotechnology Conference (MNC)*, 7P-11-10, Fukuoka, Japan, 4-7 Nov. (2014).

8. H. Mizuta, T. Iwasaki, N. Kalhor, S. Hang, Z. Moktadir, J. Sun, M. Muruganathan, Fabrication and characterization of downscaled graphene nanoelectronic devices and NEMS (invited talk). *The 1st Malaysia-Japan Joint Symposium on Nanotechnology 2014*, Kuala Lumpur, Malaysia, 10-12 Dec. (2014).

9. T. Iwasaki, M. Muruganathan, H. Mizuta, Impacts of channel constriction dimensions of graphene single-carrier transistors on the Coulomb diamond characteristics. *IEEE Silicon Nanoelectronics Workshop (SNW)*, 5-5, Kyoto, Japan, 14-15 June (2015).

10. T. Iwasaki, M. Muruganathan, H. Mizuta, Impacts of channel constriction dimensions of graphene single-carrier transistors on the Coulomb

diamond characteristics. *2015 UK-Japan Si Nanoelectronics Nanotechnology Symposium in Southampton*, 20, Southampton, UK, 9-10 July (2015).

11. A. Khalid, J. Sampe, B. Y. Majlis, M. A. Mohamed, T. Chikuba, T. Iwasaki, H. Mizuta, Towards high performance graphene nanoribbon transistors (GNR-FETs). *2015 IEEE Regional Symposium on Micro and Nanoelectronics*, Kuala Terengganu, Malaysia, 19-21 Aug. (2015).

12. M. A. Mohamed, A. Khalid, B. Y. Majlis, T. Iwasaki, M. Muruganathan, H. Mizuta, Characterization of trilayer graphene field-effect transistors (invited talk). *3rd Malaysia Graphene and Carbon Nanotube Workshop*, Kuala Lumpur, Malaysia, 19-20 Oct. (2015).

13. H. Mizuta, T. Iwasaki, S. Suzuki, A. Hammam, J. Sun, M. E. Schmidt, M. Muruganathan, Downscaled graphene nanoelectronics and NEM devices for advanced applications (invited talk). *The 2nd Malaysia-Japan Joint Symposium on Nanotechnology*, Ishikawa, Japan, 10-12 Nov. (2015).

14. H. Mizuta, T. Iwasaki, S. Suzuki, A. Hammam, J. Sun, M. E. Schmidt, M. Muruganathan, Recent progress of graphene nanoelectronic and NEM device technologies for advanced applications (invited talk). *Perspectives in Nano Information Processing an international conference and workshop 2015*, Cambridge, UK, 14-16 Dec. (2015).

15. H. Mizuta, T. Iwasaki, S. Suzuki, O. Takechi, A. Hammam, J. Sun, M. E. Schmidt, M. Manoharan, Downscaled graphene devices for low-power nanoelectronics and advanced sensing (invited talk). *IISc-JAIST Joint Workshop on. Functional Inorganic and Organic Materials*, Ishikawa, Japan, 7-8 Mar. (2016).

16. Z. Tan, T. Iwasaki, L. Boodhoo, H. Mizuta, H. M. H. Chong, Fabrication and characterization of silicon notched nanowire FETs with selective channel dopants. *29th International Microprocesses and Nanotechnology Conference (MNC)*, Kyoto, Japan, 8-11 Nov. (2016).

Domestic conferences

1. N. Kalhor, S. Hang, T. Iwasaki, Z. Moktadir, S. Boden, M. Muruganathan, H. Mizuta, Fabrication of extremely-scaled graphene single-

electron transistors by using He ion beam milling technology. *The 60th Japan Society of Applied Physics (JSAP) Spring Meeting*, 27p-G12-43, Kanagawa, 27-30 Mar. (2013).

2. T. Iwasaki, M. Muruganathan, H. Mizuta, Characterization of bilayer graphene single-electron transistors. *The 61st JSAP Spring Meeting*, 20a-E2-7, Kanagawa, 17-20 Mar. (2014).

3. H. Mizuta, T. Iwasaki, N. Kalhor, S. Hang, Z. Moktadir, J. Sun, M. Muruganathan, グラフェン超微細デバイスの作製と応用 (invited talk). 第 59 回 CVD 研究会, Aichi, 27-28 Aug. (2014).

4. T. Iwasaki, M. Muruganathan, H. Mizuta, Fabrication and characterization of graphene single carrier transistor. 電子デバイス研究会, Hokkaido, 5-6 Feb. (2015).

5. T. Iwasaki, J. Sun, N. Kanetake, T. Chikuba, M. Akabori, M. Muruganathan, H. Mizuta, Elimination of silicon dioxide substrate doping to graphene nanoribbon FET by hydrogen intercalation. *The 62nd JSAP Spring Meeting*, 11a-P6-53, Kanagawa, 11-14 Mar. (2015).

6. K. Inoue, T. Iwasaki, M. Muruganathan, H. Mizuta, Fabrication and characterization of graphene quantum dot by using hydrogen silsesquioxane. *The 76th JSAP Autumn Meeting*, 15a-2T-4, Aichi, 13-16 Sep. (2015).

7. H. Mizuta, O. Takechi, T. Iwasaki, M. Schmidt, J. Sun, Y. Tsuchiya, S. Boden, M. Koyano, M. Muruganathan, NEMS 技術とフォノンエンジニアリング (invited talk). 応用電子物性分科会研究例会「フォノンエンジニアリングの現状と展望」, Ishikawa, 25th Nov. (2015).

8. W. Wang, T. Iwasaki, J. Sun, M. Muruganathan, H. Mizuta, Hydrogen annealing effect on graphene nanoribbon FET covered by silicon dioxide passivation layer. *The 63rd JSAP Spring Meeting*, 20a-P4-46, Tokyo, 19-22 Mar. (2016).

9. T. Iwasaki, T. Zelai, S. Ye, H. M. H. Chong, Y. Tsuchiya, H. Mizuta, Local doping concentration modulation on graphene probed by tip-enhanced Raman spectroscopy. *The 77th JSAP Autumn Meeting*, 13p-P5-43, Niigata, 13-16 Sep. (2016).

10. T. Iwasaki, M. Muruganathan, M. E. Schmidt, H. Mizuta, Annealing effects on transport properties of trilayer graphene field-effect transistors. *The 77th JSAP Autumn Meeting*, 15p-A33-5, Niigata, 13-16 Sep. (2016).

11. T. Iwasaki, M. Muruganathan, H. Mizuta, Hysteresis behavior in trilayer graphene. *The 64th JSAP Spring Meeting*, 15a-B6-3, Kanagawa, 14-17 Mar. (2017).

Acknowledgements

For completing this research, I thank to a great number of people for their kind help. There is no reason for I can now write this thesis, except everyone's help. Here I would like to express my appreciation to them.

First of all, I would like to express my sincere gratitude to Professor Hiroshi Mizuta, at Department of Energy and Environment, School of Materials Science in Japan Advanced Institute of Science and Technology (JAIST), who is the supervisor of my PhD project. Professor Mizuta gave me a very interesting research theme, a blessed research environment, and the opportunity to study in the United Kingdom for a year. He taught me not only the scientific technical skills (i.e., professional writing, presentation at a conference meeting, data analysis from a broad perspective), and also mentality and humanity (i.e., thinking for student education as a teacher, attitude as an independent researcher). When the study was not going well, he helped me, sometimes kindly, and sometime strictly. Since this balanced teaching, I could continue and complete the project tasks. For total five years including the master course, he trusted and guided me politely, that I have never experienced. I sincerely express my respectful gratitude to Prof. Mizuta from the bottom of my heart.

I would like to heartily thank Assistant Professor Manoharan Muruganathan in Mizuta Laboratory, for giving me guidance on concrete experimental and analytical techniques etc. He was always a first person who checked experiment data and a manuscript. Hence, he is the most familiar teacher for me. He cultivated my basic research skills and technical English ability, which is plenty for growing up as an independent researcher. When I asked him about any problems in research, he thoughtfully considered it from the point of view same as me. As we also discussed something unrelated to research, I learned an English skill, humanity and international thinking from him. I deeply appreciate Assis. Prof. Muruganathan from the bottom of my heart for giving priceless experiences.

I am very grateful to Dr. Harold Chong, a visiting associate professor in Mizuta Lab. and a senior lecturer at Faculty of Physical Sciences and Engineering in University of Southampton (UOS). He supervised me when I studied at UOS from July 2015 to June 2016. I learned the methods to use Raman spectroscopy, AFM, TERS systems, and to analyze experimental data, and to organize the manuscript from the point of view in

engineering. I then could consider worth and significance in my own research. Even though he was always so busy, he often invited me lunch and discussed the progress of research and life in UK. I really thank Dr. Chong from the bottom of my heart for his very polite guidance.

I would like to thank Professor Hideyuki Murata at Department of Applied Physics, School of Materials Science in JAIST. He was assigned as a second supervisor for my PhD project. Though I often inconvenienced him on administrative documents, he kindly helped me every time. In addition, he gave me advice on the subtheme thesis.

I would like to deeply thank Professor Shinichi Saito at Faculty of Physical Sciences and Engineering in SOU. We deeply discussed the significance and prospect of my research and related research field in future. In addition, he invited me to his group discussion every week and gave me the opportunity to present my research in that meeting, which was the great experience. Moreover, he kindly counseled me not only on my PhD project, but also on my future in academia.

I am very grateful to Dr. Yoshishige Tsuchiya, a senior lecturer at Faculty of Physical Sciences and Engineering in UOS. He gave me a lot of advice on TERS and Raman scattering. In addition, he taught me what is important to continue the research theme fusing both material characterization and device application. I also learned a lot including the significance of TERS in the world. Despite the fact that he was always so busy, he invited me to the regular meeting every meek and kindly gave me advice on my subtheme project in Southampton.

I would like to deeply appreciate Associate Professor Tetsuo Kodera at School of Engineering, Department of Electrical and Electronic Engineering in Tokyo Institute of Technology. He kindly did an external examiner of my preliminary and final defense. We often discussed the research related to quantum transport at a conference, and I learned a lot of expertise, such as technique for transport measurement at a low temperature, device design etc. He gave me advice very carefully even for the very primitive questions.

I am grateful to Professor Tatsuya Shimoda at Department of Energy and Environment, and Professor Eisuke Tokumitsu at Department of Applied Physics, and Associate Professor Yukiko Takamura (assigned as one of advisor in JAIST for my subtheme) at Department of Applied Physics, School of Materials Science in JAIST. They gave me

helpful advice and comments with very deep insight in the preliminary defense. Additionally, Assoc. Prof. Takamura guided me on the subtheme project.

I would like to thank Associate Professor Masashi Akabori at Department of Applied Physics, Center for Nano Materials Technology (CNMT) in JAIST. He gave me a lot of advice about the experiment for a cryogenic low temperature (e.g., cryostat, dilution refrigerator) and the method to use the equipment in the clean room. Without his supports, the samples in this thesis were not satisfactorily fabricated. I deeply appreciate Assoc. Prof. Akabori for teaching me basic and applied technique.

I am very grateful to Professor Mikio Koyano at Department of Energy and Environment, School of Materials Science in JAIST, for training me on Raman spectroscopy equipment. He taught me not only about own research but also wide range topics. In particular, I learned from him many things involved with education. I thank Prof. Koyano very much for his careful guidance.

I would like to sincerely thank Dr. Marek Schmidt, a postdoctoral researcher in Mizuta Lab. He taught me a lot of high-level expertise consisting of sample preparation, mechanism and operation method of experimental apparatus, advanced software, etc. He also kindly corrected my English in a manuscript and a presentation with the very proficient skill. Furthermore, I learned from him that careful handle in experiment directly leads to a good result. I deeply appreciate Dr. Schmidt to teach me the importance of attitude for research.

I am dearly grateful to Dr. Jian Sun, a postdoctoral researcher in Mizuta Laboratory (current: RIKEN). I learned a lot from him about the basic format of scientific writing, and logical layout in a scientific paper, and how to proceed with the experiment plan. Especially, his plan from the beginning of the experiment to the end of writing paper was incredible, which is the great reference for me. Even in a short period, I was honored and lucky to have done research with him. I thank Dr. Sun for his valuable guidance and advice.

I thank Mr. Ichiro Kimura, Mr. Nobuaki Itou, Mr. Munenori Uno and Mr. Yuji Nakabayashi at CNMT in JAIST, for managing liquid helium, teaching me how to use AFM, and designing, creating, modifying our experimental equipment, respectively.

I would like to appreciate Mrs. Reiko Seki for her excellent management on expenses for my business trip and on many administrative documents. I also cordially thank doctoral researchers, students, and visitors in Mizuta Laboratory, students, as follows: Dr. Zakaria Moktadir (current: TOSHIBA Cambridge Research Laboratory), Dr. Faezeh Arab Hassani, Dr. Le The Anh (current: RIKEN), Dr. Huynh Van Ngoc, Mr. Shinri Inoue (current: Hitachi, Ltd.), Keiichi Kitagawa (current: FUJITSU Telecom Networks Ltd.), Tomonori Imamura (current: YKK AP Inc.), Mr. Ahmed Hammam, Mr. Wenzhen Wang, Mr. Nozomu Kanetake (current: Tokyo Electron Ltd.), Mr. Takuo Chikuba (current: Miharu Communication Inc.), Mr. Dinh Hiep Duong (current: Hai Lab. in Tokyo Institute of Technology), Mr. Keisuke Inoue (current: TOSHIBA Co.), Mr. Shinya Iwashita (current: NHK Spring Co., Ltd.), Mr. Outa Takechi (current: Hitachi High-Technologies Co.), Mr. Shunei Suzuki, Mr. Kulothungan Jothiramalingam, Mr. Zhongwang Wang, Mr. Daiki Kato, Mr. Teruhisa Kanzaki, Mr. Fumihiro Seto, Mr. Nikolaos Matthaiakakis (UOS), Mr. Kouki Inoue, Mr. Kazunari Sasaki, Mr. Sho Taniuchi, Mr. Shu Nakamura, Mr. Mohit Dalal, Mr. Afsal Kareekunnan, Dr. Shuojin Hang (current: ARM Holdings plc), Dr. Liam Boodhoo (current: UOS), Mr. Jamie Reynolds (UOS), Mr. Ryohei Miyazaki (special research student in Mizuta Lab. and at Awano Lab. in Keio University), Ms. Aiko Kunisaki (special research student in Mizuta Lab. and Hatano-Kodera Lab. in Tokyo Institute of Technology), Mr. Ryo Maekura (National Institute of Technology, Okinawa College), Mr. Dinesh Godara (Indian Institutes of Technology Kanpur), Aishah Khalid (University Kebangsaan Malaysia), Mr. Aaron Teo Yii How (UOS Malaysia), Ms. Rashmi Shende (Indian Institutes of Technology Madras), Mr. Zulkefli Mohd Amir (University Kebangsaan Malaysia), and others.

I would like to express my appreciation to many people who took care of me during my study at UOS. I am grateful to Assistant Professor Takahiro Tsukamoto at Suda Lab., Graduate School of Engineering in Tokyo University of Agriculture and Technology, for discussing the configuration of TERS. I also deeply thank to Dr. Sheng Ye and Mrs. Taharh Zelai at Nanoelectronics and Nanotechnology Group in UOS, for training me on Kelvin probe force Microscope, AFM, Raman, and TERS systems. Dr. Stuart Boden a senior lecturer at Nanoelectronics and Nanotechnology Group in UOS, and Ms. Xiaoqing Shi frequently helped me for operation of helium ion microscope. Mr. Zhencheng Tan, Mr. Christoph Riedel, Mr. Benjamin Lowe, Ms. Sahar Mirzaei, Mr. Fayong Liu, Ms. Katarzyna Grabska, Mr. Abdulraham Al-Attili, Mr. Xingzhao Yan, Mr. Chirenjeevi Krishnan, Mr. Martin Ebert, Dr. Taha Masaud, Dr. Sun Kai, Dr. Swe Oo, Dr. Mehdi Banakar, Mr. Zuo Li, and other Nanoelectronics and Nanotechnology Group members

helped me a lot, so I could not complete the tasks in Southampton without their help. Dr. Kian Kiang, Mr. Peter Ayliffe, and other technical staff in UOS carefully taught me about the operation of many equipment in the clean room. I would like to thank my roommates in the share house, Mr. Zilong Wang, Ms. Wanying Xing, Ms. Jingbing Zhao, Mr. Yujun Feng for sharing the pleasant life, and Mr. and Mrs. Laybourne for taking care of us as landlords.

I am grateful to Ms. Mariko Kuki and Ms. Tomoko Yoshida at International Student Section, Student Affairs Department in JAIST for their kind assistance on the study abroad. I also warmly thank Mr. Satoshi Kawai, Ms. Nobue Kuramoto and Ms. Yumiko Mita at Competitive Research Fund Section in JAIST for taking care of KAKENHI and the administrative documents for JSPS research follow. Additionally, I appreciate other staffs in JAIST and UOS office.

I would like to express my gratitude to my friends who have studied since the master course together: Mr. Ryo Ito, Mr. Toshimasa Ui, Mr. Mahiro Shirotori, and Mr. Ko Sugahara. I also like to thank Mr. Kohei Aoyagi (current: Siemens AG) and other graduated colleagues. Without friendly competition with them and encouragement from them, it was impossible to continue research and life in JAIST.

Finally, I sincerely appreciate my family from the bottom of my heart for helping me with continuous economic and mental support.

This research could not be completed without support from everyone. Many thanks.

Takuya Iwasaki

Mizuta laboratory
School of Materials Science
Japan Advanced Institute of Science and Technology
23rd March 2017

謝辞

本研究を遂行するにあたり，非常に多くの方々にお世話になりました．このように博士学位論文を書き上げることができるのは，皆様のご助力があったからに他なりません．この場を借りて皆様に感謝の意を表します．

第一に，主指導教員である北陸先端科学技術大学院大学(JAIST)，先端科学技術研究科，環境・エネルギー領域の水田博教授に深く感謝申し上げます．水田教授には大変興味深い研究テーマ，恵まれた研究環境，さらには 1 年間のイギリス留学の機会まで与えていただきました．論文執筆・会議での研究発表・広い視野からのデータ解析等の専門的な技術のみならず，学生教育に関する考え方・独立した研究者としての姿勢・心構えなど，精神面・人間性においても多くのことを学ばせていただき，人として大切なことを多岐にわたりご指導いただきました．研究が行き詰まり困難に感じることもありましたが，時に優しく時に厳しい抑揚のある水田先生の指導のおかげで，こうして最後まで研究をやり通すことができました．博士前期課程も含めて計 5 年間私のことを最後まで信頼し，終始辛抱強くご指導いただきましたことに深く敬意を表し，心からお礼申し上げます．

水田研究室のマノハラン・ムルガナタン助教には具体的な実験・解析手法等をご指導いただきました．実験データや論文の原稿が書きあげたとき，いつも最初にご指導くださったのはマノハラン助教であり，私にとって最も身近な教育者でした．研究者として自立するための基礎研究能力や英語能力をご教授いただきました．研究に関する悩みを相談させていただいた際も，常に同じ立場になって真剣に考えてくださり，親身に対応していただきました．また，研究と関係ない雑談を頻繁にさせていただき，英語能力・国際的な考え方など，多くのことを学ばせていただきました．かけがえのない貴重な経験をさせていただいたことに深く敬意を表し，心からお礼申し上げます．

サウサンプトン大学, Faculty of Physical Sciences and Engineering，シニアレクチャラー兼 JAIST 水田研究室客員准教授であるハロルド・チョン博士には，私が 2015 年 7 月から 2016 年 6 月までの 1 年間サウサンプトン大学に留学していた際に，スーパーバイザーとしてご指導していただきました．ハロルド博士からはラマン分光, AFM, TERS 装置の使用方法や研究の進め方，データ解析や論文構成の工学的な視点からのご指導を授かり，自分の研究の意義・価値をより深く考察することができました．大変ご多忙の中でも頻繁に食事にお誘いいただき，

研究・生活に関して様々なことを相談させていただきました．丁寧なご指導に深く敬意を表し，心からお礼申し上げます．

副指導教員である JAIST, 応用物理学領域の村田英幸教授には，事務書類の手続きでご迷惑をお掛けしてしまうことも多々ありましたが，毎回丁寧に対応していただきました．また, TERS に関連する研究をまとめた副テーマ論文を完成させる過程において，有力なご助言をいただきました．深く感謝申し上げます．

サウサンプトン大学, Faculty of Physical Sciences and Engineering の斎藤真一教授には，本研究の意義・将来性，今後における関連研究の将来的な見通し等，大変多くのことを議論させていただきました．毎週の研究発表会へのお誘い，さらに研究発表の機会を与えていただきました．博士後期課程のことだけではなく，卒業後のことまで気に掛けていただき，様々なご助言をいただきました．多岐にわたりご指導いただきましたことに心からお礼申し上げます．

サウサンプトン大学, Faculty of Physical Sciences and Engineering, シニアレクチャラーの土屋良重博士には, TERS やラマン散乱に関して大変有意義な議論をさせていただきました．材料・物性評価とデバイス応用を融合させた研究を続けていく上で大切なことや, TERS 技術の世界的な位置づけ等，貴重なお話をしていただき大変勉強させていただきました．ご多忙の中，定期的にミーティングにお誘いいただき，私のサウサンプトンでの研究方針をご教授いただきました．深く敬意を表し，心からお礼申し上げます．

外部博士学位論文審査員である東京工業大学，工学院電気電子系の小寺哲夫准教授に深く感謝申し上げます．応用物理学会をはじめとする会議において，関連分野の研究に関して議論させていただき，測定技術やデバイス設計など非常に多くの専門知識を学ばせていただきました．初歩的な質問に対しても，丁寧にご助言をいただきました．心からお礼申し上げます．

博士学位論文審査委員である JAIST，環境・エネルギー領域の下田達也教授，応用物理学領域の徳光永輔教授，高村由起子准教授には本論文を完成させる過程において，予備審査を通して大変有力なご助言をいただきました．また，高村由紀子准教授には TERS に副テーマ論文を完成させる過程において，有力なご助言をいただきました．皆様に深く感謝申し上げます．

JAIST，環境・エネルギー領域の小矢野幹夫教授には，同研究室のラマン分光装

置を頻繁にご使用させていただきました．研究のみならず，様々な場面でお話しさせていただく機会が多く，幅広い知識を学ばせていただきました．特に，教育者の姿勢や学生指導に関して多くのことを学ばせていただきました．丁寧なご指導に深く敬意を表し，心からお礼申し上げます．

JAIST，応用物理学領域，ナノマテリアルテクノロジーセンターの赤堀誠志准教授には，クリーンルームの設備利用方法やクライオスタット，希釈冷凍機などの低温実験装置に関して多大なご助言・ご指導賜りました．赤堀准教授のご支援が無ければ，本研究におけるサンプル・デバイスは満足に完成しませんでした．技術的な基礎・応用知識をご教授いただきましたことに深く敬意を表し，心からお礼申し上げます．

水田研究室のマレク・シュミット博士研究員には，サンプル作製技術，実験装置の動作方法・原理，高度なソフトウェアの使用方法など，非常に高度な専門技術に関してご指導いただきました．論文原稿の細かい訂正，適切な表現等，英語能力に関しても多大なご助言をいただきました．また，実験を丁寧に進めることが良い結果に繋がることを学ばせていただきました．研究に対する大切な姿勢をご指導いただきましたことに深く敬意を表し，心からお礼申し上げます．

旧水田研究室，博士研究員のジアン・スン博士(現:理化学研究所)には，学術論文の基本的な体裁・論理構成や，実験計画の進め方などを多くのことを学ばせていただきました．特に実験開始から論文原稿完成までの段取りが素晴らしく，とても参考にさせていただきました．短い期間でしたが共に研究ができたことを大変光栄・幸運に思います．有益なご指導・ご助言いただき，心からお礼申し上げます．

JAIST，ナノマテリアルテクノロジーセンター技術職員の木村一郎氏，伊藤暢晃氏，宇野宗則氏，仲林裕司氏には，実験装置の利用方法のご指導，実験機器の設計・作製・改造と多岐にわたりお世話になりました．深く感謝申し上げます．

水田研究室の研究補助員の関玲子氏には，出張や各種手続きで多大にご助力いただきました．同研究室の博士研究員の皆様，学生の皆様，インターンシップで短期訪問研究をされた日本人・外国人の方々には，研究生活の様々な場面でご助言・ご支援いただきました．ザカリア・モクタディール博士(現:東芝ケンブリッジ研究所)，ファエゼ・アラブ・ハサーニ博士，ル・テ・アン博士，フィン・ヴァン・ゴク博士，井上真理氏(現:日立製作所)，北川景一様(現:富士通テレコムネッ

トワークス), 今村知典氏(現:YKK AP), アーメド・ハマム氏, ウェンジェン・ワン氏, 兼竹望氏(現:東京エレクトロン), 筑葉拓生氏(現:ミハル通信), ディン・ヒエプ・ドウオング氏(現:東京工業大学, Hai 研究室), 井上佳祐氏(現:東芝), 岩下晋也氏(現:日本発条), 武市旺太氏(現:日立ハイテクノロジーズ), 鈴木俊英氏, クロトゥンガン・ジョティラマリンガム氏, 王衆望氏, 加藤大貴氏, 神崎晃悠氏, 瀬戸文博氏, ニコラオス・マタイアカキス氏(サウサンプトン大学), 井上顧基氏, 佐々木和成氏, 谷内翔氏, 中村周氏, モヒート・ダラル氏, アフサル・カリクンナン氏, シュオジン・ハン博士(現:ARM ホールディングス), Liam Boodhoo 博士(現:サウサンプトン大学, 博士研究員), ジェイミ・レイノルズ氏(サウサンプトン大学), 宮崎良平氏(水田研究室特別研究学生兼慶応義塾大学, 栗野研究室), 国崎愛子氏(水田研究室特別研究学生兼東京工業大学, 波多野・小寺研究室), 前倉遼氏(沖縄高等専門学校), ディネシュ・ゴダラ氏(インド工科大学カーンプル校), アイシャ・カリド氏(マレーシア国民大学), アーロン・テオ氏(サウサンプトン大学マレーシア校), ラシュミ・シェンド氏(インド工科大学マドラス校), Zulkefli Mohd Amir 氏(マレーシア国民大学), 皆様のご助力に深く感謝申し上げます.

イギリス, サウサンプトン大学留学の際にお世話になった多くの方々に感謝の意を表します. 現地でお会いした東京農工大学, 工学部電気電子工学科, 須田研究室の塚本貴広助教には, ラマン分光に関して, 基礎知識から実践的な研究手法までご教授いただきましたことに深く感謝申し上げます. Faculty of Physical Sciences and Engineering, Nanoelectronics and Nanotechnology Group の Sheng Ye 博士と Taharh Zelai 氏には, ケルビンプローブフォース顕微鏡, TERS, AFM およびラマン分光装置の操作方法をご教授いただきました. シニアレクチャラーの Stuart Boden 博士, Xiaoqing Shi 氏にはヘリウムイオン顕微鏡の操作方法をご指導いただきました. Zhencheng Tan 氏, Christoph Riedel 氏, Benjamin Lowe 氏, Sahar Mirzaei 氏, Fayong Liu 氏, Katarzyna Grabska 氏, Abdulraham Al-Attili 氏, Xingzhao Yan 氏, Chirenjeevi Krishnan 氏, Martin Ebert 氏, Taha Ben Masaud 博士, Sun Kai 博士, Swe Zin Oo 博士, Mehdi Banakar 博士, Zuo Li 氏, Nano group の皆様のご助力が無ければサウサンプトンで研究を続けることができませんでした. Kian Kiang 博士, Peter Ayliffe 氏, その他サウサンプトン大学の技術職員の方々にはクリーンルームで多くの機器の操作について丁寧にご指導いただきました. シェアハウスで生活を共にした Zilong Wang 氏, Wanying Xing 氏, Jingbing Zhao 氏, Yujun Feng 氏, そしてシェアハウスの大家である Stephen Laybourne 氏, Joe Laybourne 氏には, 慣れない土地での私生活を支えてくれたことに大変感謝しております.

JAIST, 学生・留学生支援課留学生係, 留学生課の岫真理子氏, 吉田智子氏には,

留学時の手続き等で大変お世話になりました．研究推進課競争的研究費係の河合智史氏，倉元信江氏，三田悠美子氏には科研費管理や学術振興会特別研究員の手続き等で大変お世話になりました．その他 JAIST およびサウサンプトン大学の事務職員の方々には多岐にわたってお世話になりました．深く感謝申し上げます．

博士前期課程時から共に研究生活を続けてきた伊東嶺氏，宇井利昌氏，城取万陽氏，菅原恒氏，博士前期課程で卒業された青柳航平氏(現:シーメンス)，同期の皆様には様々な局面で相談に乗っていただきました．皆様との切磋琢磨が無ければ JAIST での生活を継続することは不可能でした．深く感謝申し上げます．
最後に，経済的・精神的に大きな支えとなり，絶えずご支援くださった家族に心から感謝します．

本研究は皆様のご支援が無ければ成り立たないものでした．深謝申し上げます．

2017 年 3 月 23 日

北陸先端科学技術大学院大学
マテリアルサイエンス研究科
水田研究室

岩﨑拓哉